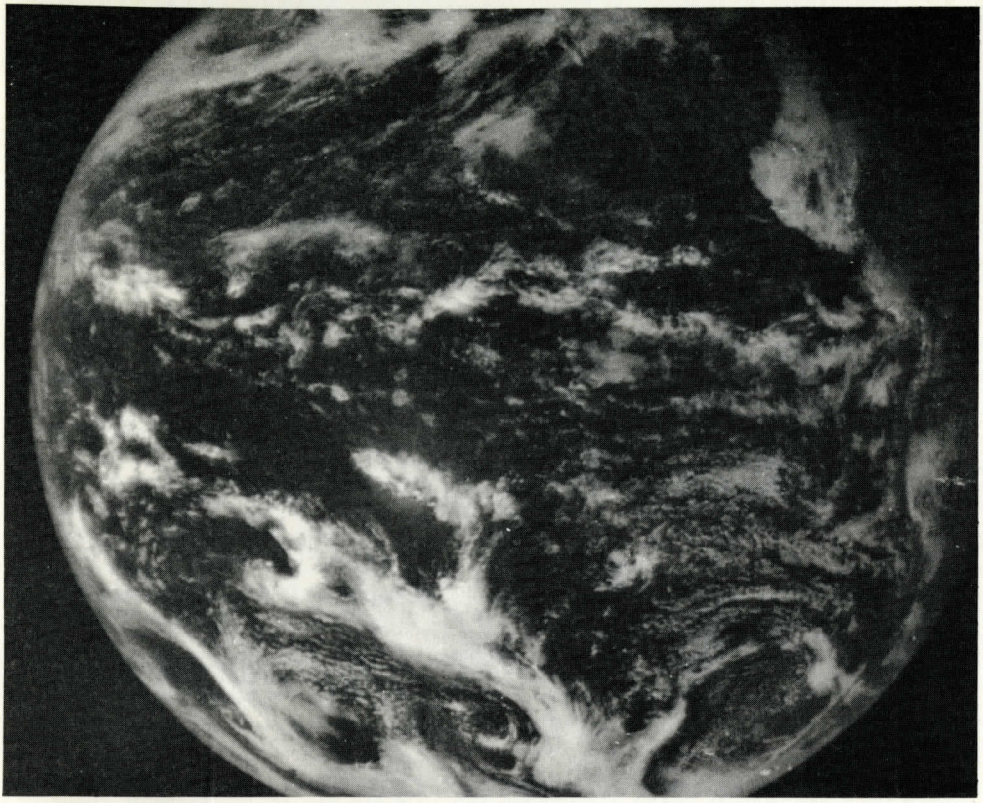

Studies in Atmospheric Energetics Based on Aerospace Probings

Annual Report–1966

Department of Meteorology,
The University of Wisconsin

MARCH, 1967

COVER PHOTOGRAPH

Since early December, 1966, the cloud camera experiment on the ATS-1 satellite has provided spectacular pictures of cloudiness on a scale never previously achieved. Each picture covers nearly 1/3 of the earth's surface. The camera experiment was developed under the direction of Professor Verner Suomi of the University of Wisconsin.

The cover picture was taken on December 11, 1967, and is one of the first pictures obtained after the ATS-1 satellite was injected into orbit. At the time, the satellite was over the equator about midway between South America and Christmas Island, in the central Pacific Ocean. The west coast of South America is visible on the right edge of the photo; however, Christmas Island is not visible.

In the upper-center portion of the picture, Baja, California, is clearly visible northeast of the large cloudless area. This cloudless area is associated with the cold, upwelling water off the Baja, California, coast. Also visible on the picture are clouds associated with large frontal systems over the United States (top right), over the northwestern Pacific Ocean (top left), and over the southern Pacific Ocean (bottom center). Throughout the tropics, considerable east-west organization of cloudiness is visible, showing covergence of the northeasterly and southeasterly trade winds in the tropics.

Many small-scale cloud features, not visible in the cover picture, show up in higher quality reproductions of the picture.

Department of Meteorology
The University of Wisconsin
Madison, Wisconsin

STUDIES IN ATMOSPHERIC ENERGETICS BASED ON AEROSPACE PROBINGS

Annual Report on

WBG-27, Amendment No. 1

1966

The research reported in this document has been supported by the National Environmental Satellite Center of the Environmental Science Services Administration.

250-277

March, 1967

PRINCIPAL INVESTIGATOR

Verner E. Suomi

CONTRIBUTIONS BY

K. Hanson
D. Nelson
R. Parent
V. Suomi
P. Swarztrauber
T. Vonder Haar
J. Weinman

University of Wisconsin

and

The Santa Barbara Research Center

PREFACE

We have used the title of the research grant WBG-27 as the title of this report. While this is useful for accounting purposes, it is not the best description for the report's contents.

Secondly, this report is presumed to serve as a document which describes the research activities carried out on the grant during the past year. It does not do this either. Much of the past year's activities are preparatory to the use of ATS-1 data. It is difficult and possibly pointless to discuss these activities in their partially completed form. This work will be evident in next year's report as the techniques get used on the ATS data.

I wish to thank my associates for their contribution.

V. E. Suomi
Principal Investigator

CONTENTS

ATS SPIN-SCAN CLOUD CAMERA AND PRELAUNCH CALIBRATION PROCEDURE

by

Santa Barbara Research Center
and
University of Wisconsin

The sections of this report dealing with camera design, the camera calibrator, and calibration of the prototype camera have been extracted from a report prepared by the Santa Barbara Research Center for the University of Wisconsin. Copies of the complete report are available at the University of Wisconsin.

The final section of the report dealing with prelaunch calibration procedure for the flight-model camera was prepared by Professors Verner Suomi and Robert Parent of the University of Wisconsin.

CONTENTS

1. INTRODUCTION

This is the Final Report covering the Applications Technology Satellite (ATS) Spin-Scan Cloud Camera prototype and flight model produced by Santa Barbara Research Center for and in association with the University of Wisconsin under the latter's Subcontract No. 1.

Early in 1965, personnel from the University of Wisconsin, from Hughes Space Systems Division, and from Santa Barbara Research Center investigated equipment design concepts that could provide good quality pictures of the earth's cloud cover from synchronous orbit. A decision was made at SBRC and Hughes to company-fund the construction and testing of a feasibility model based on the most promising concept. Santa Barbara Research Center designed and built this test model in a matter of weeks. Results of following tests were so encouraging that the University of Wisconsin proposed an experiment based on this concept for use on the ATS Program.

The feasibility model camera and spacecraft spin simulator are shown in Figure 1-1. The landscape scene photographed by a conventional camera is shown in Figure 1-2. This landscape was scanned by the feasibility model camera to produce the photographs shown in Figures 1-3 and 1-4. The area masked in Figure 1-2 shows the area covered by Figure 1-3. Careful examination of these pictures shown in Figures 1-3 and 1-4, especially the electronic enlargement, shows several defects because: 1) the roofhouse test area was not mechanically stable and movement of personnel, equipment vibration, etc., caused line spacing variation, and 2) the method of recording was to present the video line-by-line on the face of a 10-inch CRT and photograph this presentation with a polaroid camera. The resulting polaroid print was photographically copied. The result was that the camera pictures suffered considerable loss in resolution and dynamic range (contrast). The camera full-field photograph has approximately 1500 horizontal lines while the electronic enlargement has approximately 1000 lines.

2. DESIGN DISCUSSION

The prototype ATS Spin-Scan Cloud Camera quite closely resembles the feasibility model in concept; the major design effort during the prototype phase was directed toward spacecraft interface compatibility, special command-telemetry features, long operating life capability, and stability.

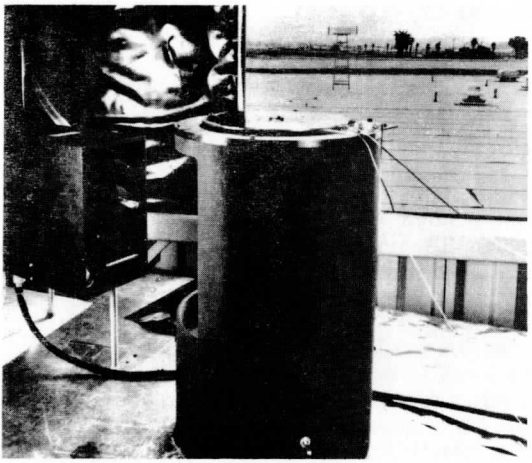

Fig. 1-1. Feasibility Model Cloud Camera (on left) and Spacecraft Spin Simulator

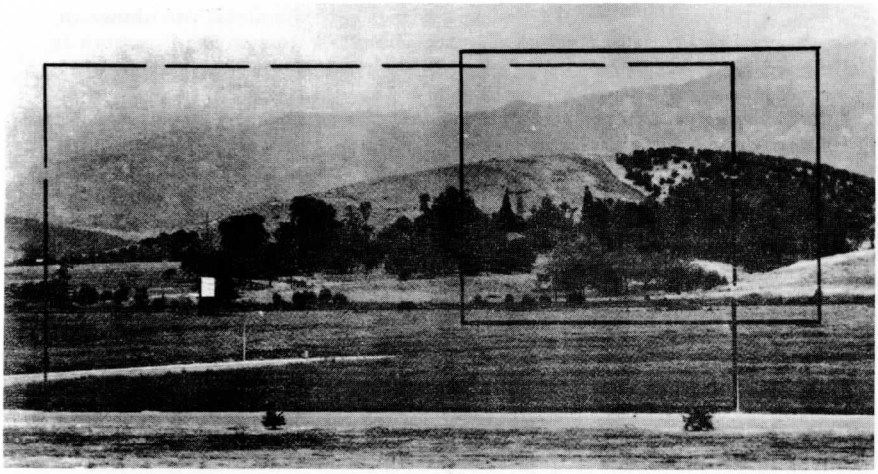

Fig. 1-2. Landscape Picture Taken with Conventional Camera Showing Areas Included in the Camera Full Frame and Small Area Enlargement.

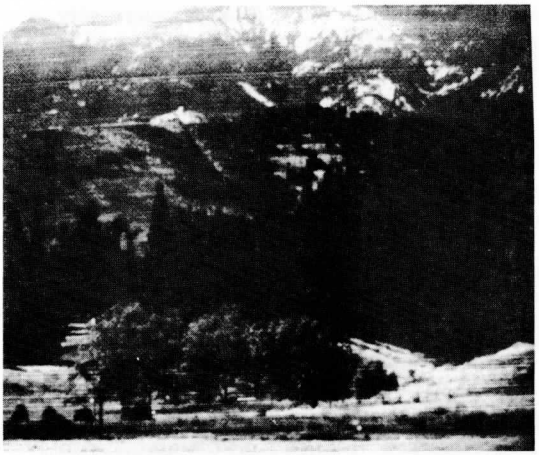

Fig. 1-3. Electronic Enlargement of Landscape made with the Feasibility Model Cloud Camera

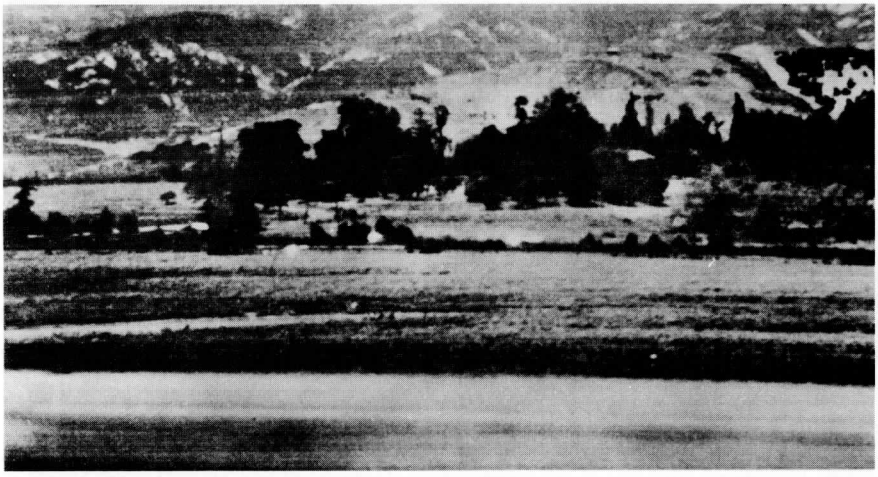

Fig. 1-4. Full Frame Landscape Photograph Made with Feasibility Cloud Camera

Camera final specifications are listed in Table 2-1. Camera sensitivity is intentionally omitted because it requires more than a brief statement and is covered in detail in Section 4 of this report.

GENERAL DESCRIPTION

The Spin-Scan Cloud Camera consists of a high resolution telescope and a photomultiplier light detector coupled with a precision latitude step mechanism. This latitude step motion combined with the spinning motion of the ATS synchronous vehicle provides complete coverage of the earth from 52.5° north latitude to 52.5° south latitude and from the west limb to the east limb. This area is scanned by 2000 horizontal (west to east) lines. The optical resolution is 2.0 nautical miles when the telescope is pointed at nadir from a synchronous equatorial orbit, 22,752 nautical miles from the earth center.

The latitude step mechanism is caused to advance one step by a command from the spacecraft pace system for each spacecraft revolution. This step will occur approximately 158° after the camera has scanned past the north-south earth centerline. When the step mechanism has completed the required 2000 steps, requiring approximately 20 minutes, a limit switch initiates retrace. The substitution of a self-contained 17-Hz oscillator output for the pace command combined with a reversal in step motor phase sequencing causes the telescope to return to the north latitude limit position in approximately 2 minutes. At this point another limit switch signals the return to normal north-south stepping in synchronism with spacecraft rotation.

Four ground commands are available which allow for modification of the step motion. The first two provide for early termination of the latitude stepping and retrace allowing for more rapid coverage of certain earth areas. The commands are called south limit override and north limit override, respectively. The other two ground commands are called normal scan command and back-to-back scan command. The normal scan mode command causes the camera step mechanism to follow the sequence previously described: 20-minute normal down scan and 2-minute retrace. The back-to-back scan command causes the camera step mechanism to step the telescope both down (north to south) and back up (south to north) at the same slow step rate. This alternate mode is accomplished by substituting the pace step command for the retrace oscillator.

The camera step mechanism is pressurized to two atmospheres. A pressure switch is included in this mechanism to indicate a drop in pressure of more than 10 psi. The pressure verification is telemetered down to earth. Additionally, camera power input voltage, two telescope temperatures, scan mode, and scan direction are also telemetered to earth.

The video amplifiers used to drive the video ground link VCO's have provision for insertion of a sun pulse. This pulse is positive going and the camera

Table 2-1. ATS Spin-Scan Cloud Camera Specifications

Optical System	
Type	Two-element reflective
Primary mirror	5-inch diameter paraboloid, 10-inch focal length
Secondary mirror	2-inch diameter, flat
Instantaneous field of view	0.1 ± 0.02 mrad diameter (1/2 power points)
Field stop diameter	0.001 ± 0.0001 inch
Mirror substrate material	Fused quartz
Spectral bandpass	4750Å to 6300Å (defined by optical filter and photocathode)
Photomultiplier	
Type	EMR Model 541A-01-14
Photocathode	S-11 type surface, 1-inch diameter
Scan System	
Line scan	Spacecraft rotation, 100 rpm
Latitude or step scan (15° total)	Camera step provided by sealed mechanical drive (one step per line)
Lines per frame	2000 ± 50 lines
Frame time	20 minutes (100 rpm SC spin rate)
Vertical retrace time	2 minutes
Dwell period (time for instantaneous field to scan a point source)	9.6 μsec (100 rpm SC spin rate)
Electronics	
Voltage gain (video amplifier)	1-10 (fixed resistor adjustable)
Gain stability 0°C to 50°C	± 5%
Dynamic range	≥ 1000/1 (video amplifier)
Linearity	± 2% over dynamic range specified
Electronic upper frequency cutoff	100 kHz (-1 db)
Electronic lower frequency cutoff	0.1 Hz (-3 db)
Signal output	1 volt p-p (nominal), 75 ohms. Two outputs provided. Channel No. 2 provides a camera signal 10 db higher voltage swing than Channel No. 1
Sun pulse input	An input is provided for connection to a spacecraft sun sensor. A 200-400 mv positive sun pulse at this input is added to the camera video and appears in both camera outputs in the opposite polarity as the video.
Size	10 × 11 × 7 inches
Weight	≤ 20 lb
Power (maximum)	-24 vdc, < 1 amp
Operating Temperature	+ 40° to 100°F (environment)

video negative going. The video output is 75 ohms and appears at two coaxial connectors on the camera housing.

The two outputs are identical except that one has a 10-db higher output level than the other. These outputs are dc and are short circuit protected. The video bandwidth at these outputs is 0.1 Hz (-3 db) to 100 kHz (-1 db).

OPTICAL DESIGN

The camera optical telescope is a two-element reflective system composed of a 5-inch diameter fused quartz parabolic primary and a flat 1.8-inch diameter secondary. The equivalent focal length is 10 inches. The optical surfaces are evaporated aluminum overcoated with magnesium fluoride. The effective area of the entrance aperture is 104 cm^2. A field defining aperture is located at the focal plane and provides a circular instantaneous field of view of 0.1-mrad diameter. This field aperture consists of a 0.001-inch diameter hole in a titanium-gold evaporated film on a quartz substrate. Quartz was chosen for its excellent resistance to damaging radiation (UV, IR, etc.), titanium for adherence properties, and gold for high reflectivity. Intermittent exposure to focused solar radiation requires these properties.

Energy collected by the optical system and focused on the field aperture passes through this aperture and is caused to spread over the 1-inch diameter photocathode of the photomultiplier tube by a diverging lens. The lens also provides the required blue cutoff filtering because it is made from Corning-type 3-71 filter glass.

This f/2 optical system required the use of an invar structure and fused quartz optical mirror substrates to provide the necessary dimensional stability with temperature. A compensating type of structure could have been used with an associated reduction in weight; however, expected nonuniform thermal gradients and a tight program schedule ruled out this approach.

In operation the entire camera is constantly exposed to a force of approximately 6 times gravity due to spacecraft rotation. This constant load required that the optics be hard mounted if defocus was to be avoided. Mounting surfaces were carefully lapped to prevent optical surface distortion by the retaining forces.

Tests on the completed telescope to simulate the centrifugal force loading were performed. Loads of several times those predicted produced no detectable change in optical performance.

A diagram of the optical configuration employed is shown in Figure 2-1. The completed telescope assembly is shown in Figure 2-2.

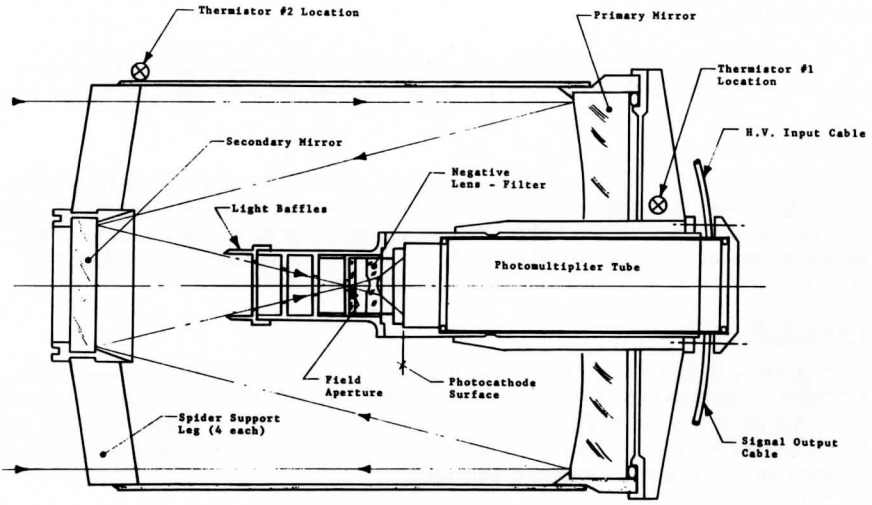

Fig. 2-1. ATS Spin-Scan Cloud Camera Optical Configuration

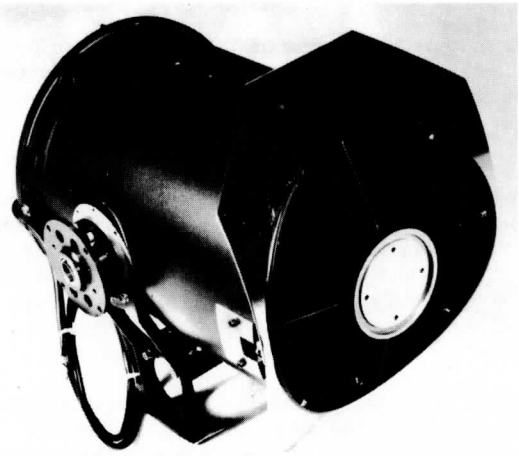

Fig. 2-2. ATS Spin-Scan Cloud Camera Optical Telescope Assembly

MECHANICAL DESIGN

The major mechanical components of the Spin-Scan Cloud Camera are the main housing, the telescope and the precision step mechanism (see Figure 2-3).

Housing

The housing is a lightweight dip-brazed aluminum structure brought to a final T-6 condition. It is composed of two halves to provide ease of assembly. Final machining is done with the halves bolted together for accurate location of the mounting surfaces. The two electronic areas are completely accessible from the outside and have lightweight protective covers.

Telescope

The telescope consists of a tubular structure made from rolled sheet stock, a spider assembly with secondary mirror holder and a photomultiplier tube housing. All parts are made from Invar with the exception of the aluminum light baffled aperture housing. The telescope housing parts are dip brazed prior to final machining of the mirror mounting surfaces.

Two Bendix flexural pivots support the telescope in the main housing and allow for the limited ±7.5° telescope motion. The flexural pivots have the advantage that they are nonlubricated bearings with no radial play. Any radial play in the telescope bearings would introduce error in the step scan linearity and step position repeatability. Step position tests on both the prototype and flight model cameras affirm the choice of the flexural pivots.

Step Mechanism

The camera telescope moves an angular distance of 27 seconds of arc for each rotation of the spacecraft. This precision angular step is accomplished in approximately 10 msec (6° of spacecraft rotation). A schematic of the step drive mechanism which is coupled to the telescope to provide the angular step is shown in Figure 2-4.

The step drive sequence starts with rotary motion from a 90° stepper motor. This motor (IMC Magnetics Model 015-802, Size 15) has four windings which are energized sequentially by the camera electronics. A 90° rotation of the stepper motor shaft produces a 0.0006-inch linear motion along the axis of the lead screw. The linear motion of the lead screw is coupled to the telescope as an angular motion by a rectangular box structure, drive bands and drive sector arms (see Figure 2-4).

Several advantages are apparent in the drive concept: 1) the stepper motor provides high starting torque without additional gear reduction, 2) any step position is repeatable since the motor is always stopped in one of four positions, 3) average power consumption is low because the motor is electrically

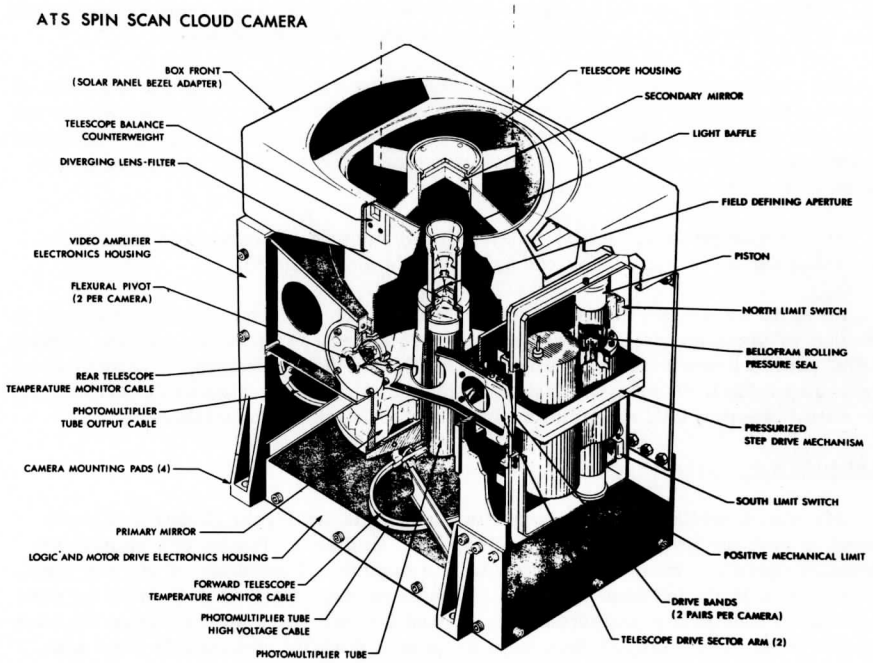

Fig. 2-3. Cutaway Drawing, ATS Spin-Scan Cloud Camera

off between steps, 4) all bearings are run at very low speed, and 5) the system has very little backlash without the use of antibacklash devices.

The drive mechanism has two electrical limit switches to signal the ends of mechanism travel. Two positive mechanical stops are also provided which act as a backup should the switches fail. If these mechanical stops are encountered they provide for a nonbinding mechanism stall, and a manual command can be used to perform the limit switch function.

The telescope is statically balanced and must be positioned in its center position during vibration environments (Tests and Launch).

An extra step mechanism is being life tested in vacuum. This mechanism is loaded to simulate maximum expected performance requirements as described in SBRC internal memo titled "Stepper Motor Torque Requirements," Project 4258 (see addendum). A total of 30 days continuous operation has been demonstrated to date. Testing will continue as long as facilities are available.

Latitude Step Performance

Measurement data of telescope step positions for Flight Model F-1 were used to plot the graphs of Figures 2-5, 2-6, and 2-7. Figure 2-5 shows the angular deviation from step to step from a nominal 27 seconds of arc per step. The dashed lines indicate probable range of reading error as estimated by personnel who made the measurement. Comparing the same step position on each of the three plots (a, b, c) does tend to show a definite measurable step nonlinearity of about 3 seconds of arc maximum, if effects of measurement accuracy are considered.

Data shown in Figure 2-6 were generated from measurements of 100-step increments on F-1. The largest deviation from a nominal 45'06" occurs in (b) at the 500- and 600-step interval. Because the 500-step position is nearly one step short (27 seconds of arc) and the 600-step position is slightly greater than one step, it is reasonable to assume the step count to be in error for this measurement. Data shown in Figure 2-6 (c) support this conclusion since these large deviations did not occur. It should be noted that the final performance summary progressed very smoothly and probably is the most reliable step position data.

The information in Figure 2-7 is intended to show step position repeatability. This could be very important for overlay comparison of successive cloud cover photos. Because the angular values are a difference of two theodolite readings, the reading accuracy is most probably ±1.0 second of arc. Plot (a) has a constant error of +27 seconds of arc due to an error in step count. This is verified by the fact that the angular readings at north and south limits are very close and the total step count is over by one step. Also, plots (b) and (c) do not show this constant one step error.

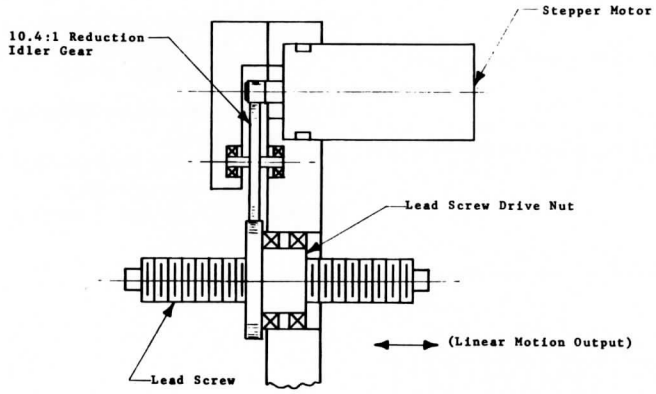

1. 90° Step Motor rotation per step pulse.
2. 10.4:1 deduction to lead screw nut.
3. 0.025 inch linear travel per revolution lead screw nut.

$$90°/\text{pulse} \times \frac{1}{10.4} \times 0.025 \text{ inch}/360° \text{ rotation} = \frac{0.025}{41.6} = 0.0006 \text{ in/pulse linear travel}$$

Fig. 2-4. Schematic of ATS Cloud Camera Precision Step Drive Mechanism

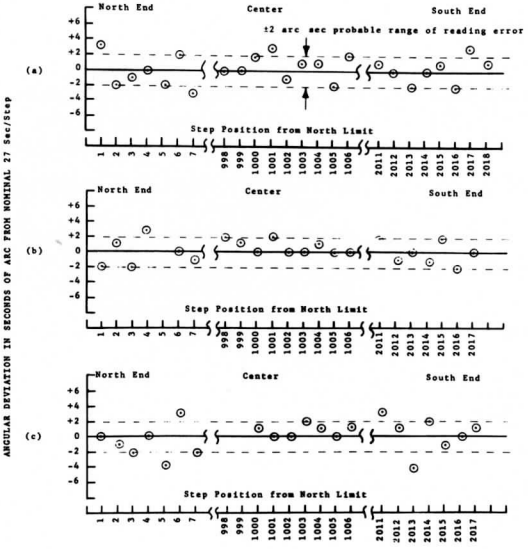

Fig. 2-5. Angular Deviation from Nominal for Single Steps at Both Ends of Center of Frame

(a) Initial Performance Summary Measurement (F-1)
(b) Post-Vibration Performance Summary Measurement (F-1)
(c) Final Performance Summary Measurement (F-1)

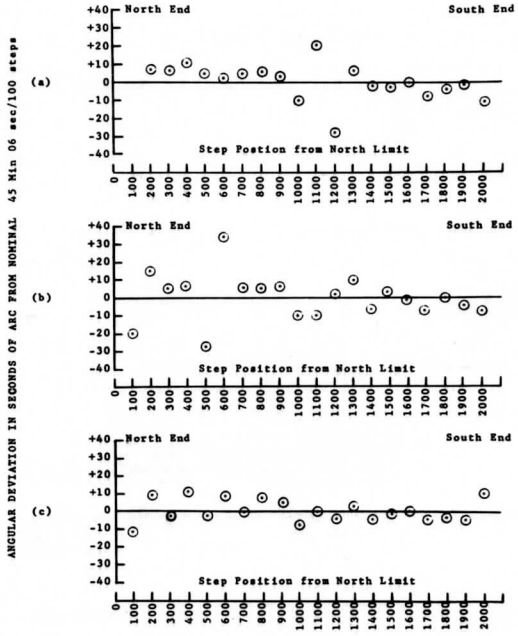

Fig. 2-6. Angular Deviation from Nominal for Each 100 Steps (F-1)

(a) Initial Performance Summary Measurement
(b) Post-Vibration Performance Summary Measurement
(c) Final Performance Summary Measurement

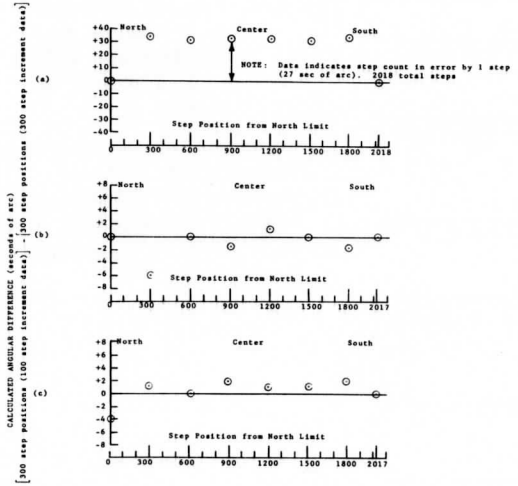

Fig. 2-7. Angular Step Repeatability Error at 300 Step Intervals (F-1)

(a) Initial Performance Summary Measurements
(b) Post-Vibration Performance Summary Measurements
(c) Final (Post Thermal-Vac) Performance Summary Measurements

The largest error in step repeatability is 7 seconds of arc for a 300-step increment. This can be expressed as:

$$\frac{7 \text{ sec max error}}{300 \text{ steps} \times 27 \text{ sec/step}} \times 100\% = 0.086\%$$

The deviation of the measured positions at 100-step intervals from those calculated for an ideal linear step scan is given in Table 2-2. The data used were those taken for F-1 during final (post-thermal vacuum) performance tests. Maximum deviation is +11 seconds of arc and -30 seconds of arc; another way of expressing this might be to say ±1 step deviation maximum at any step position in a 2017-step frame. This excellent linearity will permit accurate distance scaling of resulting photographs.

Table 2-2. Deviation in Seconds of Arc of Twenty 100-Step Incremental Positions from Calculated Positions for a True Linear Step Scan (One Camera Step is 27 Seconds of Arc)

Step Position from North Limit	Deviation (Seconds of Arc)	Step Position from North Limit	Deviation (Seconds of Arc)
100	+11	1200	-18
200	+01	1300	-22
300	+03	1400	-18
400	-08	1500	-17
500	-07	1600	-18
600	-16	1700	-13
700	-16	1800	-09
800	-25	1900	-04
900	-30	2000	+04
1000	-21	2017	+03
1100	-22		

ELECTRONIC DESIGN

The electronic block diagram (Figure 2-8) clearly illustrates the simplicity of the camera electronics. Four major electronic items shown are: 1) video amplifier, 2) photomultiplier tube, 3) photomultiplier high-voltage power supply, and 4) logic.

The video amplifier has an input for the photomultiplier tube video and one for a spacecraft-provided sun pulse. The amplifier input stage provides a fixed resistor gain adjustment of from 1 to 10 which is determined at time of calibration. There are two video outputs with one having a voltage swing 10 db greater

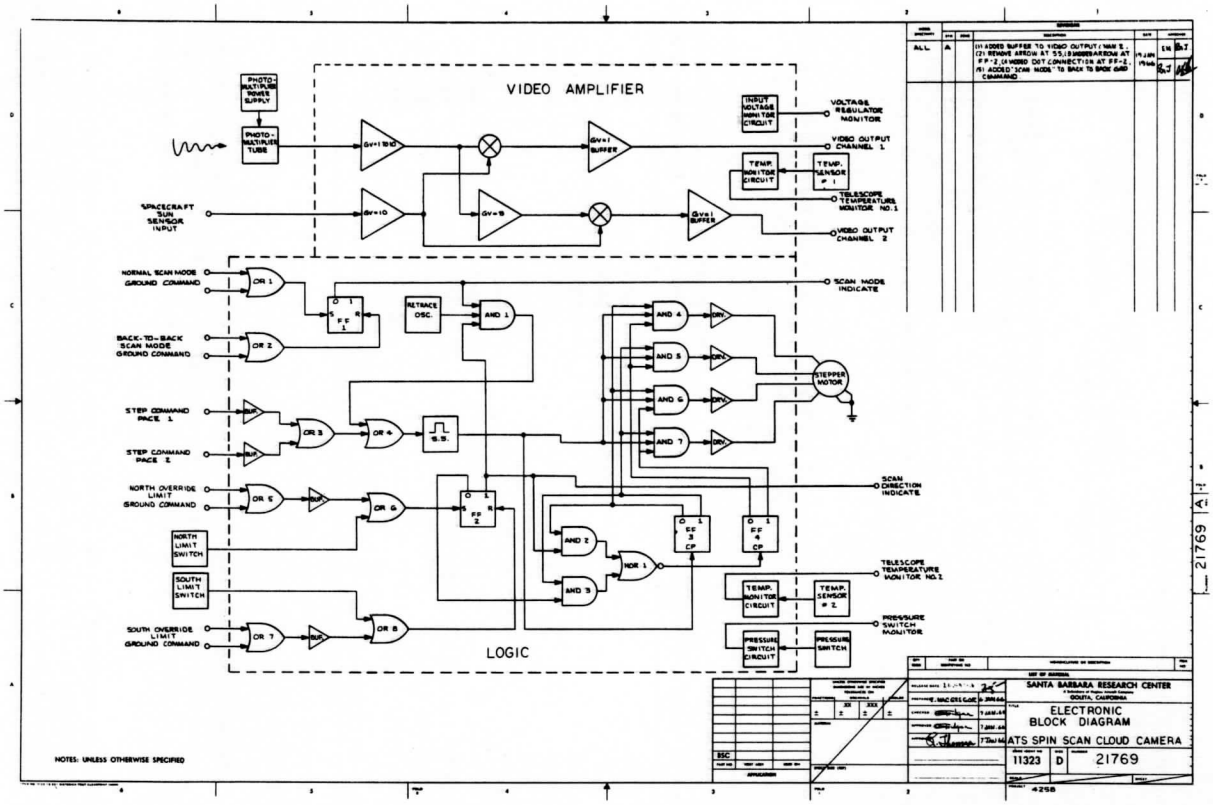

Fig. 2-8. Electronic Block Diagram

than the other. The sun pulse applied to the camera video will appear in both outputs at the same amplitude and opposite in polarity to the video information (video negative going - sun pulse positive going). The camera sun pulse processing circuitry clips approximately 10% of the pulse skirt to eliminate camera video distortion due to the sun sensor seeing the earth. This is necessary since the camera and sun sensor are aligned about the spacecraft spin axis to within a few degrees of each other. A schematic of the video amplifier is shown in Figure 2-9.

The photomultiplier tube is an EMR type 541A-01-14-05600-M-49. This is an end looking, ruggedized, 14-stage type with an S-11 equivalent photocathode. The manufacturer performed a 100-hour burn-in at 5 micro-amps anode current on each tube prior to delivery. A review of the burn-in data indicated a need for further burn-in by SBRC. An additional 150 hours showed good tube stabilization. The only change in tube response since burn-in was observed when the flight model was in the dark in the thermal vacuum chamber for about 4 days. The response increased by approximately 10%. Response reduction for the final 150 hours of burn-in was 25% to 40%. Therefore, some recovery (tube gain) was experienced as predicted by the manufacturer. Since average anode current while scanning in space will be well below 1 microamp, excellent tube stability is expected for the useful life of the camera. Manufacturers' data sheets can be found in the addendum.

The photomultiplier tube high-voltage supply is a Mil Associates Model A-24-0-10-25 High-Voltage Converter. This supply was found to have adequate internal RF shielding but did reflect very narrow spikes at a 14-kHz rate into the 24-volt input power line. A small LC RF filter was inserted just ahead of the supply to prevent this RFI from entering the video circuits or leaving the camera. Additionally, a separate -24 volt input power line was added for additional isolation. A very small ripple (less than 1 mv) was detected in the photomultiplier tube output under no light conditions and was traced to the high-voltage converter output. This was eliminated by the addition of a series 1-megohm resistor in the high-output line. The combination of the high-voltage cable capacitance and the series resistor produced the necessary attenuation with no significant change in tube operation.

The average tube load on the supply is determined by the dynode bleeder string resistance. This is approximately 25 microamps and depends on the value of high voltage selected. Momentary direct looks at the sun by the camera will nearly double this value. The tubes have 90 megohms of bleeder string resistance and the supply is fixed resistor adjustable from 1935 to 2500 volts. The high-voltage value was selected for each camera prior to acceptance testing.

A schematic of the camera logic is shown in Figure 2-10. The logic performs the control functions associated with latitude scanning. These circuits receive camera, spacecraft and ground commands, relay these commands at the proper

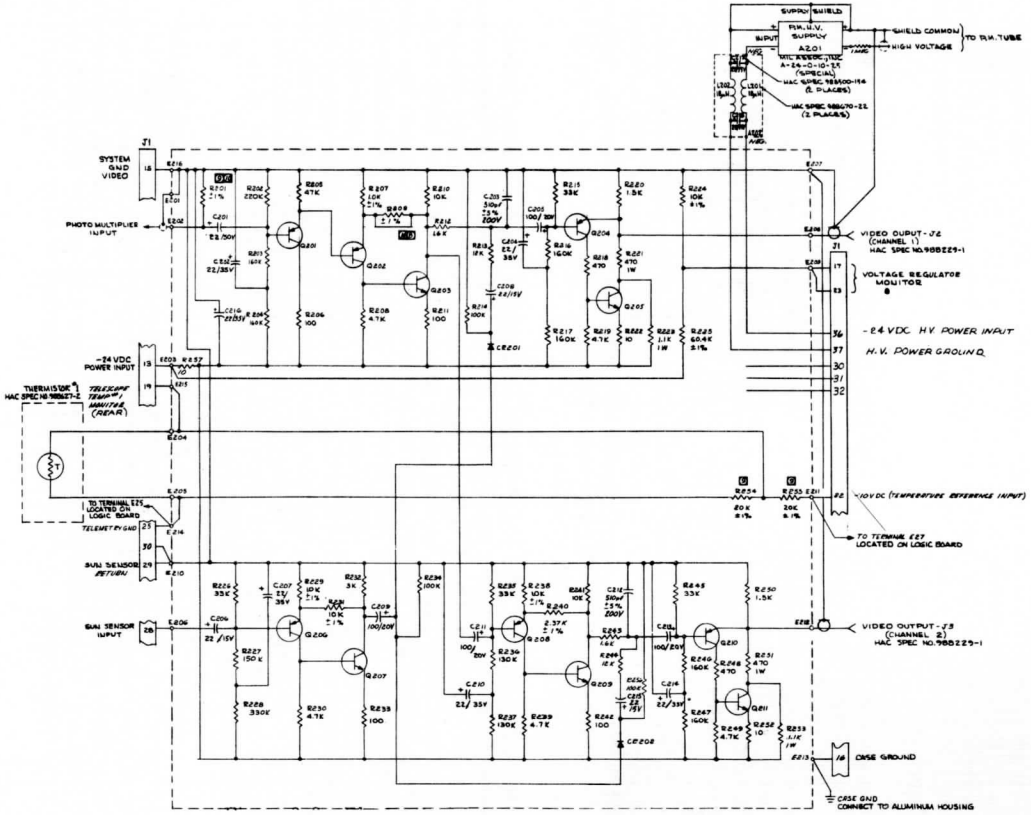

Fig. 2-9. Electronic Schematic Diagram, Video Amplifiers

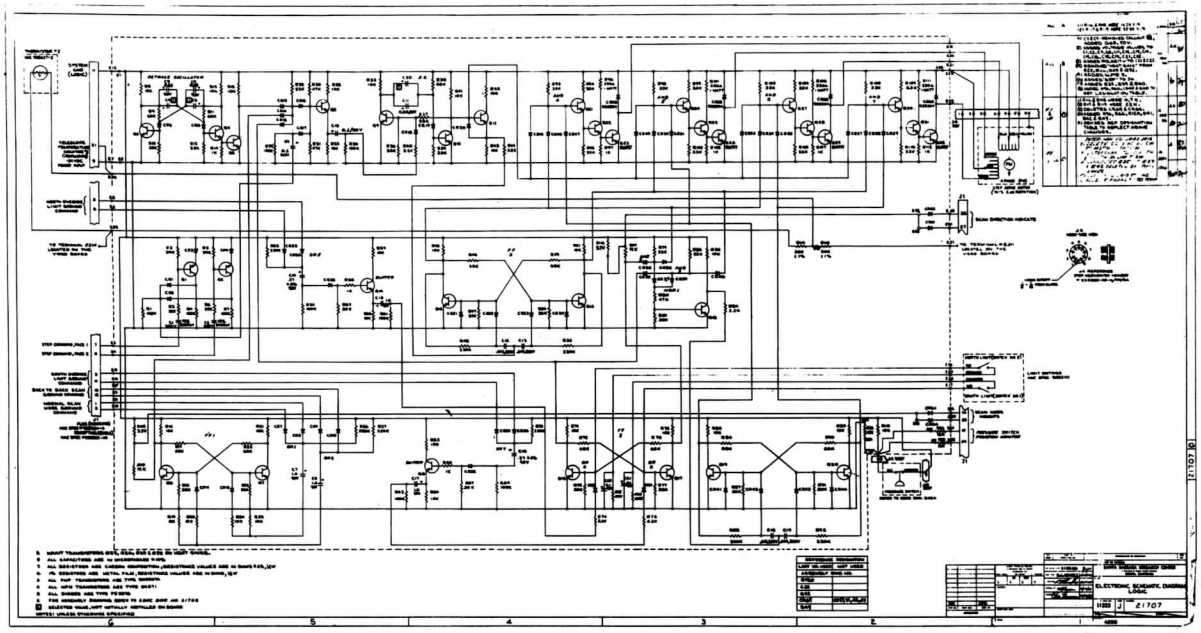

Fig. 2-10. Electronic Schematic Diagram, Logic

time and provide telemetry indications of camera command responses. Due to the simplicity of the logic and drive circuits, a detailed description seems unnecessary. The electronic design in general is based on simplicity and generous safety margins in component ratings. Also, a careful analysis was made of the logic to ensure that no combination of commands or transient situations could cause logic circuit hang-up.

All electronic components used on the two circuit boards are from ATS qualified stock.

The electronic circuit board assembly prior to installation in the camera housing is shown in Figure 2-11. The simplicity of the over-all design approach is illustrated in Figure 2-12 which shows the electronics installed in the camera frame. The photomultiplier power supply can be seen at the lower left in this photo.

COMMAND/TELEMETRY DETAILS

The following description of ground commands and telemetry outputs associated with the cloud camera is included as an aid in ground equipment design and general camera operation.

Camera Commands

1. Normal Scan Command—This command can be initiated at any time but is ideally performed during telescope north-to-south stepping (20-minute period). If this command is given while the camera logic circuits are already in this mode, no change of scan mode will occur. When the camera logic is in the Back-to-Back Scan Mode, initiation of the Normal Scan Command will cause a change of scan mode which will be detectable immediately at the telemetry output labeled Scan Mode Indicate as a "0" state. The camera stepping rate will not be altered until the north-to-south frame has been completed and retrace begins. This retrace will now take place in a 2-minute period (2000 steps) and will not be synchronized with spacecraft rotation as the down scan was, and therefore produce no useful video information.

2. Back-to-Back Scan Command—This command can also be initiated at any time but again is ideally performed during the telescope north-to-south stepping. Again, if this command is given while the camera logic is in this mode, no change of scan mode will occur. When the camera logic is in the Normal Scan Mode (telemetry indicates a "0" state) initiation of the Back-to-Back Scan Command will cause a change of scan mode which will be immediately detectable by a change in telemetry scan mode indicate to a "1" state. When the telescope reaches the south end of the frame, retrace will begin at the down scan rate (2000 steps in 20 minutes) and will be in synchronism with spacecraft rotation. The video information during retrace, while in the Back-

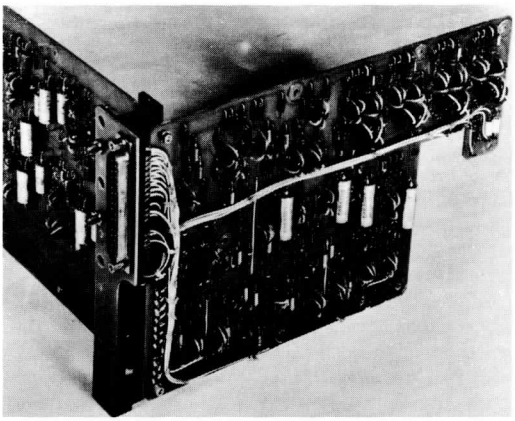

Fig. 2-11. ATS Cloud Camera/ Video-Logic Circuit Assembly

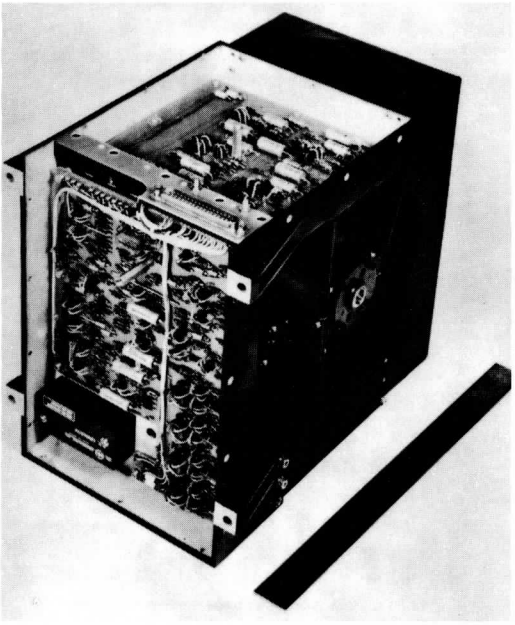

Fig. 2-12. ATS Cloud Camera/ Electronic Area View

to-Back Scan Mode, will be identical to the down scan frame information but will be reversed in time (the south latitude information preceding the north latitude information).

It should be noted that either of the above commands causes the camera logic to lock in either mode and remain indefinitely in that mode until commanded to change or until the camera is turned off.

3. South Override Limit Command—This command is designed to end the north-to-south stepping at any time prior to the end of the frame. If this command is initiated during retrace (south-to-north stepping), the camera logic will not respond. If more than one frame is to be shortened, this command must be sent for each frame. Therefore, some ground timing consisting of step counting will be required to make the best use of this command. The telemetry output called "Scan Direction Indicate" will signal a "zero state" during north-to-south scan stepping and a "one state" during south-to-north scan stepping and a "one state" during south-to-north retrace stepping. The sampling rate of this telemetry channel is such that a maximum error of five lines is possible and this should therefore be considered in devising any ground timing scheme.

4. North Override Limit Command—This override command is identical with the south override limit command except that it is intended to end retrace stepping at some time prior to the telescope reaching the top of the frame. The combination of the two override commands allows for more rapid frames of shorter latitude dimension to study specific earth areas or for a reduction in telescope total angular motion if this motion is suspected as a cause of possible spacecraft nutation.

Telemetry Data

1. Scan Mode Indicate—As mentioned above, this telemetry channel will have the following output indications:

   a. "0" state for the Normal Scan Mode
   b. "1" state for the Back-to-Back Scan Mode

2. Scan Direction Indicate—The following outputs will occur:

   a. "0" state for north-to-south scan stepping
   b. "1" state for south-to-north scan stepping or retrace

Maximum indication error from the 3-second access encoder will be five scan lines for each change of state when the camera is in the Back-to-Back Mode.

3. Telescope Temperature—The temperature of the forward and aft end of the optical telescope is available on two telemetry channels. These two locations were chosen to monitor the differential temperature expected due to the telescope interior exposure to cold space. The telescope is designed to operate with a relatively large thermal gradient between optical elements but actual

thermal data could be very useful for future lightweight designs. Temperature Monitor No. 1 is located on the telescope near the primary mirror and Monitor No. 2 is located at the forward end of the telescope housing near the secondary mirror.

4. Camera Input Voltage—The camera input voltage from the experiment regulator is available in one analog channel of the telemetry. A voltage of -3.41 volts at this output represents 24.0 volts at the spacecraft regulator input to the camera. Any change in this output therefore represents a change in the regulator output by this ratio.

5. Pressure Switch Position Monitor—A pressure switch in the camera step mechanism is used to monitor the internal nitrogen pressure of this housing. This housing is sealed to prevent failure due to loss of lubrication. Initial pressurization is 2 atmospheres absolute. A drop of approximately 10 psi will cause the switch to open. An analog telemetry channel indicates normal pressure when the output is 0 volts and -4.2 volts is an indication of pressure loss. This information should be useful in verifying mechanism life expectancy.

3. CAMERA CALIBRATOR

BACKGROUND

In preliminary discussions of the plans for the spin-scan camera, personnel from Hughes Space Systems Division expressed a need for the capability of a rapid checkout of the camera. This checkout would provide assurance that the sensitivity and resolution of the camera had not degraded during periods of spacecraft handling and test.

The 0.1-mrad field of view of the camera is obtained only with very precise optical alignment and focus. A measurement of deterioration of resolution could not be achieved with an instrument less precise, nor could the time required to set up and align normal optics laboratory types of test equipment be tolerated. Therefore, it was decided to construct a special calibration instrument which would provide the required test features.

It was decided that resolution checks of the optical system could best be performed by Modulation Transfer Function (MTF) measurement techniques. Though classical MTF measurement would be too sophisticated and complex for a field test device, the principle of moving alternate, closely spaced, light and dark bars across the focal plane of a collimator could be applied to the cloud camera.

INSTRUMENT DESCRIPTION

The test instrument shown in Figure 3-1 was designed to provide the required evaluation functions. The telescope has a 5-1/8 inch diameter clear aperture, 75-inch focal length, Maksutov design with diffraction limited optics. The light source, beam splitter, eyepiece and chopper are added to create a versatile test instrument. A schematic of the optical arrangement is shown in Figure 3-2.

Taking advantage of the magnification given by the ratio of length of the camera to the focal length of the calibrator, a chopper of modest size and tolerance is capable of rigorously testing the field defined by the 0.001-inch camera field stop.

The light source is a diffuse bulb of the type commonly used in photoenlargers. The lamp is powered with regulated dc to eliminate any cyclic variation. Typical lamp operating voltages are held at least 25% below rated operating voltage to extend the lamp operating efficiency.

The chopper pattern, shown in detail in Figure 3-3, is photoetched in titanium-gold on a quartz substrate. In an ideal configuration, the bars and spaces would be parallel, whereas this configuration uses the pie-shaped sectors of a rotating disc. This difference can be insignificant if care is used to position the target at a fixed radial position on the chopper for all tests described later in the report, the target was centered at a fixed radial distance indicated by the small triangle point shown in Figure 3-3.

The chopper motor turns slowly enough to allow the highest frequency pulses to be at least ten times longer than the electronic time constant of the system.

A description of the chopper blade in terms of the angular subtense at the camera field of view is shown in Figure 3-4, along with a sketch of the response that might be anticipated if the output signal were displayed on an oscilloscope. A photograph of the oscilloscope trace taken during testing of the camera is shown in Figure 3-5.

It should be added that the calibrator proved very useful during the assembly and test of the spin-scan camera. The ability to use the calibrator device as a simple collimator to observe the camera aperture proved useful. The modulation display is extremely sensitive to poor focus or distortion in the camera optical system. Not only does it detect small distortions which might be overlooked by the eye, but it provides a direct quantitative measure of the image sharpness.

The field of view of the spin-scan camera was specified to be 0.1 mrad at the 50% response, or half power, points. This definition clearly describes the field of view in terms common to hardware that is tested by scanning with a point source of light. The spin-scan camera was not tested in this direct fashion for the following reasons:

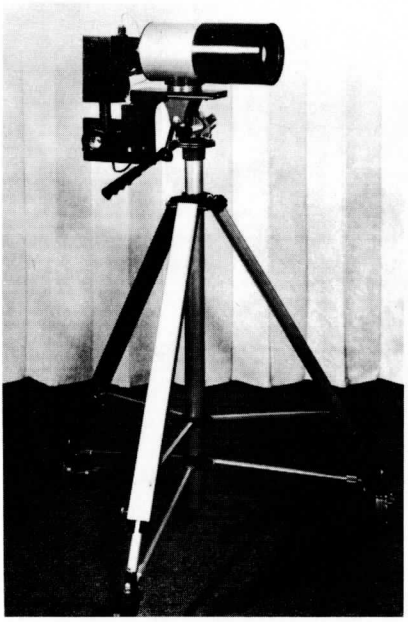

Fig. 3-1. ATS Cloud Camera Calibrator

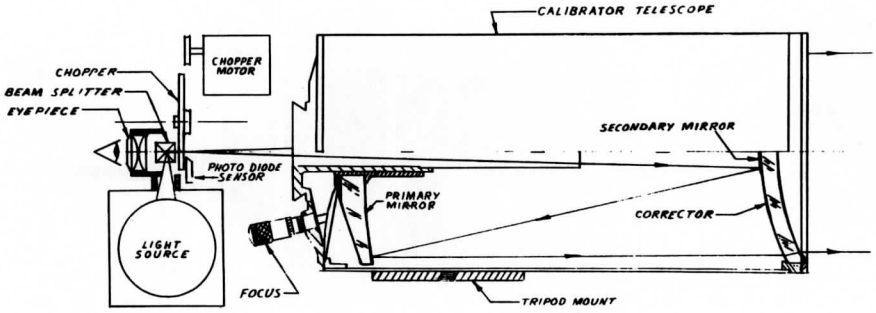

Fig. 3-2. Optical Calibrator Diagram

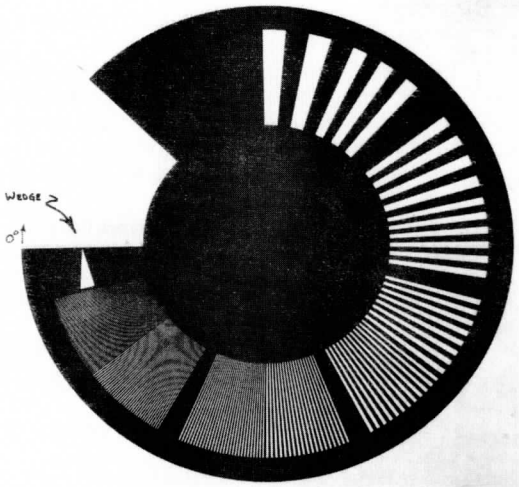

Fig. 3-3. Chopper Pattern/ Cloud Camera Calibrator

Blade Sector	6°	4°	3°	2°	1.5°	1°	.6°	.4°	.3°	.2°
Angular Field (milliradian)	1.05	.697	.523	.348	.262	.173	.105	.070	.052	.035
Time/Cycle (milliseconds)	5	3.33	2.5	1.67	1.25	.833	.500	.333	.250	.167

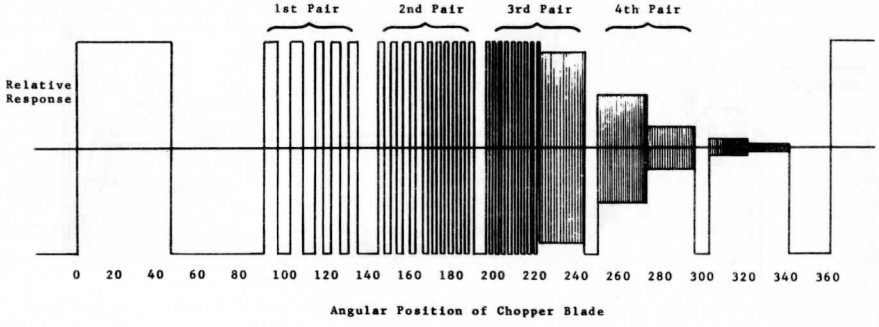

Fig. 3-4. ATS Spin-Scan Cloud Camera Sample Optical Resolution Chart

1. It is very difficult to get sufficient energy in the point source to produce usable signal levels. In this case, the "point" could only be 1 or 2 seconds of arc. Tests would have had to have been accomplished at low signal-to-noise ratios.

2. Laboratory testing of the field of view requires precise alignment control. The process is time-consuming and does not readily lend itself to the frequent testing and troubleshooting associated with instrument assembly.

Therefore, confidence would be low because of the poor S/N ratio, the fact that the point source is not truly a point, and the doubt as to whether a scan had crossed the true field-of-view diameter or perhaps along a chord.

To relate the chopper modulation data to the field of view as defined by the half power points is rather awkward. The truly analytical approaches are handicapped by the small amount of data from the display. The following is pursued here primarily as a matter of interest. It is felt that the modulation testing alone is meaningful and useful, and camera field-of-view specifications might better have been defined in these terms.

To calculate the modulation which might be anticipated with a circular field stop moving across a field of light and dark bars, the modulation is defined

$$M = \frac{\text{maximum transmittance} - \text{minimum transmittance}}{\text{maximum transmittance} + \text{minimum transmittance}}$$

As the ratio of the bar width/aperture diameter is changed, the curve such as shown in Figure 3-6 is generated.

Considering a sample of the test data (Figure 3-5) and the geometry of the test instrument, Table 3-1 is intended to be self-explanatory.

These data are used to construct the plot shown in Figure 3-7. This should represent the field shape if testing had been accomplished with the use of a point source scan. An idealized optical field of view is shown for comparison.

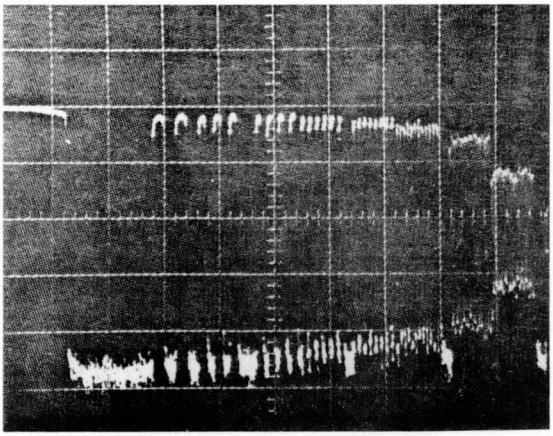

Fig. 3-5. Sample Oscilloscope Photograph of Camera Output for the Calibrator Chopper Light Input

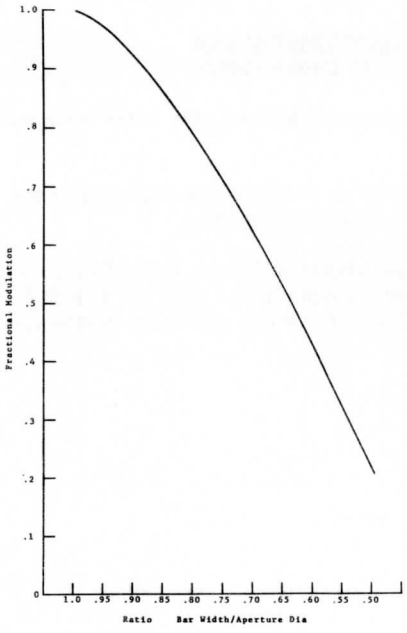

Fig. 3-6. Calculated Fractional Modulation with Ratio of Bar Width/Aperature Diameter

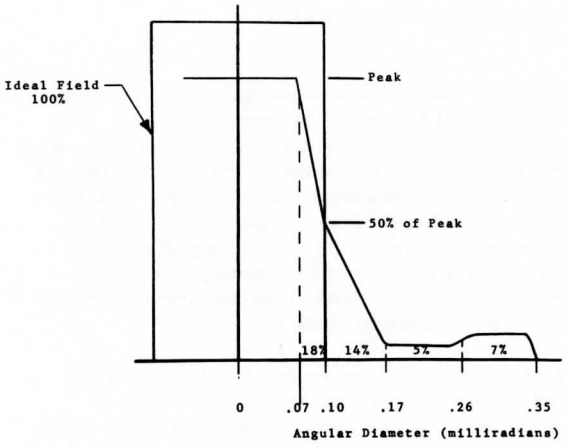

Fig. 3-7. Probable Shape of a Field of View Reconstructed from Calibrator Modulation Data (Table 3-1)

Table 3-1. Data Used to Relate Cloud Camera Modulation to Its Instantaneous Field of View

1. Angular field of bar (mrad) (from the geometry of the calibrator)	0.35	0.26	0.17	0.10	0.07
2. Modulation observed during testing (normalized)	1.0	0.95	0.90	0.70	0.35
3. Ratio of bar width/aperture diameter (from Figure 3-6)	1.0	0.925	0.88	0.742	0.562
4. Apparent blur diameter (mrad) (angular field of bar/ratio)(Item 1, Item 3)	0.35	0.28	0.19	0.135	0.127

However, the apparent blur diameter does not represent the blur which would be observed if the field were scanned with a point source. It is necessary to determine the fraction of energy at each radial distance.

5. The fraction of energy in the blur (4) which is larger than the bar (Item 1)	0.0	0.07	0.12	0.26	0.44
6. The fraction of energy in the increment between bars (from 5)	0.0	0.07	0.05	0.14	0.18

4. CAMERA CALIBRATION DISCUSSION

As mentioned previously, the camera calibrator is used only to check camera performance and not to establish actual calibration. Camera calibration, that is, camera response to a known light input, has been accomplished in two ways. The first method is to image a small area of a strip filament lamp on the camera field aperture. The lamp spectral characteristics and absolute output power are known (Bureau of Standards calibration) and the camera response is measured. If the input light level is within the linear range of the photomultiplier tube, a calibration point on the linear characteristic tube curve is established. The high light level or nonlinear region is known from both manufacturer's data (see addendum) and measurements made during extended tube burn-in.

The second method is to cause light to enter the camera entrance aperture from a known reflective surface exposed to direct sunlight. If the sun and camera are nearly normal to the reflective surface, and measurements are taken for various sun zenith angles, camera performance for bright clouds as viewed from space can be accurately predicted.

PROTOTYPE SPIN-SCAN CAMERA CALIBRATION

All photomultiplier tubes were operated at various multiplier gains and output voltages were recorded as a function of multiples of light input prior to and after SBRC burn-in. This data established tube output voltage as a function of relative light input. Because the lamp temperature was constant and the light was merely attenuated and no attempt was made to define the light input, the spectral characteristics of both lamp and photocathode need not be known. The idea was to define the shape of the tube response curve (linear region, saturation knee, etc.)

Using the photomultiplier tube data supplied by the manufacturer (assuming additional burn-in only reduces the tube gain) and the camera optical parameters, the relative light values can be converted to effective watts. These effective watts are simply watts of light entering the camera aperture in the wavelength region of camera sensitivity. Performance of the camera to any known light input can be predicted from this plot and performance of the actual camera compared with this prediction.

Figure 4-1 shows such a plot for the prototype with the measured point shown in close agreement with the curve.

Because of the delivery schedule, no time was available for outside sun reflection measurements.

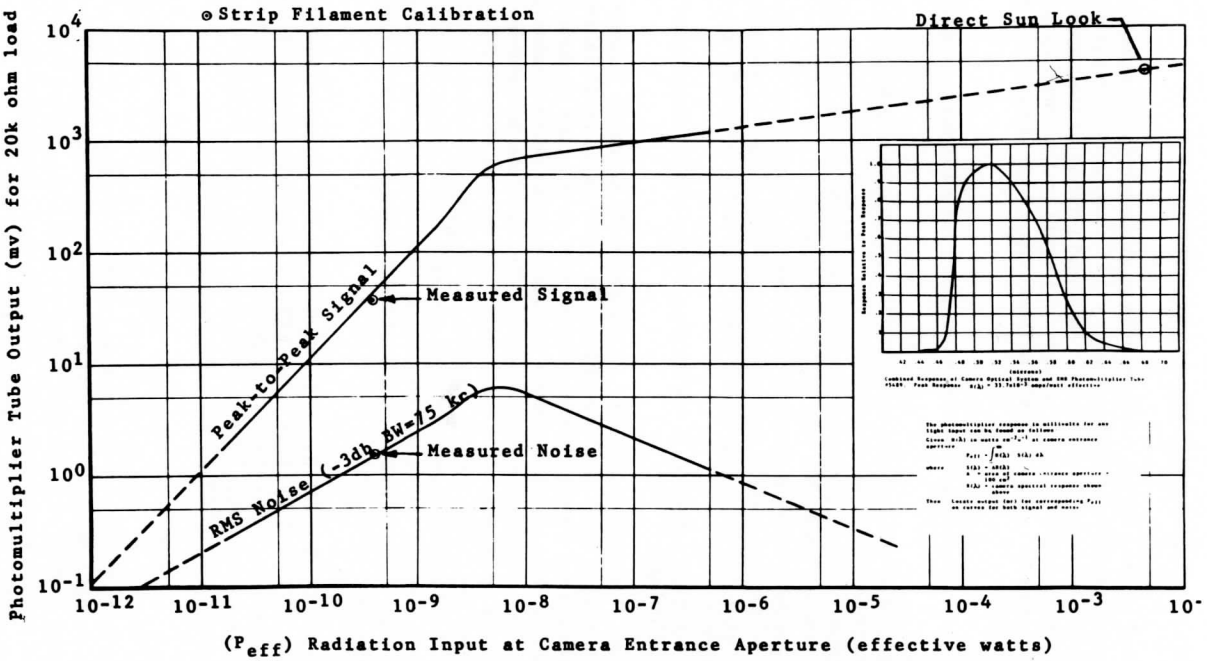

Fig. 4-1. Prototype (P-1) Spin-Scan Cloud Camera Photomultiplier Tube Output as a Function of Effective Radiant Input Power at the Entrance Aperture (HV = 2500 volts)

FLIGHT-MODEL SPIN-SCAN CAMERA CALIBRATION

The primary purpose of the calibration is to establish the relationship between the energy intercepted by the camera as it views a suitable target illuminated by sunlight and the camera output signal. A second purpose of the experiment is to set the level of the camera signal so typical targets on the earth (clouds, etc.) will generate voltages which fall within the design range of the satellite telemetry system.

There are a number of difficulties which make the calibration procedure awkward.

1. We did not have available a calibrated radiation source whose spectral composition is similar to that of sunlight.
2. The exact spectral distribution of the specific quartz-iodide lamps which were used as a variable source was not available.
3. The spectral response of the spot photometer, which was used for relative calibration, did not match the spectral response of the camera; in fact it probably departs from the calibration curve provided with the instrument.
4. The California sunshine is not as pure as the typical Californian would have us believe!

In principle it should be possible to determine the camera's performance in sunlight from first principles alone without the need for an artificial radiation source or without the need for an instrument such as the spot photometer. The light box source and spot photometer were used only as relative measures to aid in setting the sensitivity of the system. The absolute calibration of these devices was not employed. It is awkward to use the sun as a variable source, so the light box was used for this purpose. This box, on loan from the National Environmental Satellite Center, contains 5 quartz iodide lamps whose distance to the diffusing screen can be varied. Thus, the light intensity can be varied over wide limits without changing its spectral content. The limits can be varied by turning off some of the bulbs, as well.

Because the spectral energy distribution of the light from the quartz-iodide lamps is less intense in the blue portion of the spectrum compared to sunlight, and because the pass band of the camera and spot photometer are not matched, it is necessary to use about 20 percent higher readings on the spot photometer to get the equivalent sunlight performance in the camera.

The camera has a filter which allows light in the band from about 4500 to 6500 Å to be measured. As can be seen in Figure 4-2, the solar spectrum is fairly flat in this portion of the spectrum, whereas the energy of the quartz-iodide lamp changes rapidly with wavelength. Thus, even though the spot photometer and camera have slightly different pass bands, their sensitivities will be quite similar in sunlight. On the other hand, the camera will tend to read lower using the radiation from the quartz-iodide lamps.

Photomultiplier Sensitivity Tests

The light box was used in laboratory tests to determine the "knee" of the photomultiplier response curve; the test setup is illustrated in Figure 4-3. In these tests the voltage on the photomultiplier tube was varied as well as the illumination. The resulting performance of the photomultiplier tube is shown in Figure 4-4. One obtains a better signal to noise ratio with higher photomultiplier supply voltage; however, the light level at which the photomultiplier saturates decreases with higher photomultiplier voltage. Thus for operational use, one would like to set the photomultiplier supply voltage as high as possible and yet not have it saturate when viewing the brightest clouds. A close approximation to what this brightness level is for the flight-model camera has been obtained from outdoor tests using the sun as a light source.

Photomultiplier Response in Sunlight

The flight model camera was tested outdoors at Santa Barbara, California on April 27, 1966. The test setup is shown in Figures 4-5 and 4-6. The chopper in front of the camera aperature produced an AC signal q almost perfect sinusoidal wave shape so measurement was simplified to reading a true rms AC voltmeter and realigning the platform for changing sun zenith angle. The scattered light level was also measured by obscuring the direct sun and recording the camera output. Measurement of the direct sunlight was obtained as the difference between the total and scattered light. Data from this test is shown in Table 4-1.

From a series of measurements using a spot photometer and the spin-scan camera, one may determine the illuminance of Kodak white paper as it would appear at the top of the atmosphere (m = 0) normal to the sun's rays. After smoothing a time vs. illuminance plot to the brightest (cleanest) values, Figure 4-7 shows that one can indeed extrapolate to zero air mass with some confidence.

In order for the camera to view a bright target in the atmosphere having high luminance values similar to those obtained for the Kodak white paper extrapolated to the outside of the atmosphere, it would be necessary to:

1. Have a cloud whose albedo is greater than 90 percent.
2. Have the cloud extend high into the atmosphere so a small amount of attenuating atmosphere lies above it.
3. Have the zenith angle of the sun near zero.
4. Have the nadir angle of the camera near zero also.

Only when local noon is at the subsatellite point will all these conditions prevail. There are other phenomena such as specular reflection which gives rise to sea glint and non-isotropic forward scatter when the sun is low on the horizon. These phenomena will yield abnormally high light values, but they are the exceptional cases.

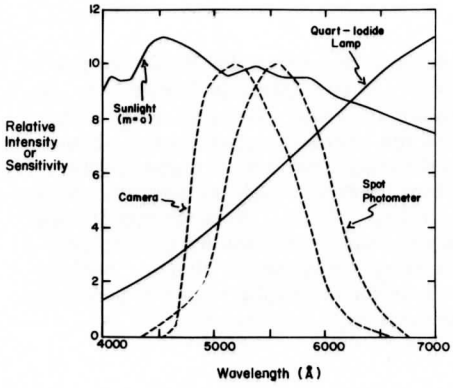

Fig. 4-2. Relative Intensity of Sunlight (at m = 0) and Quartz-Iodide Lamp, and Relative Sensitivity of ATS Spin-Scan Cloud Camera and Spot Photometer.

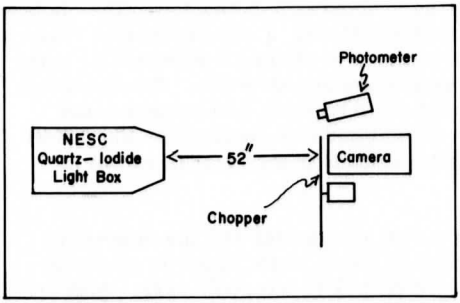

Fig. 4-3. Test Setup for Photomultiplier Response Using the Quartz-Iodide Light Box

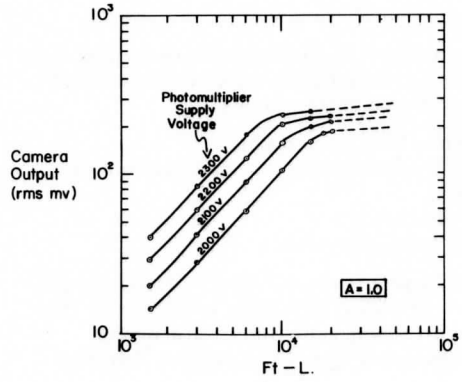

Fig. 4-4. Photomultiplier Response with Quartz-Iodide Light Box

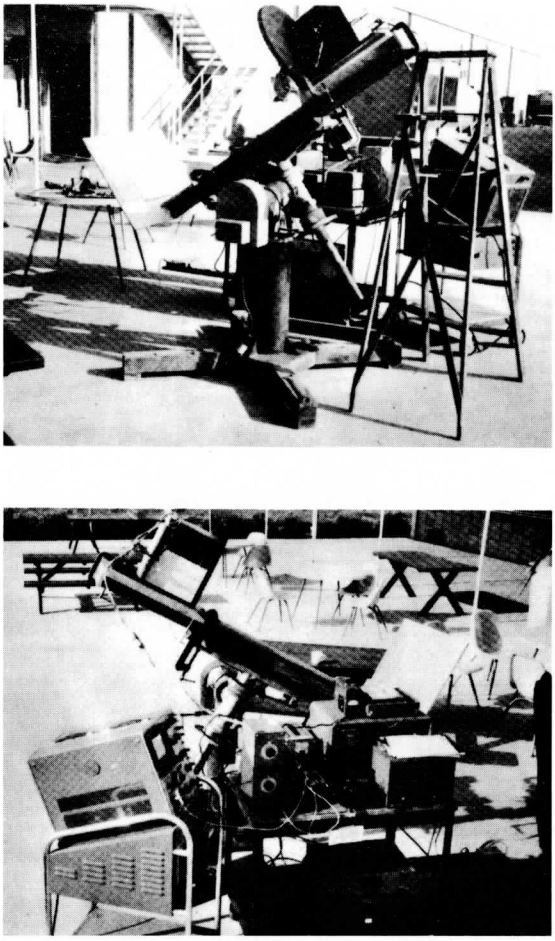

Fig. 4-5. Flight Model Camera Calibration Using Reflected Solar Radiation Source

Table 4-1. Spin-Scan Cloud Camera F-1 Calibration Test Data—Camera and Photometer Output as a Function of Reflected Sunlight from Kodak White Paper at Various Times of Day

Time (Pacific Daylight)	Camera Output (mv rms)		Photometer Output (ft lamberts)	
27 April 1966	Direct and Scattered	Scattered	Direct and Scattered	Scattered
11:52	182	32.8	9800	2050
12:03	178	34	9490	2090
12:05	178	32.5	9330	2000
12:15	175	33.5	9580	2100
12:20	175	32.5	9820	2060
12:33	172	32.0	9660	2140
12:45	170	31.0	9700	2100
13:00	167	32.0	9580	2230
13:15	166	28.5	9700	1990
13:30	165	28.0	9850	2080
13:43	165	26.7	9980	2080
13:55	162		9899	
14:03	162	27.5	9900	2120
14:15	158	27.7	9650	2250
14:39	152.5	29.5	9550	2360
14:52	152.0	28.2	9500	2230
15:00	150	28.4	9460	2220
15:15	146	28.0	9330	2210
15:35	142	27.8	8890	2300
15:45	139	28.4	8890	2280
16:00	136	29.0	8750	2320
16:15	129	28.4	8400	2390
16:27	122	29.4	7900	2350
16:45	114	29.7	7410	2310
17:00	107	28.5	6930	2210

If the video gain is set to include all these phenomena, most meteorological phenomena will have light values near the low end of the detectable video range. We chose, therefore, to set the gain so most cloud systems would give signals near mid-scale. A small percentage of the very brightest targets would therefore saturate the photomultiplier.

Camera Characteristics in Operational Use

For operational use, the upper limit of the linear range of the video has been kept above 10,000 foot Lamberts by setting the photomultiplier supply voltage to 2100 v. Figure 4-4 shows that this supply voltage keeps the "knee" of the video curve sufficiently high.

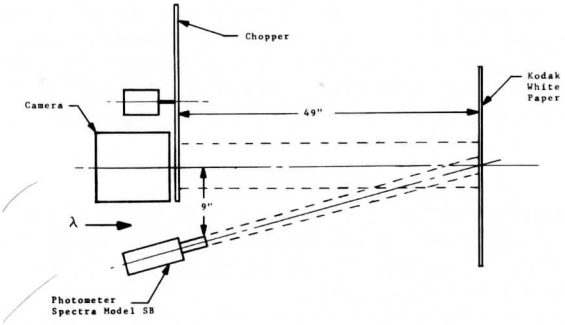

Fig. 4-6. Schematic of Test Setup for Calibration of F-1 Using Reflected Solar Energy

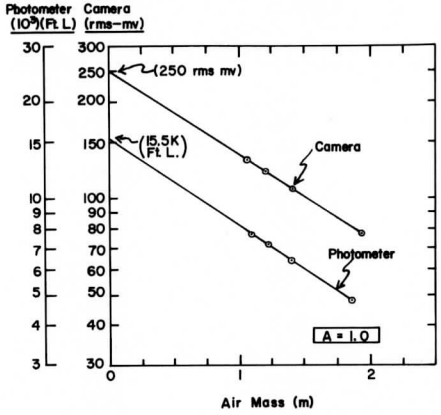

Fig. 4-7. Camera Video Response Using Reflected Solar Radiation Source

The other required prelaunch adjustment of the video level is to set the video amplifier. The adjustable range is between 1 and 10, as shown in the electronic block diagram, Figure 2-8. The amplification, A, is set by specifying the resistance of R209, shown in Figure 2-9. The combined resistance of R209 and R207 in parallel determine the actual A-value of the video amplifier. From the laboratory and outdoor tests, the desired A-value was found to be 2.72. Thus, resistor R209 was specified as 1.72k ohms for operational use of the camera.

Figure 4-8 shows the camera video response with (1) the quartz-iodide light source, (2) a photomultiplier supply voltage of 2100 v., and (3) A-values of 1.0 and 2.72. The data are also given in Table 4-2.

From these measurements and from a knowledge of the spectral distribution of light from the lamps and sun and the spectral response of the camera and

photometer, it is possible to estimate the camera video response to sunlight at the top of the atmosphere. Doing the necessary integration, we find that the camera response to sunlight (at m = 0) is greater than to quartz-iodide light by a factor of 1.21. Thus, we may compute the camera response to sunlight at m = 0 using this factor. The results are shown in Figure 4-8 as well as in Table 4-2.

Table 4-2. Spin-Scan Cloud Camera F-1. Measured Camera (Channel 1) and Photometer Output with Quartz-Iodide Light and Photomultiplier Supply Voltage of 2100 V. Computed Camera Output (Channel 1) for Sunlight at the Top of the Atmosphere.

Photometer	Quartz—Iodide Light			Sunlight
	Measured		Computed (from A = 2.5)	Computed (from A = 2.72)
(ft. L.)	A = 1.0 (rms-mv)	A = 2.5 (rms-mv)	A = 2.72 (rms-mv)	A = 2.72 (rms-mv)
1000	12.8	31	32.7	39.5
1520	19.8	48	52.2	63.0
2000	27.5	63	68.7	83.
3000	42.0	100	109	132
4500	68.0	154	168	203
6000	96.0	215	235	284
8000	132	300	326	395
10000	165	390	425	515
12000	188	450	490	592
15000	210	500	545	660
17500	218	530	578	698
20000	225	540	588	710
25000	228	550	599	723

The outdoor measurements serve as an excellent, independent check on the camera response curve in Figure 4-8, which was obtained with artificial light and was extended to sunlight by calculation. The advantage of using the outdoor measurements for a check on the artificial-light method is that there is less difference between the spectral distribution of sunlight at the top and bottom of the atmosphere than there is between quartz-iodide light and sunlight at the top of the atmosphere.

Using the camera and photometer response to sunlight on Kodak white paper at the top of the atmosphere, as shown in Figure 4-7, and applying an A-value of 2.72, we see the camera output would be 680 rms mv. for a target of 15,500 ft. L. This single value is plotted as a point in Figure 4-8 and falls on the response curve for an A-value of 2.72. This verifies results with the artificial-light method.

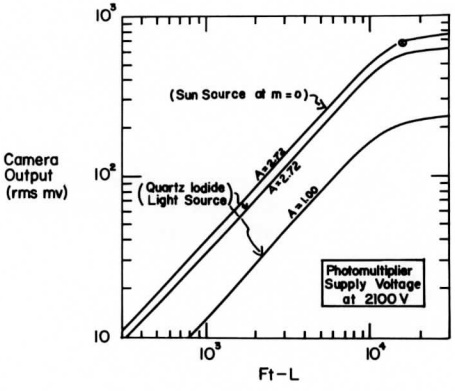

Fig. 4-8. Camera Video Response

Using the procedure described above, we have established the magnitude of the camera signal that will be generated by a surface having the same spectral reflectivity characteristics as Kodak white paper near normal to the solar beam above the atmosphere. (The spectral reflectivity characteristics of Kodak white paper are shown in Figure 4-9.) If the sensitivity of the photomultiplier tube were stable with time in a space environment, it should be possible to obtain the albedo of clouds for the camera spectral pass band. Unfortunately, despite a substantial effort to "burn in" the photomultiplier photocathode to make it more stable, the photomultiplier becomes temporarily about 10-15 percent more sensitive when it has a short history in total darkness or low light levels. This increase in sensitivity is evident in the early readings of the calibration experiment. Thus, we cannot use this calibration as a precision calibration for the instrument sensitivity in space.

Use of the Moon as a Camera Stability Check

The camera will scan about 70 lines across the face of the moon. Thus it will be possible to use portions of the moon's surface or the mean value of the whole moon as a lunar monthly check of the camera sensitivity stability. Of course all the appropriate astronomical parameters will have to be taken into account.

It should be possible to get a good estimate of the absolute value of the camera sensitivity using the moon as a light source. One should be able to carry out a series of moon brightness measurements from a high mountain top on a moonlight night using a carefully calibrated spot photometer having an identical spectral pass band as the camera. Since the pass band of the camera does not include any significant absorption bands in the CO_2 or H_2O spectrum and Mie scattering is small, an extrapolation to the top of the atmosphere making use of Beers law attenuation should give excellent results. Since the spin-

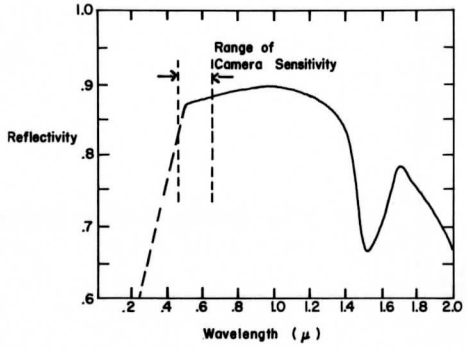

Fig. 4-9. Spectral Reflectivity Characteristics of Kodak White Paper

scan camera views the moon without an intervening atmosphere, it should be possible to calibrate the camera at least as often as monthly intervals.

The first calibration of this type is planned for the summer of 1967 on a mountain station in the Hawaiian Islands. The work should be continued as needed to determine a history of the sensitivity of the photomultiplier tube on ATS-1. When this history is documented, one can proceed with determining the albedo of clouds within the spectral pass band of the camera and may then begin working on the host of meteorological problems in which precision albedo determinations are useful.

THE REFLECTION OF SUNLIGHT TO SPACE AND ABSORPTION BY THE EARTH AND ATMOSPHERE OVER THE UNITED STATES DURING SPRING, 1962

by

Kirby J. Hanson, Thomas H. Vonder Haar,
and
Verner E. Suomi

ABSTRACT

This study describes a method for determining the reflection of sunlight to space and absorption by the earth and atmosphere, using low-resolution radiometer data from earth satellites. The method has been used with TIROS IV data together with radiation measurements at the ground to determine the reflection and absorption of sunlight over the United States during the Spring of 1962.

The results indicate that for this region and time, 40 percent of the incident sunlight at the top of the atmosphere was reflected to space, 13 percent was absorbed by the atmosphere and clouds, and the remaining 47 percent was absorbed at the earth's surface. Atmospheric absorption of the sunlight varied from over 20 percent in the moist air in southeastern United States to less than 10 percent over much of the dry mountain west and northern plains.

Atmospheric absorption values determined from this study have been compared with earlier studies of absorption in a cloudless atmosphere. There is good agreement at low values of water vapor; however, the present study gives significantly higher absorption at high values of water vapor.

An empirical relationship is determined for fractional absorption of sunlight as a function of optical pathlength of water vapor, based on the present study.

$$q_a = 0.096 + 0.045(u^*)^{1/2} \text{Log}_e(u^*)$$

The fractional absorption of sunlight, q_a, is the fraction of the total amount incident at the top of the atmosphere. The optical pathlength, u^*, is given in cm.

$$u^* = u \cdot \sec(\zeta)$$

Here, u is total precipitable water in a vertical column, given in cm, and ζ is the solar zenith angle.

CONTENTS

LIST OF SYMBOLS

Symbol	Meaning
Roman Letters	
A_s/A_f	Ratio: albedo snowcovered ground to albedo snow-free ground
c_p	Specific heat of air at constant pressure
d	Direct distance from point p on ground to satellite at height h
g	Acceleration of gravity at earth's surface
h	Height of satellite
I_s	Solar constant
p	Point at earth's surface
q_a	Fraction of Q_0 absorbed in the atmosphere
q_e	Fraction of Q_0 absorbed at the ground
q_g	Fraction of Q_0 incident at the ground
q_r	Fraction of Q_0 reflected to space
Q_a	Radiation absorbed in the atmosphere
Q_g	Irradiance at the ground
Q_0	Irradiance at the top of the atmosphere
Q_r	Outward Irradiance at the top of the atmosphere
Q_s	Irradiance reflected at the ground
r	Earth-sun distance
r_m	Mean earth-sun distance
u	Total precipitable water in the atmosphere
u*	Optical pathlength of atmospheric water vapor
WF_p	Weighting factor for radiance from point p to a spherical sensor at height h above the earth
w	Mixing ratio of water vapor
Greek letters	
α	Surface albedo
ζ	Solar zenith angle at the subsatellite point
ϕ	Zenith angle of satellite at height h, viewed from point p

1. INTRODUCTION

The albedo is defined as the ratio of reflected to incident radiation integrated over the solar spectrum from 0.2 to 4.0 microns. The albedo of the earth and atmosphere is an important component in the global heat budget, but, unfortunately, it is a difficult component to determine. Prior to 1957, there was no possibility of making direct measurements of this component on a global scale. In the ensuing nine years since satellite measurements have become available, there has been conflicting interpretation of them. One problem in determining the albedo of the earth and atmosphere is that cloudiness, which has a strong modulating influence on the albedo, varies widely over the planet both in time and space. This, of course, causes a sampling difficulty because measurements cannot be made everywhere, all the time. Another hindrance to determining the albedo is that the scattering properties of water droplets in clouds, together with the variable solar zenith angle over the spherical earth, further complicates the sampling.

Prior to the launching of earth satellites, the only "outside" approach to determining the amount of sunlight reflected from earth was to measure the "earthlight" reflected from the shadowed side of the moon (Danjon [3]; Dubois [4]). Computations of the planetary albedo have been made from those illumination measurements (Angstron [1]). Another approach to estimating the earth's albedo was through a knowledge of cloud distribution over the earth and estimates of the reflectivity of various cloud types (Simpson [13]; Houghton [6]; London [11]).

Recently, Fritz et al. [5] have described a method of combining satellite and surface radiation measurements to determine the reflection and absorption of sunlight. In that study, the data from medium-resolution radiometers of TIROS III were used. This gives the albedo of relatively small areas (50 km radius) near surface radiation stations. In comparison to Fritz, the study reported in this paper is similar in that it combines simultaneous satellite and surface data to determine reflection and absorption terms. However, it differs in that low-resolution measurements are used. Thus, the resulting albedoes are representative of larger surface areas.

The low-resolution measurements have been described by Suomi [14] and House [8].

2. METHOD OF CALCULATION

From consideration of conservation of radiant energy, it is clear that sunlight reaching the top of the atmosphere is either reflected to space or is absorbed by the earth or atmosphere. To define these relationships for the present study, we have used a notation similar to that of Fritz.

As illustrated in Fig. 1, Q_o and Q_r are the values of solar irradiance incident and reflected from the top of the atmosphere. Likewise, Q_g and Q_s are values of solar irradiance incident and reflected from the earth's surface. These irradiance terms define the absorption in the atmosphere, Q_a, as

$$Q_a = (Q_o + Q_s) - (Q_r + Q_g) \tag{1}$$

Dividing Eq. (1) by Q_o and rearranging terms gives,

$$1 = q_a + q_r + q_g(1 - \alpha) \tag{2}$$

where:

$q_a = Q_a/Q_o$, the fraction of incident sunlight absorbed in the atmosphere.

$q_r = Q_r/Q_o$, the fraction of incident sunlight reflected to space.

$q_g = Q_g/Q_o$, the transmission of the atmosphere.

$\alpha = Q_s/Q_g$, the surface albedo.

The right-hand term in Eq. (2) is the fractional absorption at the earth's surface and will be denoted as simply q_e. Then,

$$1 = q_a + q_r + q_e \tag{3}$$

It is apparent from Eq. (3) that the sunlight incident at the top of the atmosphere is divided between two absorption terms: (1) the absorption in the atmosphere, q_a, and (2) the absorption at the earth's surface, q_e, and one reflection term: the reflection of sunlight to space, q_r, by the earth, atmosphere and clouds.

Clearly, the fractional terms are completely specified if the four irradiance values are known and are compatible in time and space. The following section defines the irradiance terms to assure this compatibility.

a. Irradiance at the Upper Boundary

The irradiance at the upper boundary of the atmosphere, Q_o, was calculated from

$$Q_o = I_s(r_m/r)^2 \cos \zeta \tag{4}$$

The solar constant, I_s, was taken as 2.0 cal/cm^2 min, r_m and r are the mean and actual earth-sun distances, and ζ is the solar zenith angle at the subsatellite point.

b. Outward Irradiance at the Upper Boundary

The outward irradiance at the upper boundary was obtained from TIROS IV low-resolution measurements of sunlight reflected to space by the earth, atmosphere and clouds. Although these TIROS sensors respond to sunlight reflected from a relatively large area below the spacecraft (radius of 2890 km), [1] the radiation reaching the sensor is strongly weighted in favor of a relatively small area around the subsatellite point. For example, about 50 percent of the irradiance comes from an area with radius of 734 km, centered at the subsatellite point.

c. Irradiance at the Ground

The irradiance at the ground, Q_g, was calculated from radiation measurements at many surface stations in the region viewed by the satellite. Data were weighted by a factor that was symmetrical about the subsatellite point and varied in the same manner as described in the preceding section for satellite measurements of outward irradiance. Identical geographical weighting is an important consideration of this study, because it is essential that irradiance determined for the upper and lower boundaries of the atmosphere represent identical areas. This is necessary because atmospheric absorption is only a small difference between large irradiance values. The appropriate weighting factor for radiation from a point p on the ground reaching a spherical sensor at height h above the ground has been derived by House [7], as

$$WF_p = (h/d)^2 \cos \phi \qquad (5)$$

Here, d is the direct distance from p to the satellite, and ϕ is the zenith angle of the satellite, viewed from point p.

d. Irradiance Reflected at the Ground

The irradiance reflected at the ground, Q_s, was obtained as the product of irradiance at the ground and the surface albedo. Albedo values are representative for an area around the station with a radius of 280 km. The particular radius value was selected in order to include all of the area between surface stations. The values used were the "winter-minimum" albedoes (Fig. 2) for the United States as determined by Kung, et al. [10]. Since these are representative of snow-free conditions, it is necessary to correct them if snow exists at a particular time. Using observed daily snow depth, a best estimate of the surface albedo at each station, each day was calculated. The nomogram (Fig. 3) developed by Kung was used for translating snow depth to albedo.

[1] Distance from the subsatellite point to the earth's horizon, as viewed from the satellite.

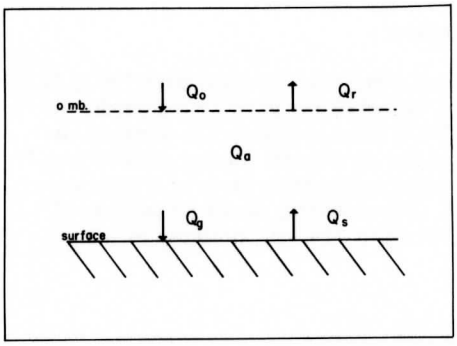

Fig. 1. Symbols for irradiance bounding the atmosphere and absorption of radiation in the atmosphere.

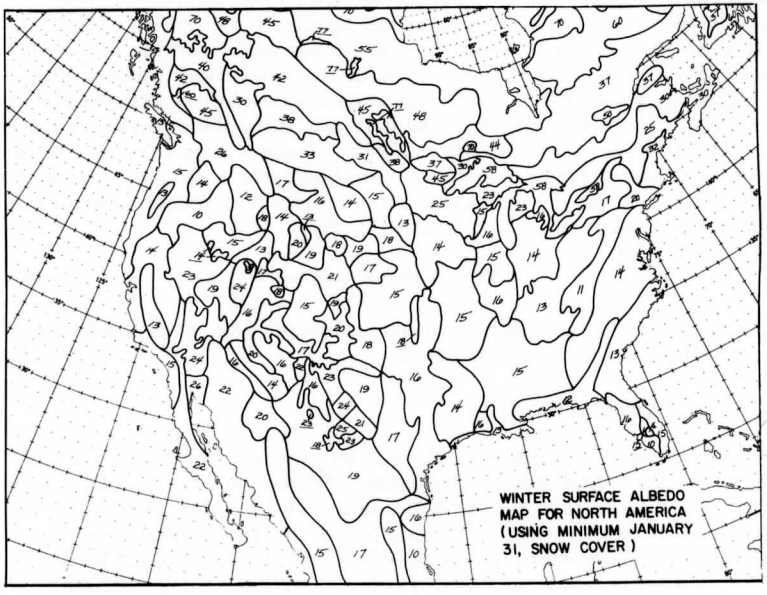

Fig. 2. Winter-minimum albedoes based on minimum snow cover (from Kung, et al. [10]). (Values are percentages)

e. Boundary Condition

A limitation of this study is that outside the surface-station network, it is no longer possible to determine an irradiance at the ground which is representative of the area seen by the satellite. As a result, measurements along the periphery of the network may be in error—particularly where a significant change in cloudiness or surface albedo occurs across the boundary. Inside the boundary, and over most of the continental United States, this is not a problem.

3. MEASUREMENTS

a. Irradiance Values

A total of 775 observations of outward irradiance, Q_r, were obtained by TIROS IV low-resolution radiometers over the United States from February 8 - June 3, 1962. For calculating the partitioning of sunlight, it was required that the other three irradiance terms correspond in time and space with the satellite ogservation. To do this, the irradiance at the ground was calculated from hourly radiation measurements at surface stations, weighted geographically as previously defined. Hourly surface observations were used for convenience, since the satellite data have no systematic time bias within one hour intervals. The two other irradiance terms were calculated as previously described.

Because of the precession of TIROS IV, daytime observations over the United States are not on a continuous basis, but are for intermittent periods. These periods are shown in Fig. 4. In addition to time bias, there is geographical bias in the sample. This is due to: (1) the orbit inclination of 48.3 degrees which has the effect of increasing the relative frequency of observations in the northern latitudes, and (2) the location of read-out in the eastern United States which has the effect of decreasing the number of observations in that region. Clearly, the data used in this study are biased in time and space. To surmount this problem we have equalized the bias in all variables being studied. Only then, it will be possible to obtain meaningful relationships between them.

b. Optical Pathlength of Atmospheric Water Vapor

Atmospheric water vapor is an effective absorber of sunlight and a variable constituent of the atmosphere. As a result, absorption by water vapor is significantly large, but not geographically uniform. In this paper, the absorption of sunlight as a function of precipitable water is examined in order to make an estimate of its nonuniformity.

A calculation of total precipitable water, u, was made to correspond with each satellite observation. The radiosonde observation closest to the sub-

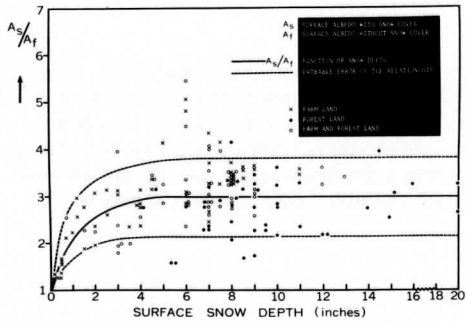

Fig. 3. A factor A_s/A_f for modifying the albedo of snow-free ground as a function of snow depth (from Kung [10]).

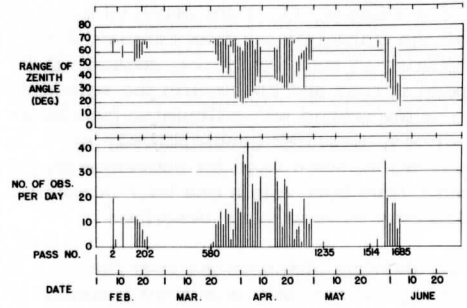

Fig. 4. The number of daytime observations from TIROS IV low resolution radiometers and associated solar zenith angles at times when the satellite was over the continental United States, February-June, 1962.

satellite point, in time and space, was used. The total precipitable water was computed as,

$$u = g^{-1} \int w \, dp \tag{6}$$

where g is the gravitational acceleration at the earth's surface, w is the mixing ratio of water vapor, and p is pressure. The integration was done from the surface to 300 mb.

Over most of the atmosphere, sunlight enters on a slant path rather than vertically. Then, if ζ is the zenith angle of the sun, the optical pathlength, u^*, for sunlight penetrating a clear atmosphere is given as

$$u^* = u \cdot \sec \zeta. \tag{7}$$

4. GEOGRAPHICAL DISTRIBUTION

a. Reflection and Absorption of Sunlight over the United States

The reflection and absorption data were calculated for the hours indicated on Fig. 4. For the period March through May, averages of reflection, absorption and total precipitable water data are shown in Figs. 5 and 6. Spatial smoothing was done by averaging observations within 330 km of fixed grid points over the United States. A 2 by 2 degree latitude-longitude grid was adopted for this purpose. In the southeastern United States where there are sampling limitations, a minimum number of 15 samples was required at a grid-point before the average was calculated. Over the remainder of the United States, the data have been shown up to the border, even though the boundary condition may influence the representativeness of the analysis.

Several relationships between the partitioning terms are significant in Figs. 5 and 6. For example, the patterns of atmospheric absorption and absorption at the ground show similar trends—particularly over the eastern two-thirds of the United States. This suggests that, in comparison to reflection, absorption in the atmosphere has a very dominant effect on the amount of sunlight reaching the ground. It is interesting that neither of these two patterns resemble that of reflection to space. An exception to this is over the Western United States where absorption at the ground appears to be inversely correlated with reflection to space.

A physical interpretation of these results suggests that in areas where the atmospheric water vapor tends to be uniform (e.g., in western U.S.), the variation in atmospheric absorption is correspondingly small. Under these conditions, the reflection term has a dominant effect on the amount of sunlight reaching the ground. On the other hand, in regions where atmospheric water vapor is nonuniform (e.g., in eastern U.S.), the variation in atmospheric absorption is increased, considerably. In fact, it appears to be increased to the extent that water vapor has the dominant effect on the amount of sunlight reaching the ground, rather than the modulating effect of clouds which would otherwise control it.

A striking feature of Figs. 5 and 6 is the similarity between the patterns of total precipitable water and atmospheric absorption—one that would be expected in view of the results of previous work (Gates [2]; Yamamoto [15]; Houghton [6]; and Kimball [9]), among others. The two patterns are remarkably similar over nearly all of the United States, except for the upper Great Lakes region where absorption values are low. This could result from somewhat greater cloudiness in that area. Another explanation could be that surface albedo estimates may not be representative of the surface area seen by the satellite, particularly the snow-covered country to the north. Consideration of a boundary condition of this type would tend to reduce the calculated absorption values for the

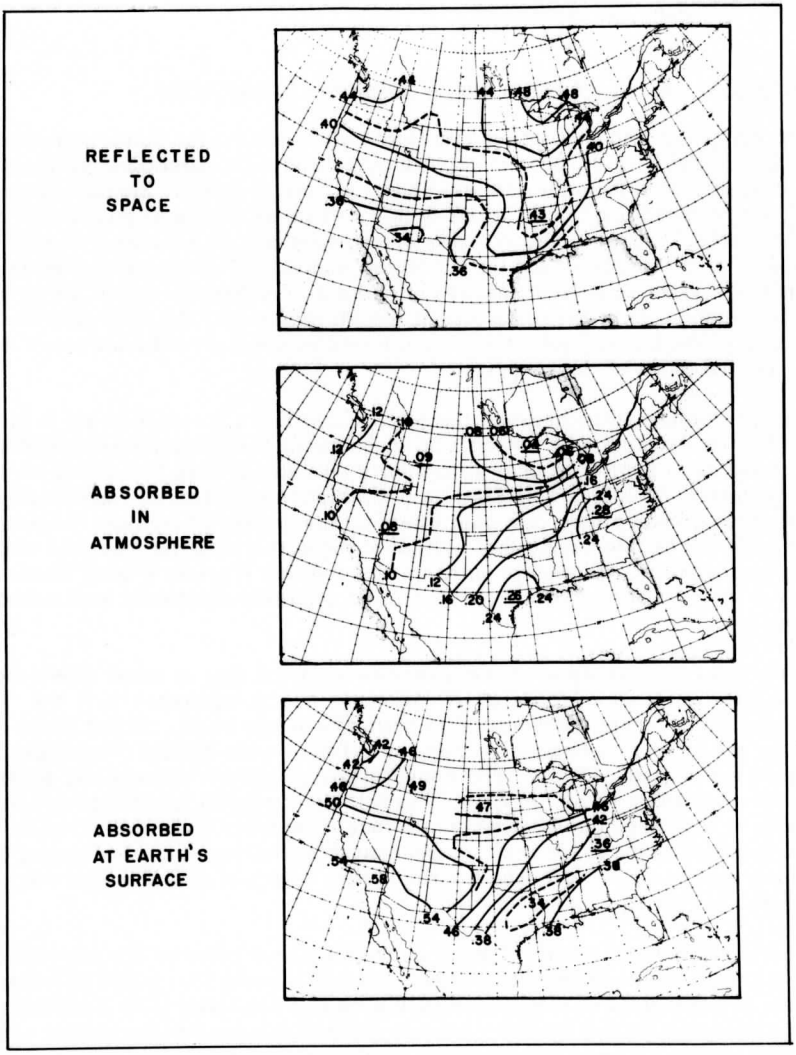

Fig. 5. The reflection and absorption of sunlight during the period March through May, 1962, based on TIROS IV low resolution radiometer and surface radiation data. (Values are fraction of incident sunlight at the top of the atmosphere.)

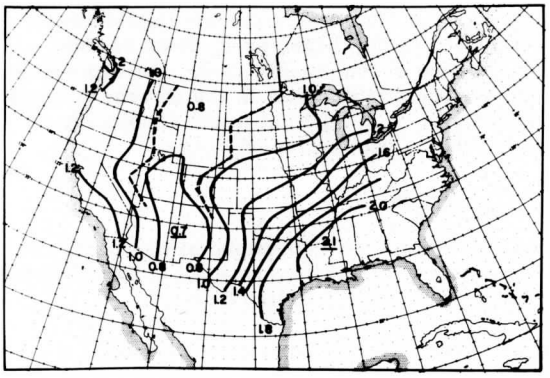

Fig. 6. Total precipitable water (cm) in the atmosphere during the period March through May, 1962. Sampling times correspond to the data illustrated in Fig. 5.

atmosphere. Unfortunately it is not possible to assess the influence of these effects without detailed information on cloudiness associated with the satellite observations.

It is interesting to note in Fig. 5 that absorption in the atmosphere has a considerable variation over the United States, in spite of the smoothing technique used. At the same geographical latitude, absorption varies by a factor of 3 from the minimum values in the Great Basin to the maximum values in southeastern United States. With latitude, it varies by a factor of 7 between the western Great Lakes region and the southeastern United States. It appears that atmospheric absorption has as large a spatial variation as absorption at the ground, and has an even larger variation than the reflection of sunlight to space.

Finally, from the data illustrated in Figs. 5 and 6, overall spatial averages of these terms for the continental United States were derived and summarized in Table 1.

TABLE 1

Average values of partitioning of sunlight over the continental United States during Spring, 1962 (fraction of total incident sunlight)

Reflection to Space, q_r	0.40
Absorbed in Atmosphere, q_a	0.13
Absorbed at ground, q_e	0.47
	1.00
(Total precipitable water	1.19 cm)

Reitan [12] has found that for the period March-May the precipitable water over the entire United States averaged 1.44 cm, based on 11 years of data. When Reitan's data are limited to the area of the present study, the average is 1.39 cm. This indicates the average precipitable water in the present study is low by 0.2 cm, and the fractional absorption of sunlight in the atmosphere is low by about 1 percent in relation to the 11 year period of Reitan.

b. Solar Heating Rate over the United States

The atmospheric absorption values which were determined in this study can be expressed as the amount of heating of an atmospheric column. For the values given in Fig. 5, the resultant heating rate was calculated from

(8) $$\text{Average Heating Rate } (^\circ C/\text{day}) = (g \cdot \bar{Q}_o \cdot q_a)/(10^3 \cdot c_p \cdot \Delta p)$$

$\bar{Q}_o$ is the average for the period March through May for the United States and Δp was taken as 1000 mb. The results shown in Fig. 7 indicate the maximum warming exceeded 0.8°C/day in the moist belt across the southeastern United States. The minimum warming rate of about 0.35°C/day is found over the northern Great Plains and throughout the western mountain region.

5. ABSORPTION OF SUNLIGHT IN THE ATMOSPHERE

There has been considerable work on absorption of solar radiation in the atmosphere based on laboratory measurements (e.g., Yamamoto [15]; Houghton [6]). These studies were concerned with the absorption in a cloudless atmosphere. Yamamoto, and also Houghton, relate absorption to total precipitable water, for an optical airmass of one (i.e., where the solar zenith angle is zero), as shown in Fig. 8, curves 1 and 2.

The absorption values of the present study have been averaged by class intervals of the natural logarithm of u*, in order to provide comparable results to those mentioned above. The results are shown in curve 3 of Fig. 8.

The work of Yamamoto and Houghton show the absorption of sunlight in "artificial" atmospheres which depart from the real case because they:

are cloudless,
are dustless,
have fixed vertical distribution of absorbing constituents, and
have a nonreflecting surface at the lower boundary.

Clearly, the curves in Fig. 8 are not directly comparable. Nevertheless there is significant similarity in the shape of the curves.

The important feature in Fig. 8 is that the absorption of sunlight in an atmosphere with clouds (curve 3) departs from the clear-sky absorption curves

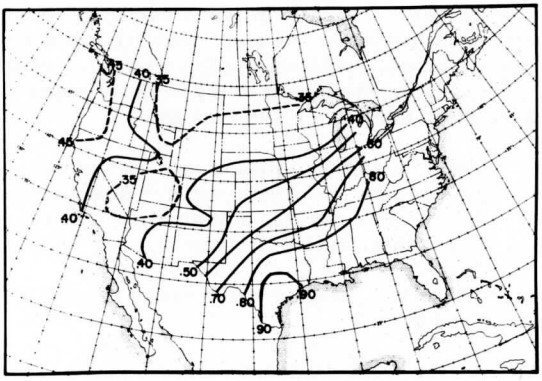

Fig. 7. Atmospheric heating (°C/day) due to absorption of solar radiation in the atmosphere during the period March through May, 1962, based on q_a values of Fig. 5.

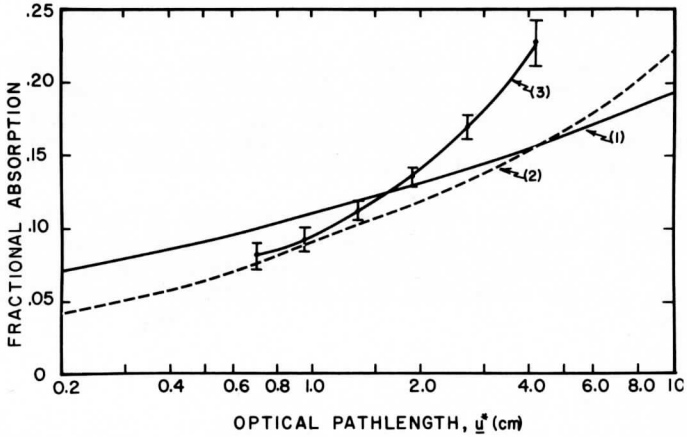

Fig. 8. Absorption of solar radiation in the atmosphere as a function of optical pathlength, u*, in cm.

Curve 1 is the absorption in a clear atmosphere due to H_2O, CO_2 and O_2, from Yamamoto [15].
Curve 2 is the absorption in a clear atmosphere due to H_2O only, from Houghton [6].
Curve 3 is the absorption in the atmosphere over the United States with mixed cloudiness, based on the present study. Brackets indicate the confidence limit of the function values.

(1 and 2) in the region of higher water vapor content. At lower values of water vapor, there is much closer agreement between the curves. Thus, it appears that clear-sky absorption estimates are least applicable in the areas with more moisture (and presumably more cloudiness), and the tendency in these cases is to underestimate the actual absorption that occurs with clouds.

This is particularly important because IR cooling is relatively less in moist, cloudy areas; thus, both the IR and solar radiation have a positive effect on the generation of available potential energy in mid-latitude disturbances. In addition, the solar absorption term is greater than previously thought.

For further studies it is useful to know the function which represents curve 3 (Fig. 8). An approximation was found to be

$$q_a = 0.096 + 0.045(u^*)^{1/2} \cdot \log_e(u^*) \tag{9}$$

The variance of the dependent data from this function is 1.0×10^{-4}.

An example illustrating the use of Eq. (9) has been calculated for 40°N latitude at the time of the vernal equinox. Since both time and position on earth are specified, then the fractional absorption (q_a) and total absorption (Q_a) are simply functions of the optical depth of water vapor. By holding optical depth constant, the fractional and total absorptions are specified as shown in Fig. 9.

The limitations on the use of this example are that: (1) the empirical data obtained over the United States must be used with caution in other areas, e.g., oceanic areas, and (2) optical pathlength is not simply a function of secant of solar zenith angle for atmospheres with clouds, although it may be a good approximation.

REFERENCES

1. A. Angstrom, Atmospheric turbidity, global illumination and planetary albedo of the earth. Tellus, 14, 1962, pp. 435-450.
2. D. M. Gates, Energy Exchange in the Biosphere. Harper and Row Biological Monographs, Harper and Row, New York, N.Y., 1962, 151 pp.
3. A. Danjon, Nouvelles researches sur la photometrie de la lumiere cendree et l'albedo de la terre. Ann. l'Obs. Strasbourg, 3, 1936, pp. 139-181.
4. J. Dubois, La variation de brilliance de la lumiere cendree de la lune au cours du dernier cycle solarie. L'Astronomie (Paris), 69, 1955, pp. 242-246.
5. S. Fritz, P. Krishna Rao and M. Weinstein, Satellite measurements of reflected solar energy and the energy received at the ground. Journal of the Atmospheric Sciences, 21:2, 1964, pp. 141-151.

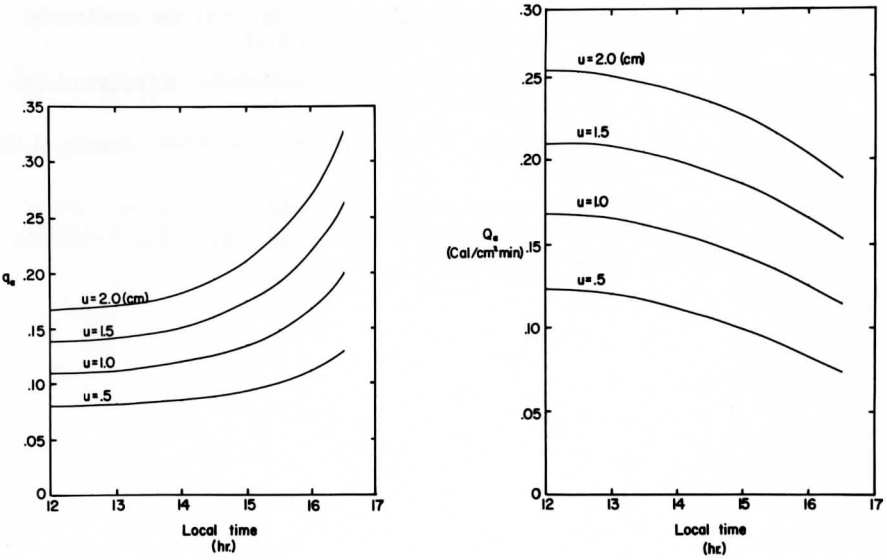

Fig. 9. Fractional absorption (q_a) and total absorption (Q_a) at 40 degrees N. latitude on vernal equinox based on Eq. (9).

6. H. Houghton, On the annual heat balance of the northern hemisphere. Journal of Meteorology, 11:1, 1954, pp. 1-9.

7. F. House, On the interpretation of long-wave radiation data from Explorer VII Satellite, 1963. (Unpublished manuscript)(Copies available from the author)

8. F. House, The radiation balance of the earth from a satellite. Ph. D. thesis, University of Wisconsin, 1965 (unpublished).

9. H. Kimball, Measurements of solar radiation intensity and determination of its depletion by the atmosphere. Monthly Weather Review, 58, 1930, pp. 43-52.

10. E. Kung, R. Bryson and D. Lenschow, Study of a continental surface albedo on the basis of flight measurements and structure of the earth's surface cover over North America. Monthly Weather Review, 92:12, 1964, pp. 543-564.

11. J. London, A study of atmospheric heat balance. Final Report, Contract No. AF19(122)-165, Dept. of Meteorology and Oceanography, New York University, 1957, 99 pp. (OTS No. PB 129551).

12. Reitan, C., Distribution of precipitable water vapor over the continental U. S., Bulletin A. M. S. 41(2), Feb. 1960, pp. 79-87.

13. G. C. Simpson, The distribution of terrestrial radiation. Memoirs of Roy. Meteor. Soc., 3, 23, 1929, pp. 53-78.

14. V. Suomi, The radiation balance of the earth from a satellite, Annals of the IGY, VI, 1958, pp. 33-340.

15. G. Yamamoto, Direct absorption of solar radiation by Atmospheric Water Vapor, Carbon Dioxide and Molecular Oxygen. Journal of the Atmospheric Sciences, 19:2, 1962, pp. 182-188.

ALBEDO OF A STRIATED MEDIUM OF ISOTROPICALLY SCATTERING PARTICLES

by

James A. Weinman and
P. N. Swarztrauber[1]

[1]Affiliation: National Center for Atmospheric Research, Boulder, Colorado

CONTENTS

ABSTRACT

Giovanelli's approximation to the equation of radiative transfer was solved to yield the albedo of an externally illuminated plane-parallel striated medium. The medium was assumed to consist of isotropic scatterers with a scattering coefficient per unit depth:

$$K = K_0 + K_1 \cos(\ell x)$$

that depended periodically on one horizontal coordinate. The albedo computed for $K_1/K_0 = 0$, 0.1 and 0.9 demonstrated a dependence on the angle of incedence of the solar radiance, the mean optical thickness, and the wave length and amplitude of the striations.

INTRODUCTION

The albedo for solar radiation incident on horizontally uniform, plane parallel clouds has been calculated by several authors, notably Fritz (1954), Korb and Möller (1962), and Irvine (1965). Although some inconsistencies exist among these various analyses, they agree in their general conclusions with regard to the dependence of albedo on the angle of incidence of solar radiation, optical thickness of the cloud, and the albedo of the underlying surface.

The upper surfaces of most horizontally stratified clouds and fogs display varying degrees of texture resulting from convection. The present analysis was conducted to ascertain the influence of horizontal inhomogeneity of optical thickness on the albedo of a stratified medium. The optical density of the medium was assumed to vary periodically in one horizontal direction only to simplify this analysis. In order to compute the albedo, a number of simplifying assumptions were made: absorption within the medium was neglected, the incident radiation was assumed uni-directional and the surface beneath the medium was assumed nonreflecting. Although Deirmendjian (1964) showed that drops comprising natural clouds scatter light extremely anisotropically, the present analysis assumed that such scattering was isotropic. In view of these simplifying assumptions, the present results are primarily of heuristic value to indicate the influence of horizontal inhomogeneities on the albedo of clouds.

ANALYSIS

The derivation of the albedo for an inhomogeneous medium proceeds from the three dimensional equation of transfer which provides the radiance, I, as a

function of position and direction. The equation of transfer in cartesian coordinates is

$$(1) \quad \sin\theta \cdot \cos\Phi \frac{\partial I}{\partial x} + \sin\theta \cdot \sin\Phi \frac{\partial I}{\partial y} - \cos\theta \frac{\partial I}{\partial z} = -K\{I - J - \frac{F}{4}\exp(-KZ/\mu_0)\}$$

according to Chandrasekhar (1950). The origin of the coordinate system is at the upper surface of the turbid medium, and the z coordinate increases in the nadir direction. The azimuth angle, Φ, increases from the horizontal x axis, and the angle θ is measured from zenith, the negative z coordinate. The source function J is

$$J \equiv \frac{1}{4\pi} \int_0^{4\pi} I \, d\Omega$$

All irradiance, πF, incident on the surface $z = 0$, is assumed unidirectional at an angle $\cos^{-1}(\mu_0)$ with respect to the z axis.

Giovanelli (1959) proposed that the solution, I, of Eq. (1) is of the form:

$$(2) \quad I = \sum_{n=0}^{\infty} [I_n P_n(\cos\theta) + \sum_{m=1}^{\infty} \{a_n^m \cos(m\Phi) + b_n^m \sin(m\Phi)\} P_n^m(\cos\theta)]$$

where $P_n(\cos\theta)$ and $P_n^m(\cos\theta)$ are the Legendre polynomials and associated Legendre functions. The I_n, a_n^m and b_n^m are appropriate amplitudes depending on x, y, and z.

Substituting Eq. (2) in Eq. (1), integrating over Φ from 0 to 2π, and dividing the result by 2π provides:

$$(3) \quad -\cos\theta \frac{\partial}{\partial z}\left\{\sum_{n=0}^{\infty} I_n P_n(\cos\theta)\right\} + \frac{1}{2}\sin\theta \cdot \left\{\sum_{n=1}^{\infty}\left(\frac{\partial a_n^1}{\partial x} + \frac{\partial b_n^1}{\partial y}\right) P_n^1(\cos\theta)\right\}$$

$$= -K\left\{\sum_{n=0}^{\infty} I_n P_n(\cos\theta) - J - \frac{F}{4}\exp(-KZ/\mu_0)\right\}$$

Multiplying Eq. (3) by $P_m(\cos\theta)$ and integrating over θ from π to $-\pi$ yields:

$$(4a) \quad -\frac{1}{3}\frac{\partial I_1}{\partial z} + \frac{1}{3}\frac{\partial a_1^1}{\partial x} + \frac{1}{3}\frac{\partial b_1^1}{\partial y} = \frac{KF}{4}\exp(-KZ/\mu_0)$$

$$(4b) \quad -\frac{\partial I_0}{\partial z} + \frac{2}{5}\frac{\partial I_2}{\partial z} + \frac{3}{5}\left(\frac{\partial a_2^1}{\partial x} + \frac{\partial b_2^1}{\partial y}\right) = -KI_1$$

If I_2, a_2^1 and b_2^1 are assumed negligible, Eq. (4b) is

$$\frac{\partial J}{\partial z} = KI_1 \tag{4c}$$

where $I_0 \equiv J$.

Inserting Eq. (2) into Eq. (1) multiplied by $\cos\phi$, integrating the product over ϕ from 0 to 2π, and integrating that equation over $\neq$ from 0 to π, yields:

$$\frac{\partial J}{\partial x} = -Ka_1^1 \tag{5}$$

Similarly, by inserting Eq. (2) into Eq. (1) multiplied by $\sin\phi$, integrating the product over ϕ from 0 to 2π, and integrating that equation over θ from 0 to π, yields:

$$\frac{\partial J}{\partial y} = -Kb_1^1 \tag{6}$$

Combining Eqs. (4a), (4c), (5) and (6) yields:

$$\frac{1}{K}\nabla\cdot\left(\frac{1}{K}\nabla J\right) = -\frac{3F}{4}\exp(-KZ/\mu_0) \tag{7}$$

The albedo, A, is derived from Eq. (2) by

$$A \equiv \int_0^{2\pi}\int_0^{\pi/2} I\cdot\cos\theta\cdot\sin\theta\cdot d\theta d\phi/(\pi\mu_0 F) \tag{8}$$

This is approximated by

$$A(x,y) \simeq 2\left[J + \frac{1}{3^{1/2}K}\frac{\partial J}{\partial z}\right]\Bigg|_{z=0} \Big/ (3^{1/2}\cdot\mu_0 F) \tag{8a}$$

where all I_n with $n > 1$ are neglected.

The scattering coefficient per unit length, K, is chosen to vary periodically in one horizontal direction only, i.e.:

$$K(x) = K_0 + K_1\cos(\ell x) \tag{9}$$

For a medium with this scattering coefficient, the solution of the transfer equation is periodic in x with a wavelength $2\pi/\ell$. Thus we can expand the terms of Eq. (2):

$$\left.\begin{aligned} I_n &= \sum_{s=0}^{\infty} I_{n,s}\cdot\cos(s\ell x) \\ a_n^m &= \sum_{s=0}^{\infty} a_{n,s}^m\cdot\cos(s\ell x) \end{aligned}\right\} \tag{2a}$$

$$b_n^m = \sum_{s=0}^{\infty} b_{n,s}^m \cdot \cos(s\ell x)$$

where $I_{n,s}$, $a_{n,s}^m$, and $b_{n,s}^m$ depend on z only.

Inserting Eqs. (2a) into Eq. (3), dividing both sides by $2\pi/\ell$, and integrating both sides of Eq. (3) over x from 0 to $2\pi/\ell$ yields the equation of transfer determining the radiance averaged over a horizontal wavelength. Thus:

$$-\cos\theta \frac{\partial}{\partial z} \sum_{n=0}^{\infty} I_{n,0} \cdot P_n(\cos\theta) \simeq -K_0\left[\sum_{n=1}^{\infty} \{I_{n,0} + (K_1/2K_0)I_{n,1}\} \cdot P_n(\cos\theta)\right]$$

(3a)

$$+\frac{K_0 F}{4}\left[1 - \frac{1}{2}\{K_1/K_0\}^2 \cdot \{K_0 Z/\mu_0 - \frac{1}{2}(K_0 Z/\mu_0)^2\} + \ldots\right] \exp(-K_0 Z/\mu_0)$$

The radiance averaged over a horizontal wavelength, $\frac{\ell}{2\pi}\int_0^{2\pi/\ell} I\,dx$, is thus independent of ℓ. Furthermore, for $K_1/K_0 < 1$, the horizontally averaged radiance is approximately equal to the radiance in a homogeneous medium. Equation (8) then indicates that the horizontally averaged albedo approaches the albedo of a homogeneous medium, i.e.:

$$\lim_{K_1/K_0 \to 0} \frac{\ell}{2\pi}\int_0^{2\pi/\ell} A[\{K_0 + K_1 \cos(\ell x)\}Z_0/\mu_0]dx = A[K_0 Z_0/\mu_0]$$

Equation (3a) shows that the average value of the albedo is also independent of the horizontal wavelength of the striations, $2\pi/\ell$, irrespective of the amplitude of these striations.

The albedo was calculated from Eqs. (7) and (8a) by the following methods:

1) Eddington's approximation was utilized to provide the albedo in the limiting case of a homogeneous medium as a reference for subsequent calculations ($K_1/K_0 = 0$).

2) Giovanelli's approximation was solved analytically to provide the albedo of a medium with small density perturbations ($K_1/K_0 < 1$).

3) Giovanelli's approximation was solved numerically to provide the albedo of a medium with deep horizontal density striations ($K_1/K_0 \simeq 1$).

1. Eddington's Approximation, $K_1/K_0 = 0$

Eddington's approximation to the equation of transfer in a homogeneous medium with $K_1/K_0 = 0$ requires that $J(z)$ satisfies:

$$\frac{1}{K_0^2}\frac{d^2J}{dz^2} = -\frac{3F}{4}\exp(-K_0 Z/\mu_0) \tag{7a}$$

according to Chandrasekhar (1950). The source function, $J(z)$, is subjected to the boundary conditions.

$$J(0) = \left.\frac{dJ}{dz}\right|_{z=0} \Big/ (3^{1/2}\cdot K_0)$$
$$J(z_0) = -\left.\frac{dJ}{dz}\right|_{z=z_0} \Big/ (3^{1/2}\cdot K_0) \tag{10a}$$

These conditions are equivalent to the statement that no diffuse radiance is incident on the upper and lower boundaries of the medium.

Inserting the solution of (7a) subjected to the boundary conditions (10a) into Eq. (8a) yields the albedo A:

$$A = 1 - [\mu_0\{1 - \exp(-K_0 Z_0/\mu_0)\} + 3^{-1/2}\cdot\{1 + \exp(-K_0 Z_0/\mu_0)\}]/$$
$$[K_0 Z_0 + 2\cdot 3^{-1/2}] \tag{8b}$$

The solutions to Eq. (8b) are presented in Figure 1 for $\mu_0 = 1.000$, i.e., where the sun is directly overhead, and for $\mu_0 = .1737$, i.e., where the sun is near the horizon. The results of Eq. (8b) are compared with the albedo calculations of Fritz (1954) for clouds of anisotropically scattering drops. The present analysis assumes that the scattering phase function is isotropic. At grazing incidence, $\mu_0 = .1737$, agreement between the two calculations is moderately good because the anisotropy of the phase function is manifest in the horizontal direction and thus it has little effect on the upward directed irradiance. However, at normal incidence, $\mu_0 = 1.000$, albedo calculated by the present method is somewhat large; this is a consequence of the isotropic phase function which scatters too much light in the backward direction. We may thus have confidence in the qualitative conclusions that Eddington's approximation provides with respect to the dependence of albedo on optical thickness, $K_0 Z_0$ and solar angle, $\cos^{-1}(\mu_0)$, for a horizontally homogeneous cloud.

2. Giovanelli's Approximation for a Medium with Small Horizontal Density Perturbations, $K_1/K_0 < 1$.

Whereas Case 1 was a one-dimensional problem, we now consider a medium with the scattering coefficient given by Eq. (9) with $K_1/K_0 = 0.1$. The source function $J(z, x)$, satisfying Eq. (7) is represented by the approximation:

$$J(x, z) \simeq J_0(z) + J_1(z)\cdot\cos(\ell x)$$

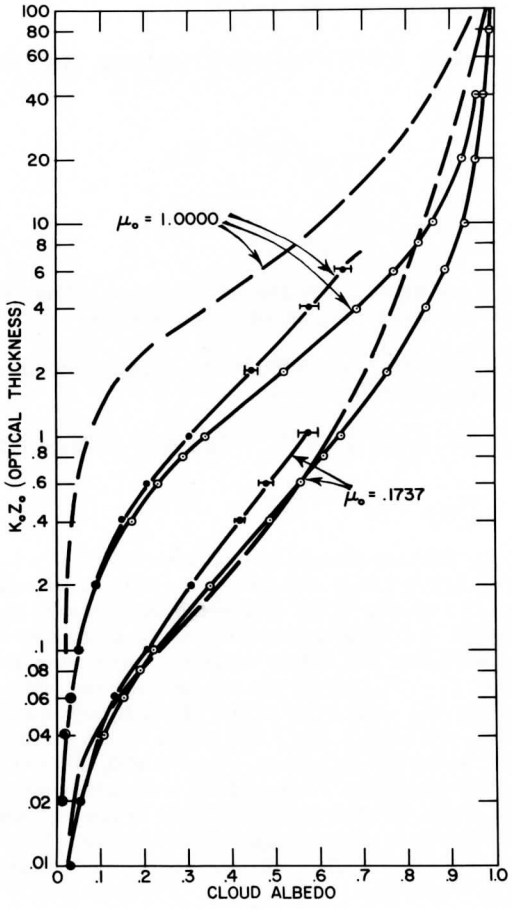

Fig. 1. Albedo computed by Fritz (1954) for a horizontally homogeneous plane parallel medium utilizing a diffusion model incorporating a forward scattering phase function, ----. Albedo of a homogeneous medium computed by Eddington's approximation utilizing an isotropic phase function, from Eq. (8b), —— ⊙ ——. Mean albedo, A_0, for a striated medium with $K_1/K_0 = 0.9$ computed from Eq. (8d), —— ● ——.

Equation (7) is expanded in terms of $\cos(s\ell x)$, the coefficients for $s = 0$ and 1 respectively satisfy:

$$\frac{d^2 J_0}{dz^2} = (\ell^2 K_1/2K_0) J_1 - \frac{3}{4} K_0^2 F \exp(-K_0 Z/\mu_0) \tag{7b}$$

$$\frac{d^2 J_1}{dz^2} = \ell^2 J_1 + \frac{3}{4} K_0 K_1 F \left[(K_0 Z/\mu_0) - 2\right] \exp(-K_0 Z/\mu_0) \tag{7c}$$

Because $K_1/K_0 \ll 1$, $\exp[-(K_1 Z/\mu_0)\cos(\ell x)]$ is approximated only by the first two terms of its series expansion in these equations.

The source function, $J(z, x)$, is subjected to the boundary conditions:

$$J(0, x) = \left.\frac{\partial J}{\partial z}\right|_{z=0} \Big/ [3^{1/2} \cdot K(x)]$$

$$J(z_0, x) = -\left.\frac{\partial J}{\partial z}\right|_{z=z_0} \Big/ [3^{1/2} \cdot K(x)] \tag{10b}$$

for all x. These boundary conditions impose the restriction that no diffuse radiance is incident on either boundary of the medium.

The albedo, $A(x)$, derived from Eq. (8a) then has the periodic form:

$$A(x) = A_0 + A_1 \cos(\ell x) \tag{8c}$$

The introduction of a periodic perturbation with $K_1/K_0 = 0.1$ permits A_0 to remain virtually unaltered from the value given by Eq. (8b); this agrees with conclusions drawn from Eq. (3a). Isopleths of constant variability of the albedo, $A_1/A_0 \times 100$, are presented as a function of $K_0 Z_0$ and $\ell\mu_0/K_0$ in Figs. (2a) and (2b) for $\mu_0 = 1.000$ and $\mu_0 = .1737$ respectively.

3. Giovanelli's Approximation for a Medium with Deep Horizontal Density Striations, $K_1/K_0 \simeq 1$.

The scattering coefficient per unit length, $K(x)$, of Eq. (9) is now assumed to be deeply striated with $K_1/K_0 = 0.9$. The periodic variation of $K(x)$ can no longer be treated as a perturbation; the solution, $J(z, x)$ of Eq. (7) is therefore obtained by numerical means. The symmetry of this problem adds the boundary condition on $J(z, x)$:

$$\frac{\partial J}{\partial x} = 0 \quad \text{for } x = 0 \text{ and } \pi/\ell \text{ for all } z \tag{10c}$$

in addition to those already cited in (10b).

The function J is evaluated at mesh point i, j of a mesh placed on the region $\{(z, x),\ 0 \le z \le z_0,\ 0 \le x \le \pi/\ell\}$. The mesh point i, j corresponds to $[(i-1)\Delta z,\ (j-1)\Delta x]$ where Δz and Δx are mesh widths in the z and x directions respectively. Thus $\Delta z = z_0/(L-1)$ and $\Delta x = \pi/(M-1)$, and

$$j = 1, 2, \ldots, L$$

$$j = 1, 2, \ldots, M$$

Virtual mesh points are also placed outside the region in order that the Neumann type boundary conditions can be center differenced. Hence

$$i = 0, 1, 2, \ldots, L + 1$$

$$j = 0, 1, 2, \ldots, M + 1$$

A solution for J_{ij} comprising a total of $LM + 2(L+M)$ points is sought at all but the corner points. In order to do this the $LM + 2(L+M)$ equations are required.

The elliptical partial differential Eq. (7) is thus written as LM equations, in difference form:

$$\frac{J_{i,j+1} - 2J_{i,j} + J_{i,j-1}}{\Delta x^2} + \frac{J_{i+1,j} - 2J_{i,j} + J_{i-1,j}}{\Delta z^2} + g_j\left(\frac{J_{i,j+1} - J_{i,j-1}}{2\Delta x}\right) + f_{i,j} = 0 \tag{7'}$$

where $g_j = K_1 \ell \sin[(j-1)\Delta x]/\{K_0 + K_1 \cos[(j-1)\Delta x]\}$ and

$$f_{i,j} = \frac{3}{4} F\{K_0 + K_1 \cos[(j-1)\Delta x]\}^2 \cdot \exp\{-[K_0 + K_1 \cos[(j-1)\Delta x]] \cdot [(i-1)\Delta z]/\mu_0\} \qquad i = 1, \ldots, L \qquad J = 1, \ldots, M$$

An additional M equations are obtained from the boundary conditions at $z = 0$.

$$J_{1,j} = \frac{J_{2,j} - J_{0,j}}{3^{1/2} \cdot 2\Delta z \cdot [K_0 + K_1 \cos(j\Delta x)]} \qquad j = 1, \ldots, M \tag{10b'}$$

The boundary conditions at $z = z_0$ also provide M additional equations:

$$J_{L,j} = \frac{J_{L-1,j} - J_{L+1,j}}{3^{1/2} \cdot 2\Delta z \cdot [K_0 + K_1 \cos(j\Delta x)]} \qquad j = 1, \ldots, M \tag{10c'}$$

The boundary conditions at $x = 0$ provide L equations:

$$\frac{J_{i,2} - J_{i,0}}{2\Delta x} = 0 \qquad i = 1 \ldots L$$

The boundary conditions at $x = \pi/\ell$ provide L additional equations:

$$\frac{J_{i,M+1} - J_{i,M-1}}{2\Delta x} = 0 \qquad i = 1 \ldots L$$

This gives the required number of equations. A solution to this system was obtained by relaxation. In general, problems which involve Neumann type boundary conditions result in difference equations which relax slower than problems having Dirichlet boundary conditions. The point relaxation scheme for this system is too slow to render solution by that method feasible. The line relaxation scheme which is somewhat better is outlined below:

The point relaxation, at any given pass and at any point, assumes that the value at all other points is known. It is then a simple process to solve the difference equation for the one unknown, namely the value of the function at the point under consideration. The process then moves to the next point with a similar computation. In the line relaxation scheme at any given pass and at the line* under consideration, it is assumed that the value of the function is known at all points except on that line. A system of equations is then produced for the values of the function on that line.

This system, which is of the order of $L + 2$ or $M + 2$ depending on which direction the line is taken, is then solved for the values of the function on this line. The relaxation proceeds to the next line and a similar computation gives new values on that line. After all lines are relaxed, a convergence criterion is examined and if it fails the process is repeated, Varga (1962).

The difference equation is thus written in a form suitable for line relaxation in the j or x direction.

$$\left(\frac{g_j}{2\Delta x} - \frac{1}{\Delta x^2}\right) J_{i,j-1} + \left(\frac{2}{\Delta z^2} + \frac{2}{\Delta x^2}\right) J_{ij} + \left(-\frac{1}{\Delta x^2} - \frac{g_j}{2\Delta x}\right) J_{i,j+1} =$$

$$\frac{J_{i+1,j} + J_{i-1,j}}{\Delta z^2} + f_{ij}$$

This set of equations plus the boundary conditions

$$J_{i,2} = J_{i,0} \text{ and } J_{i,M+1} = J_{i,M-1}$$

*A line is considered to be the set of points having the same row on column index, depending which direction is chosen.

provide a total of $M+2$ equations in the $M+2$ unknowns:

$$J_{i,0},\ J_{i,1},\ \cdots,\ J_{i,M+1}$$

This system of equations is of a particular form, however, which lends itself well to a numerical solution.

If

$$A_j = \frac{g_j}{2\Delta x} - \frac{1}{\Delta x^2}$$

$$B_j = \frac{2}{\Delta z^2} + \frac{2}{\Delta x^2}$$

$$C_j = \frac{1}{\Delta x^2} - \frac{g_j}{2\Delta x}$$

$$Y_j = \frac{J_{j+1,j} + J_{i-1,j}}{\Delta z^2} + f_{ij}$$

then the system of equations has the form:

$J_{i,0}$	$J_{i,1}$	$J_{i,2}$	$J_{i,3}$	$\cdots$	$J_{i,M-2}$	$J_{i,M-1}$	$J_{i,M}$	$J_{i,M+1}$	Right Side
1		(-1)							$= 0$
A_1	B_1	C_1							$= Y_1$
	A_2	B_2	C_2						
					A_{M-1}	B_{M-1}	C_{M-1}		$= Y_{M-1}$
						A_M	B_M	C_M	$= Y_M$
						(1)		-1	$= 0$

This system is almost in a form suitable for application of the algorithm considered in the appendix to this paper.

In order to obtain tridiagonal form, the two circled coefficients are eliminated. The top one is eliminated by subtracting a suitable multiple of the second equation, and the bottom is handled analogously. The resulting equations are then solved by using the algorithm.

In this manner all values of the function on any given line are computed. For lines $i = L + 1$ and $i = 0$ a different set of equations must be solved which utilize the boundary conditions at $z = 0$ and z_0.

The code which was developed found that line relaxation in the j direction which has just been discussed was slightly better than point relaxation. However, when line relaxation was alternately applied in the i direction and then the j direction, the convergence was markedly improved. However, this was primarily a result of the line relaxation in the i direction being effective rather than the alternating method itself. This is due to the equations being highly coupled in the i direction.

Over relaxation was found to be effective. However, for a problem of this complexity the degree of over relaxation cannot be analytically computed. The method of trial and error for determining this degree was unsatisfactory since each change of equation parameters required a different value of over relaxation. Therefore a conservative estimate of over relaxation was used throughout the computation.

The accuracy of the solution was established in two ways:

1. The program coding was checked by substituting the solution directly into the difference equation in a computation independent of the main program.

2. The accuracy of the difference scheme was checked by reducing the grid intervals and comparing the two solutions. It was found that due to the wide range of values that the equation parameters assumed that some problems required grid sizes much smaller than others. In order to make the computations economical, the grid size in the i direction was computed from equation parameters.

The criterion for computing the grid size in the i direction was based on the fact that the equation was highly coupled in that direction.

The relative error in the difference formula for J_{zz} is of the form:

$$\frac{h^2 J_{zzzz}}{12\, J_{zz}} \quad \text{where } h \text{ is mesh width.}$$

Now due to the coupling in the i direction we can assume from the differential equation that $J_{zz} \cong f(x, z)$. Substituting this relation into the error term we obtain an approximate expression for the relative error.

$$\frac{h^2 f_{zz}}{12\, f}$$

For a relative error less than some t, the h is given by the expression

$$h = \left(\frac{12\, f t}{f_{zz}}\right)^{1/2}$$

Upon finding a suitable solution, $J_{i,j}$, to Eq. (7') the albedo is computed from

$$A_j = 4 \cdot J_{1,j} / (3^{1/2} \mu_0 F) \tag{8a'}$$

where this expression is obtained by combining the boundary condition (10b) at $z = 0$ with Eq. (8a).

The albedo thus obtained is then approximated by Fourier series to facilitate graphical display of the results:

$$A_j \simeq \sum_{s=0} A_s \cdot \cos[s(j-1)\Delta x] \tag{8d}$$

The albedo averaged over a horizontal wave-length, A_0, shown in Figure 1, is reduced to $\simeq$ 90% of the albedo computed from Eq. (8b). The average albedo demonstrates an increased dependence on $\ell\mu_0/K_0$ as the optical thickness increases, this is indicated by the horizontal bars of Figure 1. However, Eq. (3a) showed that A_0 must be independent of ℓ. This suggests that Giovanelli's approximation becomes invalid for $K_0Z_0 \gtrsim .9$ when $\mu_0 = .1737$, and for $K_0Z_0 \gtrsim 6$ when $\mu_0 = 1.0000$.

RESULTS AND DISCUSSION

The average albedo, A_0, of a medium with $K_1/K_0 = 0.1$ has values that are 98% of the value determined by Eq. (8b) for a uniform medium. This is in agreement with the conclusion drawn from Eq. (3a).

Figures (2a) and (2b) show the variability in albedo $100 \cdot (A_1/A_0)$ for a cloud with $K_1/K_0 = 0.1$ as a function of K_0Z_0, and $\ell\mu_0/K_0$ for $\mu_0 = 1.0000$ and $\mu_0 = .1737$ respectively. The albedo of very thin media, with $K_0Z_0 < 1$ varies in direct proportion to the magnitude of the perturbation, i.e., $A_1/A_0 \simeq K_1/K_0 = 0.1$ if the wave length of the striations is large compared to the slant optical thickness, i.e., $\ell\mu_0/K_0 < 1$. If on the other hand the wave length of the horizontal perturbation, $2\pi/\ell$, becomes small compared to the slant optical thickness, i.e., $\ell\mu_0/K_0 > 1$, light will penetrate several striations before being scattered back out of the cloud. This has the effect of averaging the effect of the striations such that $A_1/A_0 < 0.1$. As the medium becomes thicker, the albedo becomes less sensitive to any changes in optical thickness. The oscillating part of scattering coefficient therefore has a diminishing influence on the albedo as K_0Z_0 increases.

The average albedo of a medium with $K_1/K_0 = 0.9$ of Eq. (8d) is reduced to $\simeq$ 90% of the albedo for a uniform medium determined by Eq. (8b), provided that $K_0Z_0 \leq 6$.

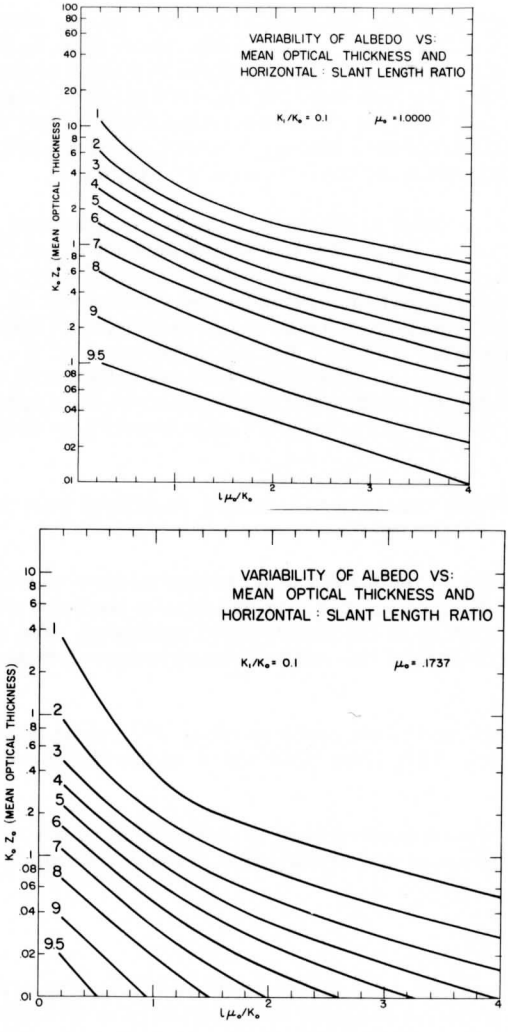

Fig. 2. Isopleths of variability of albedo, $100 \cdot (A_1/A_0)$ as a function of mean optical thickness, $K_0 Z_0$, and slant length ratio, $\ell\mu_0/K_0$, for $K_1/K_0 = 0.1$.
a. $\mu_0 = 1.0000$.
b. $\mu_0 = .1737$

In Figure (3a) and (3b), the variation in albedo, A_1/A_0, shows the same general dependence on K_0Z_0 and $\ell\mu_0/K_0$ for clouds with $K_1/K_0 = 0.9$ as it showed for those with $K_1/K_0 = 0.1$. The absolute values of the second and higher order harmonics are less than $.1 \cdot A_0$, except in the limited domain indicated in Figures (3a) and (3b). The second harmonic is only comparable to the first as the medium becomes thicker, and the striations acquire finer structure; this is a manifestation of the formation of shadows.

The formation of shadows is contrary to the assumption that I_2, a_2^1 and b_2^1 are negligible in Eq. (4b). The increasing dependence of the mean albedo, A_0 of Eq. (8d), on ℓ as K_0Z_0/μ_0 exceeds 6 is contrary to the prediction of Eq. (3a). This suggests that the neglect of the coefficients of $P_2(\cos\theta)$ and $P_2^m(\cos\theta)$ in Eq. (2) renders Giovanelli's approximation somewhat questionable for optically thick media. The fact that the dependence of A on ℓ occurs for thinner media when $\mu_0 = .1737$ (grazing solar incidence) than when $\mu_0 = 1.000$ (sun at zenith) lends additional support to the suggestion that shadows limit the validity of Giovanelli's approximation to determine cloud albedo.

The most significant conclusions that may be derived from this investigation are:

1) The mean value of the albedo of a striated medium of isotropic scatterers with $K_0Z_0/\mu_0 \lesssim 6$ depends on K_0Z_0 in essentially the same manner as it does in a homogeneous medium of the same optical thickness. The mean value of the albedo is independent of the width of the striations irrespective of their amplitude.

2) Striations with horizontal scale lengths, ℓ^{-1}, short compared to the vertical scale length, K_0^{-1}, have little effect on the albedo of a stratified medium.

3) The albedo of a striated medium is proportional to the density of scatterers only in the limits of an optically thin, broadly striated cloud.

ACKNOWLEDGMENTS

One of the authors (J.A.W.) wishes to thank Dr. John W. Firor and Professor Julius London for providing him with the opportunity to investigate most of this problem at the High Altitude Observatory of N.C.A.R. Some of the programs employed in this study were written by Messrs. Fred N. Alyea and Peter Guetter. Their cooperation is gratefully acknowledged.

Part of this investigation was also supported by funds from Environmental Sciences Service Administration grant W.B.G. 27.

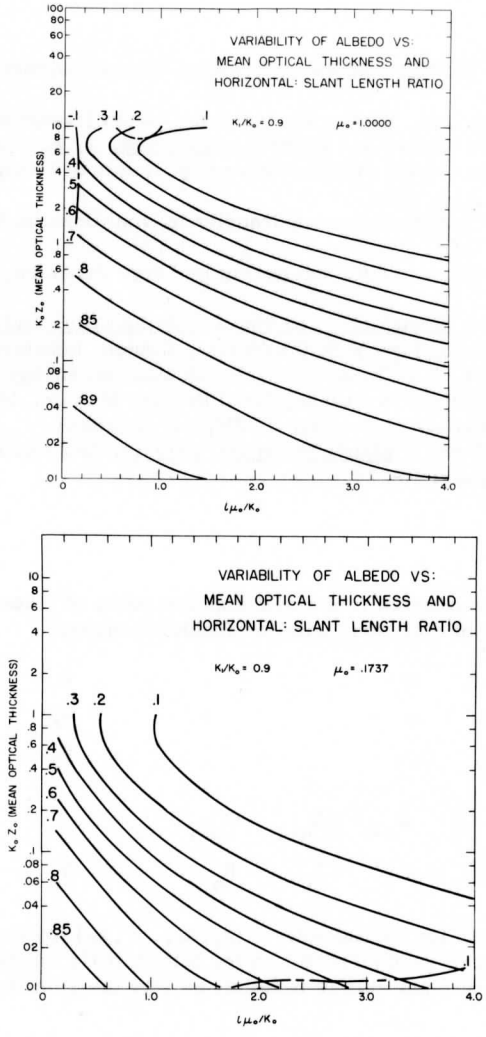

Fig. 3. Isopleths of variability of albedo, A_1/A_0, ———, A_1/A_0, — - —, as a function of mean optical thickness, $K_0 Z_0$ and slant length ratio, $\ell \mu_0 / K_0$, for $K_1/K_0 = 0.9$. Note that $|A_1/A_0| < 0.1$ throughout most of the domain considered in this analysis.

a. $\mu_0 = 1.0000$
b. $\mu_0 = .1737$.

REFERENCES

Chandrasekhar, S. (1950), Radiative Transfer, Oxford University Press, pp. 9, 330-331.

Deirmendjian, D. (1964), Scattering and Polarization Properties of Water Clouds and Hazes in the Visible and Infrared, Appl. Opt. 3, p. 187.

Fritz, S. (1954), Scattering of Solar Energy by Clouds of "Large Drops," J. Meteorol., 11, p. 291.

Giovanelli, R. G. (1959), Radiative Transfer in Non-Uniform Media, Aust. J. of Phys. 12, p. 164.

Irvine, W. M. (1965), Multiple Scattering by Large Particles, Ap. J., 142, p. 1563.

Isaacson, E. (1956), Introduction to Applied Mathematics and Numerical Analysis (Lecture Notes), New York University, Courant Institute, pp. 224-233.

Korb, G. and Möller, F., Theoretical Investigation on Energy Gain by Absorption of Solar Radiation in Clouds, Final Report, Munich, Meteorologisches Inst., L. Maximillian University (ASTIA, AD #292924).

Varga, Richard S. (1962), Matrix Iterative Analysis, Englewood Cliffs, N.J., Prentice Hall, pp. 194-239.

APPENDIX

The following discussion is derived from the notes of Isaacson (1956): Consider a system of equations with the following matrix:

$$\begin{pmatrix} B_1 & C_1 & 0 & 0 & & & \\ A_2 & B_2 & C_2 & 0 & & & \\ 0 & A_3 & B_3 & C_3 & & & \\ & & \cdots & & & & \\ & & A_{n-1} & B_{n-1} & C_{n-1} & & \\ & & 0 & A_n & B_n & & \end{pmatrix} = \begin{pmatrix} Y_1 \\ Y_2 \\ Y_3 \\ \vdots \\ Y_n \end{pmatrix}$$

To solve this system for the unknowns $(x_1, x_2, \ldots, x_n)$ by the elimination method, the matrix is triangularized on the left with 1's on the main diagonal, i.e., this system of equations is transformed into the system whose matrix is:

$$
\begin{array}{ccccccc}
1 & D_1 & 0 & & & & \\
0 & 1 & D_2 & . & & & \\
 & . & 1 & D_3 & . & & \\
 & & . & . & . & . & \\
 & & & . & . & . & \\
 & & & & . & . & 0 \\
 & & & & & 1 & D_{N-1} \\
 & & & & & 0 & 1
\end{array}
=
\begin{array}{c}
W_1 \\ W_2 \\ W_3 \\ . \\ . \\ . \\ \\ W_n
\end{array}
$$

This is accomplished by dividing the first equation by the coefficient of x_1 in the first equation,

$$D_1 = \frac{C_1}{B_1}, \quad W_1 = \frac{Y_1}{B_1},$$

By eliminating x_1 from the second equation and dividing by the coefficient of x_2 in the second equation,

$$D_2 = \frac{C_2}{B_2 - A_2 D_1} \qquad W_2 = \frac{Y_2 - A_2 W_1}{B_2 - A_2 D_1}$$

. . . etc.

$$D_k = \frac{C_k}{B_k - A_k D_{k-1}} \qquad W_k = \frac{Y_k - A_k W_{k-1}}{B_k - A_k D_{k-1}} \qquad \text{(a)}$$

for $2 \leq k \leq N-1$

If $D_0 = 0$ and $W_0 = 0$, then (a) holds for D_k,

$1 \leq k \leq N-1$ while since

$$W_N = \frac{Y_N - A_N W_{N-1}}{B_N - A_N D_{N-1}}$$

This formula holds for W_k, $1 \leq k \leq N$.

Once the W_k's and the D_k's are derived, the x_k's can be obtained from

$$
\begin{aligned}
x_N &= W_N \\
x_{N-1} &= W_{N-1} - D_{N-1}\, x_N \\
&\vdots \qquad\qquad \vdots \\
w_k &= W_k - D_k\, x_{K+1} \\
&\vdots \qquad\qquad \vdots
\end{aligned}
\tag{b}
$$

By introducing the notation

$$x_{N+1} = 0, \quad D_N = 0,$$

formula (b) will be good for $1 \leq k \leq N$.

THE THEORETICAL BASIS FOR LOW-RESOLUTION RADIOMETER MEASUREMENTS FROM A SATELLITE

by

Verner E. Suomi
Kirby J. Hanson
and
Thomas H. Vonder Haar

CONTENTS

LIST OF SYMBOLS

Symbols	Meaning	Units
ROMAN LETTERS		
a	Radius of spherical sensor	(cm)
A	Equals r/(r+h)	-
ALB	Albedo	-
B	Subscript denoting black sensor	-
C_0	Conduction constant	(cal sr/cm^2 min °C)
C_L	Lag constant	(cal sr/cm^2 min °C)
C_M	Mirror constant	(sr)
D*	Difference in energy gain ($E_B^* - E_W^*$)	(cal sr/cm^2 min)
E_B	Total energy gain by black sensor	(cal sr/cm^2 min)
E_B^*	Energy gain by black sensor at day side of terminator	(cal sr/cm^2 min)
E_W	Total energy gain by white sensor	(cal sr/cm^2 min)
E_W^*	Energy gain by white sensor at day side of terminator	(cal sr/cm^2 min)
$E_{W_{day}}$	Energy gain by white sensor at day side of terminator	(cal sr/cm^2 min)
$E_{W_{night}}$	Energy gain by white sensor at night side of terminator	(cal sr/cm^2 min)
$E(\lambda)$	Radiant energy in spectral interval $d\lambda$	(cal/micron)
$f(\lambda)$	Spectral radiant power	(cal sr/min micron)
f	Radiant power, incident on spherical sensor from specified source	(cal sr/min)
f_{rs}	Radiant power incident on spherical sensor from reflected solar radiation from earth	(cal sr/min)
f_{LW}	Radiant power incident on spherical sensor from IR radiation from earth	(cal sr/min)

h	height of satellite at point (P) above point (S) on earth's surface	
$H(\lambda)$	Spectral irradiance	(cal/cm^2 min micron)
H'	Irradiance at point (P), from specified source	(cal/cm^2 min)
$H_{LW'}$	Outward IR irradiance from earth at point (P)	(cal/cm^2 min)
$H_{rs'}$	Reflected solar irradiance from earth at point (P)	(cal/cm^2 min)
H	Irradiance at standard level (30km) from specified source	(cal/cm^2 min)
$I(\omega, \lambda)$	Radiance	(cal/cm^2 min sr micron)
I_{LW}	Outward IR radiance from earth	(cal/cm^2 min sr)
I_{rs}	Reflected solar radiance from earth	(cal/cm^2 min sr)
I_s	Parallel beam radiation from sun	(cal/cm^2 min)
K_C	Conduction constant	(cal sr/cm^2 min °C)
K_L	Lag constant	(cal sr/cm^2 min °C)
K_M	Mirror constant	(sr)
LW	Subscript denoting IR radiation	-
0	Point at earth's surface in field of view of point (P)	-
P	Position of satellite at distance (h) above point (S) on earth's surface	-
r	Radius of earth (6378 km)	(km)
rs	Subscript denoting reflected solar radiation	-
R_n	Net radiation at a standard level of 30 km above earth's surface	(cal/cm^2 min)
SW	Subscript referring to solar radiation	-
s	Subscript denoting sensor	-
S	Subsatellite point	-
T_B	Temperature of black sensor	(deg A.)
T_M	Temperature of mirror	(deg A.)
T_s	Temperature of sensor	(deg A.)

T_W	Temperature of white sensor	(deg A.)
W	Subscript referring to white sensor	-
W*	Difference in energy gain ($E_{W_{day}} - E_{W_{night}}$)	(cal sr/cm^2 min)

GREEK LETTERS

α_{LW}	Absorptivity of sensor to IR irradiance from earth	-
α_{sw}	Absorptivity of sensor to solar radiation	-
α_B'	Lumped absorptivity constant	-
α_W'	Lumped absorptivity constant	-
β'	Geometrical form factor relating (f) to (H')	(sr)
β	Geometrical form factor relating (f) to (H)	(sr)
ϵ_{LW}	Emissivity of sensor for IR radiation	-
θ_m	Half-angle subtended by earth viewed from (P)	(sr)
θ_m^*	Half-angle subtended by earth viewed from standard level (30km)	(sr)
λ	Spectral wavelength	(micron)
π	3.1416	(sr)
σ	Stefan's constant (8.132×10^{-11})	(cal/cm^2 °A min)
$\left.\begin{matrix}\psi \\ \theta\end{matrix}\right\}$	Directional coordinates (fig. A-1)	(sr)
ϕ	Solar zenith angle at point (P) or (S)	(sr)
ω	Solid angle	(sr)

1. INTRODUCTION

This paper is intended to provide the theoretical background for obtaining irradiance values from low-resolution radiometers of the TIROS satellite series. Hemispherical sensors were used on the TIROS series. The theory and notation used in this presentation were developed, in part, by Suomi (1958), Bignell (1962), and House (1965).

The theory for inflight calibration of the low-resolution radiometers is developed in this paper. Such a calibration is possible from data obtained when the satellite crosses the earth's shadow (usually called the terminator) and the earth shades or unshades the radiometers from the direct sunlight. These inflight calibrations provide information on degradation of the absorbing properties of the sensor surface. The measurements are useful in determining other sensor characteristics as well.

An important feature of this measurement system is that the radiant energy from a specific source which is absorbed by the sensor is used to determine the irradiance from that source, through a known geometrical relationship between the two. The radiation sources are direct solar radiation, reflected solar radiation from the earth, and IR radiation from earth.

A necessary refinement to the calculation of irradiance is to reduce the irradiance value, determined for the height of the satellite, to some lower (reference) level, which more nearly corresponds to the "top" of the atmosphere. Such a reduction assures the compatibility of all measurements obtained during an elliptical orbit, or from satellites in different orbits. This refinement is included here.

2. RADIANCE AND IRRADIANCE

In this section the radiance and irradiance terms will be derived as needed to develop the measurement theory. Although some of this development is repetitious of material published elsewhere, it is included here for continuity and completeness.

It is useful to consider the amount of radiant energy $dE(\lambda)$ in a specific wavelength interval $(\lambda, \lambda + d\lambda)$ which is transported across an element of area da and in directions confined to an element of solid angle $d\omega$ during a time dt, as shown in Figure 1, and as defined by Chandrasekhar (1960). This energy $dE(\lambda)$ is expressed in terms of the intensity $I(\omega, \lambda)$ by,

$$(1) \qquad dE(\lambda) = I(\omega, \lambda) \cos\theta \; da \; dt \; d\omega \; d\lambda$$

where θ is the angle which the direction considered makes with the outward normal to area da.

In order to sum the intensity over many solid angles, it is convenient to express the solid angle in polar coordinates, as shown in Figure 1, where

$$d\omega = \sin\theta \, d\theta \, d\psi \tag{2}$$

The amount of radiant energy in the spectral interval $d\lambda$ per unit area and unit time may then be expressed as,

$$dE(\lambda)/da\,dt = I(\theta, \psi, \lambda) \cos\theta \sin\theta \, d\theta \, d\psi \, d\lambda \tag{3}$$

The integrated form of Eq. (3) gives the spectral irradiance $H(\lambda)$, which is the total amount of radiant energy in spectral interval $d\lambda$ per unit area and unit time, from sources on the earth. This is written as

$$H'(\lambda) = \frac{E(\lambda)}{da\,dt} = \int_{\lambda}^{\lambda_2} \int_{\phi=0}^{2\pi} \int_{\theta=0}^{\theta_m} I(\theta, \psi, \lambda) \cos\theta \sin\theta \, d\theta \, d\psi \, d\lambda \tag{4}$$

Equation (4) is the basic radiative transfer equation by which irradiance is defined, as well as the total radiation impinging on a spherical satellite sensor, and is useful in specifying the total irradiance from the earth at any height above the "active" radiating layer of atmosphere.

a. Radiation at Satellite Height

We wish to consider the radiation reaching the satellite at a point P and distance h above the earth's surface, as shown in Figure 2. The radiation streams reaching this point above the earth are from three sources. These are:

i) direct solar radiation from the sun $(0 \leq \lambda \leq 4\mu)$,

ii) solar radiation reflected upward from the earth and atmosphere $(0 \leq \lambda \leq 4\mu)$, and,

iii) IR radiation from the earth and atmosphere $(4 \leq \lambda \leq \infty)$.

The first source, direct solar radiation, is parallel beam radiation I_s with units of cal/cm^2 min. The radiation from this source is very nearly constant at the satellite during one orbit (except for the period when the satellite is eclipsed by earth) because the semimajor axis of the satellite orbit is small compared to the earth-sun distance. The reflected solar and IR radiation from earth, sources ii) and iii), only differ in their spectral distribution of radiation. Fortunately, these two radiation streams have a natural separation in their spectra at a wavelength of about 4 microns. As a result, the radiance values for both reflected solar radiation and IR radiation in a direction CP and solid angle $d\omega$ are defined as

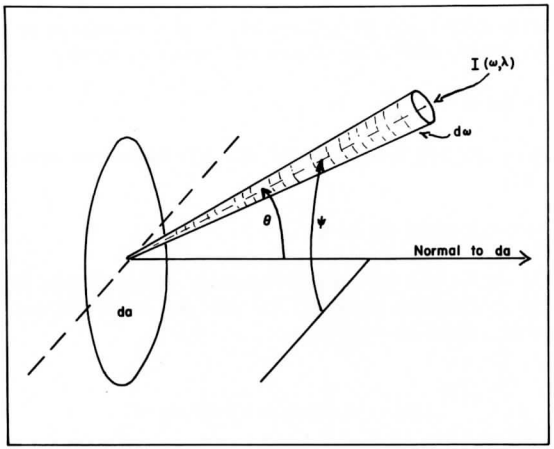

Fig. 1. Intensity $I(\omega, \lambda)$ on an area da.

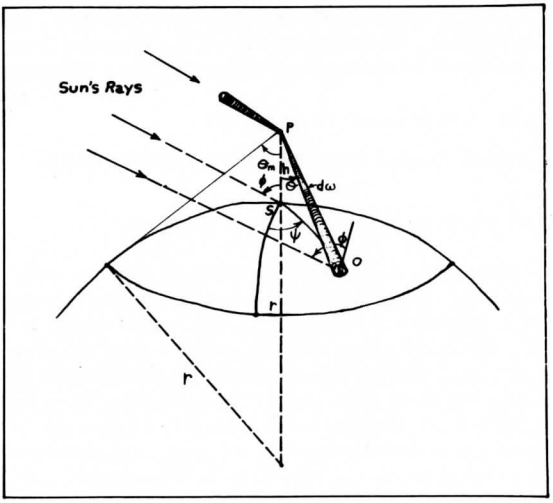

Fig. 2. Radiation reaching a satellite at point P above the earth.

$$I_{rs}(\theta,\psi) = \int_{\lambda=0}^{4\mu} I(\theta,\psi,\lambda)d\lambda$$

$$I_{LW}(\theta,\psi) = \int_{\lambda=4\mu}^{\infty} I(\theta,\psi,\lambda)d\lambda \qquad (5)$$

where the subscript rs refers to reflected solar radiation and LW refers to IR radiation from earth.

b. Irradiance

It is clear that if the spectral irradiance $H(\lambda)$, which is given in Eq. (4), is integrated over a fixed spectral interval, $\lambda_1 - \lambda_2$, the irradiance for that wavelength interval is obtained. Mathematically, this is seen by combining Eqs. (4) and (5) which gives,

$$H'_{rs} = \int_0^{2\pi}\int_0^{\theta_m} I_{rs}(\theta,\psi)\cos\theta\,\sin\theta\,d\theta\,d\psi$$

$$H'_{LW} = \int_0^{2\pi}\int_0^{\theta_m} I_{LW}(\theta,\psi)\cos\theta\,\sin\theta\,d\theta\,d\psi \qquad (6)$$

Again, the subscripts rs and LW refer to reflected solar and IR radiation from earth.

To facilitate the development of the measurement theory, we will use the general form of Eq. (6) as,

$$H' = \int_0^{2\pi}\int_0^{\theta_m} I(\theta,\psi)\cos\theta\,\sin\theta\,d\theta\,d\psi \qquad (7)$$

and in its use recall that it may be applied to irradiance of either reflected solar or IR radiation from earth. Thus, the irradiance H' is that at a point P above the earth's surface, as shown in Figure 2.

It is of interest to note in Eq. (7) that θ is integrated from zero to θ_m, for both reflected solar and IR radiation from earth. As a result, the irradiance of both reflected solar radiation and outward IR radiation at point P have the same geometrical considerations.

In general, reflected solar and IR radiation from earth will be anisotropic, mainly because of the scattering properties of cloud droplets, because of IR limb darkening, and because of the nonhomogeneity of the region in view. These effects have been treated by Bignell (1962) who showed that systematic errors due to anisotropy are small.

c. Radiance on an Isolated (Ideal) Spherical Sensor

The reflected solar and IR radiance from earth impinging on an isolated spherical sensor at point P may be defined as a special condition of Eq. (1) in which the radiance is intercepted by the cross-sectional area of the sphere, and is normal to this cross-sectional area. As a result, from Eq. (1) the amount of radiant energy $dE_S(\lambda)$ intercepted by an element of area da on the sensor and in directions confined to an element of solid angle $d\omega$ during a time dt is defined as

$$dE_s(\lambda) = I(\omega, \lambda) d\omega \, da \, dt \, d\lambda \tag{8}$$

This may be visualized in Figure 1, assuming θ is zero.

Again, by expressing solid angle $d\omega$ in polar coordinates, Eq. (8) may be written as

$$dE_s(\lambda)/dadt = I(\theta, \psi, \lambda) \sin\theta \, d\theta \, d\psi \, d\lambda \tag{9}$$

The spectral radiant power $f(\lambda)$ of the radiation on an isolated spherical sensor at point P above the earth, is simply the product of the cross-sectional area of the spherical sensor πa^2 and its spectral radiance $I(\theta, \psi, \lambda)$ integrated over all angles to the earth. This is written as

$$f(\lambda) = \pi a^2 \int_{\lambda_1}^{\lambda_2} \int_0^{2\pi} \int_0^{\theta_m} I(\theta, \psi, \lambda) \sin\theta \, d\theta \, d\psi \, d\lambda \tag{10}$$

Clearly, if the spectral radiance $I(\theta, \psi, \lambda)$ in Eq. (10) is integrated over a fixed spectral interval $(\lambda_1 - \lambda_2)$, the radiant power f is obtained. Mathematically, this is easily seen if we specify the spectral radiance as either reflected solar or IR radiation, as indicated in Eq. (5). In that case, Eq. (10) may be written as,

$$f_{rs} = \pi a^2 \int_0^{2\pi} \int_0^{\theta_m} I_{rs}(\theta, \psi) \sin\theta \, d\theta \, d\psi$$

$$f_{LW} = \pi a^2 \int_0^{2\pi} \int_0^{\theta_m} I_{LW}(\theta, \psi) \sin\theta \, d\theta \, d\psi \tag{11}$$

Here again, the subscripts rs and LW refer to reflected solar and IR radiation from earth. The general case of Eq. (11) for the radiant power from a specified source on a spherical sensor at point P is

$$f = \pi a^2 \int_0^{2\pi} \int_0^{\theta_m} I(\theta, \psi) \sin\theta \, d\theta \, d\psi \tag{12}$$

d. Irradiance Determined by Measurement

In the low resolution radiometer experiment, the reflected solar and IR irradiance values are not measured directly, but rather are calculated from measurements of the radiant power from these radiation sources on a spherical sensor. A computation of irradiance from radiant power only requires a knowledge of the geometrical relationship between the two, for that particular sensor. A geometrical relationship of this nature has rather diverse application in space and atmospheric science and therefore has various names. For purposes of this paper, it will be termed the "geometrical form factor" and denoted as β. Its units are steradians.

For a spherical sensor, the relationship between irradiance and radiant power is obtained by combining Eqs. (6) and (12). This gives

$$\frac{f}{H'} = \frac{\pi a^2 \int_0^{2\pi} \int_0^{\theta_m} I(\theta,\psi)\sin\theta \, d\theta \, d\psi}{\int_0^{2\pi} \int_0^{\theta_m} I(\theta,\psi)\sin\theta\cos\theta \, d\theta \, d\psi} \tag{13}$$

It is convenient to make the isotropic assumption for reflected solar and IR radiation from earth, so that Eq. (13) may be integrated. When this is done, we obtain

$$f = a^2 \left[2\pi \left(\frac{1 - \cos\theta_m}{\sin^2\theta_m} \right) \right] \cdot H' \tag{14}$$

From Eq. (14) it is easily seen that the term in brackets is the geometrical form factor β' which relates f and H'. That is,

$$\beta' = 2\pi \left(\frac{1 - \cos\theta_m}{\sin^2\theta_m} \right) \tag{15}$$

It is also clear from Eq. (15), that the geometrical form factor, β, at point P depends on the half-angle θ_m subtended by earth at point P. For example, as a satellite at point P approaches the earth's surface, the value of θ_m approaches 90 degrees, and from Eq. (15) it is apparent that β' approaches 2π steradians. This dependence of β' on θ_m is also shown in Figure 3.

Combining Eqs. (14) and (15) gives a final relationship between radiant power on a spherical sensor, geometrical form factor, and irradiance

$$f = a^2 \beta' H' \tag{16}$$

This is a very useful form for considering the radiation balance of a spherical sensor as a function of irradiance rather than radiant power.

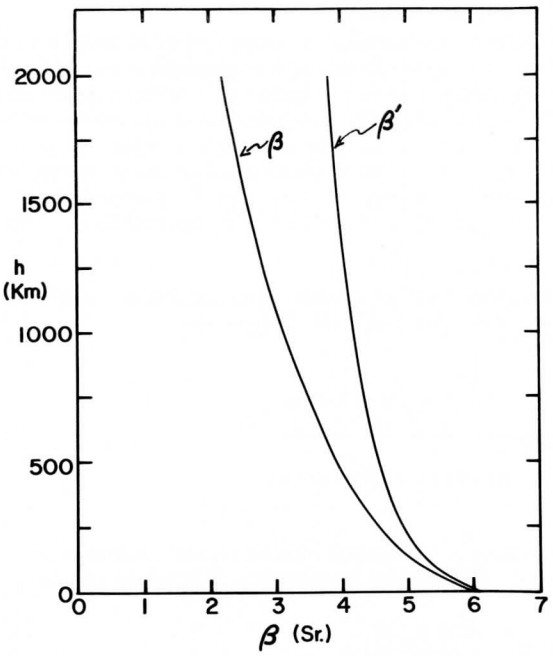

Fig. 3. Geometrical form factors, β and β', as a function of height.

3. RADIATION BALANCE OF AN ISOLATED (IDEAL) SPHERICAL SENSOR

The radiation balance of an isolated spherical sensor can be expressed by equating the sum of terms which represent gains of energy by the sensor with the sum of terms which represent losses of energy by the sensor. With this in mind, it is possible to write the radiation balance equation for an isolated (ideal) spherical sensor as,

$$(17) \quad (\alpha_{sw} \pi a^2 I_s) + (\alpha_{sw} f_{rs}) + (\alpha_{LW} f_{LW}) = 4\pi a^2 \epsilon_{LW} \sigma T_s^4$$

where α and ϵ are the respective absorptivity and emissivity; the subscripts SW and LW denote solar and IR radiation, respectively; and T_s is the sensor temperature in degrees A. With the aid of Eq. (16) we may rewrite (17) as

$$(18) \quad (\alpha_{SW} \pi I_s) + (\alpha_{SW} \beta' H'_{rs}) + (\alpha_{LW} \beta' H'_{LW}) = 4\pi \epsilon_{LW} \sigma T_s^4$$

This form of the radiation balance equation includes the irradiance H' terms for a point P above the earth.

However, a more practical form of the radiation balance equation is one which gives the irradiance value for a standard (reference) level above the earth, rather than for point P. House (1965) suggested a reference level of 30 km above the earth's surface; we will define the upward irradiance at this 30 km reference level as H. From integrating Eq. (7) for this level and assuming isotropic conditions, we obtain

$$H = \pi I \sin^2 \theta_m^* \tag{19}$$

where θ^* is the half-angle subtended by earth as viewed from the reference level. Furthermore, the relationship between upward irradiance H' as point P and upward irradiance H at the 30 km reference level is

$$\frac{H}{H'} = \frac{\sin^2 \theta_m^*}{\sin^2 \theta_m} \tag{20}$$

Combining (16) and (20) leads to the relationship between f and the upward irradiance H at the reference level

$$f = a^2 \beta H \tag{21}$$

where β is the geometrical form factor which relates f and H. β is defined as

$$\beta = \beta' \left(\frac{\sin^2 \theta_m}{\sin^2 \theta_m^*} \right) \tag{22}$$

or, written only as a function of θ_m,

$$\beta = \frac{2\pi (1 - \cos \theta_m)}{\sin^2 \theta_m^*} \tag{23}$$

Now if we assume the top of the radiating atmosphere is 30 km, which is the reference level, then θ_m^* is 90 degrees and Eq. (23) may be written simply

$$\beta = 2\pi (1 - \cos \theta_m) \tag{24}$$

The dependance of β on θ_m is also shown in Figure 3. This figure shows that β approaches 2π as θ_m approaches 90 degrees, as expected. With the geometrical form factor defined, it is possible, finally, to write a balance equation for an isolated sensor at a point P above the atmosphere in terms of irradiance values at the 30 km reference level.

$$(\alpha_{SW} \pi I_s) + (\alpha_{SW} \beta H_{rs}) + (\alpha_{LW} \beta H_{LW}) = 4\pi \epsilon_{LW} \sigma T_s^4 \tag{25}$$

This is the most useful for of the radiation balance equation for visualizing the energy balance of an actual satellite radiometer which, of course, departs from the idealized "perfect" spherical sensor that has been discussed so far.

A sometimes useful refinement of Eq. (25) is to express β and β' as functions of the height h of point P and the radius of the earth r, rather than as functions of the half-angle θ_m subtended by the earth. From geometry consideration of Figure 2

$$\sin \theta_m = \frac{r}{r+h}; \qquad \cos \theta_m = \sqrt{1 - \left(\frac{r}{r+h}\right)^2} \tag{26}$$

Using this relationship, β' and β in Eqs. (15) and (24) may be expressed as

$$\beta' = 2\pi\left(\frac{1 - \sqrt{1 - A^2}}{A^2}\right) \tag{27}$$

$$\beta = 2\pi\,(1 - \sqrt{1 - A^2}) \tag{28}$$

where, $A = r/(r+h)$.

4. ENERGY BALANCE OF HEMISPHERICAL SENSORS

a. Departure from Isolated (Ideal) Spherical Sensors

The hemispherical sensors which have been flown on the TIROS satellites differ from the isolated (ideal) spherical sensors described above in several ways.

i) They are not spherical.
ii) They are mounted on a spinning satellite.
iii) They are not thermally isolated from the satellite.
iv) They have "imperfect" spectral response characteristics.
v) The time constant of the sensors is greater than zero.

Although the sensors are hemispheres, they optically approximate a sphere since they are mounted on metal mirrors. When such a hemisphere-mirror combination is viewed at an oblique angle, it yields the image of a sphere composed partly of the hemispherical sensor and partly the sensor's reflected image on the mirror. The sensor's "reception" of incident radiation is analogous to its visual optics.

Of course, on a spinning satellite, one mirror-backed hemisphere will no longer represent a sphere to incident radiation when the satellite body eclipses the sensor's "view" of the radiation source. This problem is solved by the construction of a sensor "set" consisting of two identical mirror-backed hemispheres which are mounted diametrically opposed on the exterior surface of the satellite. In this case, as one sensor-mirror combination begins to be eclipsed by the satellite, its opposite twin begins to enter the field of view of the radiation source. In practice, the measured sensor temperature is an average of two temperatures from matched thermistors mounted in twin sensors and connected in series.

A more significant departure from the isolated spherical sensor is caused by the inability to thermally isolate the hemispheres from the body of the satellite. Energy exchange occurs between the sensor and the mirror by,

i) conduction along the hemispheres' supporting post, and
ii) radiation between the mirror and the sensor.

House (1965) has shown how the energy balance equation for an isolated spherical sensor must be modified to account for this gain or loss of energy.

In practice, the black-painted "black" sensor and the anodized aluminum "white" sensor have distinct spectral characteristics which differ in varying degrees from a "perfect" sensor set. Because of this, the energy balance equation which are used with actual measurements must include the proper radiant absorptance α and radiant emissivity ϵ values for both black and white sensors. These values are obtained before launch by laboratory experiments. However, primarily because of the unknown response of the surface coatings to the space environment, these values of α and ϵ are treated, whenever possible, as unknown quantities in the energy balance equations.

Further modification of the energy balance equation for an isolated spherical sensor is necessitated by the thermal mass of the temperature measuring system. This requires the inclusion of a "lag" term which may represent either a gain or loss of energy of the sensing system.

b. Energy Balance Equations for the Hemispherical Sensors

In view of the general comments above, the energy balance equation for a mirror-backed black hemisphere on a spinning satellite is necessarily a modification of the energy balance Eq. (25) for a "perfect" isolated, spherical sensor. A suitable modification is,

$$\frac{1}{2}(\alpha_{SW_B}\pi I_s) + \frac{1}{2}(\alpha_{SW_B}\beta H_{rs}) + \frac{1}{2}(\alpha_{LW_B}\beta H_{LW}) = 2\pi\epsilon_{LW_B}\sigma T_B^4 - K_{M_B}\sigma T^4 + K_{L_B}(T_B - T_M) + K_{L_B}\left(\frac{\partial T_B}{\partial t}\right) \quad (29)$$

The factor 1/2 which is applied to each irradiance term in the LHS of Eq. (29) results from the fact that each sensor absorbs radiation from solar and earth sources only half the time, owing to the rotation of the satellite. However, the radiation loss from the sensor is continuous—thus the factor of 1/2 is not included on the RHS of Eq. (29). Previously undefined symbols in Eq. (29) are: T_m, the temperature of the mirror; K_{M_B}, K_{C_B}, and K_{L_B}, which are "lumped" constants that are determined either in laboratory or by inflight techniques For the present, we shall define them as:

K_{M_B} - a lumped constant which includes the geometry and the radiant emissivity of the mirror,

K_{C_B} - a lumped constant which includes the thermal conductivities and dimensions of the post, and

K_{L_B} - a lumped constant which includes the heat capacity of the black sensor.

Applying a multiplying factor, $2/\alpha_{LW_B}$, to Eq. (29), we have,

$$(30) \quad (\alpha_B' \pi I_s) + (\alpha_B' \beta H_{rs}) + (\beta H_{LW}) = 4\pi\left(\frac{\epsilon_{LW_B}}{\alpha_{LW_B}}\right) \sigma T_B^4 - C_{M_B} \sigma T_M^4 + C_{C_B}(T_B - T_M) + C_{L_B}\left(\frac{\partial T_B}{\partial t}\right)$$

where,

$$(31) \quad \alpha_B' = \alpha_{SW_B}/\alpha_{LW_B}$$

$$C_{M_B} = 2K_{M_B}/\alpha_{LW_B}$$

$$C_{C_B} = 2K_{C_B}/\alpha_{LW_B}$$

$$C_{L_B} = 2K_{L_B}/\alpha_{LW_B}$$

The advantage in using Eq. (30) is, of course, that one constant has been eliminated. However, the elimination makes "lumped" constants of those remaining, as shown by the Eqs. (31).

All of the discussion above relative to a <u>black</u> hemispherical sensor also applies to a <u>mirror-backed white hemisphere.</u> Using the same arguments, it can be shown that for a <u>white</u> hemispherical sensor

$$(32) \quad (\alpha_W' \pi I_s) + (\alpha_W' \beta H_{rs}) + (\beta H_{LW}) = 4\pi\left(\frac{\epsilon_{LW_N}}{\alpha_{LW_N}}\right) \sigma T_W^4 - C_{H_W} \sigma T_M^4 + C_{C_W}(T_W - T_M) + C_{LW}\left(\frac{\partial T_W}{\partial t}\right)$$

where

$$\alpha'_W = \alpha_{SW_W} / \alpha_{LW_W}$$

$$C_{M_W} = 2K_{H_W} / \alpha_{LW_W}$$

$$C_{C_W} = 2K_{C_W} / \alpha_{LW_W} \qquad (33)$$

$$C_{LW} = 2K_{LW} / \alpha_{LW_W}$$

5. THE IRRADIANCE CALCULATION

The energy balance equations illustrate the basic principles of a set of black and white omnidirectional radiation sensors. They also provide a means of describing the energy gains and losses to which each sensor set responds. We will now discuss the use of a pair of these equations (one black sensor and one white sensor) to compute the irradiance terms.

We will consider the energy balance Eqs. (30) and (32). The RHS of both these equations is made up of terms which contain "lumped" constants and the measured temperatures of the sensor and its mount. All of these terms can therefore be evaluated if the constants are known. In general, it is possible to determine the conduction and lag constants (31) and (33) to sufficient accuracy either by laboratory or inflight techniques. The emissivity to absorptivity ratio in (30) and (32) is assumed to be unity. As a result, in the development that follows, the constants on the RHS of (30) and (32) are assumed known to sufficient accuracy for the measurements.

To simplify the notation we will represent the entire RHS of Eq. (30) by E_B and of Eq. (32) by E_W. These equations can be written then as

$$(\alpha'_B \pi I_s) + (\alpha'_B \beta H_{rs}) + (\beta H_{LW}) = E_B \qquad (34)$$

$$(\alpha'_W \pi I_s) + (\alpha'_W \beta H_{rs}) + (\beta H_{LW}) = E_W \qquad (35)$$

a. Night-time Calculations

The night-time energy balance equation is simplified considerably, of course, because the direct and reflected solar irradiance terms are zero. In this case, we can obtain directly the long wave irradiance from either the black or white hemisphere. Using Eq. (34) we have

(36) $$H_{LW} = E_B/\beta$$

b. Daytime Calculation

When the satellite is over the solar illuminated portion of the earth, each sensor is exposed to three types of irradiance. Since we have only two balance equations, we must eliminate one of these three unknowns. The direct solar irradiance term is the logical choice since it is nearly constant. However, in order to eliminate it as an unknown, we must determine its effect as "seen" by the black and white sensor combination. This is one part of the so-called "inflight calibration" or "solar contamination" technique.

Each time the satellite-borne sensors cross the terminator, at some point the sensors are directly above the darkened portion of the earth, but still illuminated by direct solar irradiance. At such a time, the reflected solar irradiance term is zero; thus, subtracting Eq. (35) from (34) we have,

(37) $$D^* = (E_B^* - E_W^*) = \pi I_s(\alpha_B' - \alpha_W')$$

The asterisk indicates data obtained at the terminator. These terms are also illustrated in Figure 4, which shows the energy gain of the black and white sensors as the satellite crosses the terminator.

As shown in that illustration, when the satellite passes through the terminator, there is an increase in energy gain by both the black and white sensors—the black has a considerably larger increase. The D* value in Eq. (37) is a measure of the difference between the energy being recieved by these two sensors. In effect, it is the "solar constant" as "seen" by the sensors. If there is no degradation of the sensors, the value of D* will be constant with time, for a series of terminator crossings. Likewise, a change in D* with time is a measure of sensor degradation. For this reason, a time plot of the value of D* is essential for the actual computations of irradiance and albedo values.

In passing through the terminator, there is a small increase in the energy gain of the white sensor, because it is not a perfect reflector. This may be referred to as "solar contamination" of the white sensor W*. This term is determined from the change in E_W values across the terminator. That is, Eq. (35) written for both the day and night side of the terminator defines $E_{W_{day}}$ and $E_{W_{nite}}$, respectively. The difference between these values defines the direct solar contamination of the white sensor W*.

(38) $$W^* = (E_{W_{day}} - E_{W_{nite}}) = \pi I_s(\alpha'_W)$$

1. Albedo Determination—The albedo can be determined during any portion of the orbit in which the satellite is in the sun, by using the black and white sensor measurements in combination. Subtracting Eqs. (34) from (35) for some point during orbit gives,

$$E_B - E_W = \pi I_s (\alpha'_B - \alpha'_W) + \beta H_{rs} (\alpha'_B - \alpha'_W) \tag{39}$$

We see that Eq. (39) includes three unknowns, the direct solar and reflected solar irradiance terms, and the difference in lumped absorptivities. However, the first term on the RHS of Eq. (39) is easily determined from data at the terminator. This term is merely D* in Eq. (37), and therefore, can be routinely determined. Combining Eqs. (37) and (39), and solving for H_{rs} gives,

$$H_{rs} = (E_B - E_W - D^*)/\beta (\alpha'_B - \alpha'_W) \tag{40}$$

Since the solar constant is known to a better degree of accuracy than the difference in absorptivities, it is desirable to determine H_{rs} as a function of I_s rather than $(\alpha'_B - \alpha'_W)$. From Eq. (37), we have,

$$(\alpha'_B - \alpha'_W) = D^*/\pi I_s \tag{41}$$

As a result, Eq. (40) may be written as simply,

$$H_{rs} = I_s (\frac{\pi}{\beta}) \left(\frac{E_B - E_W}{D^*} - 1 \right) \tag{42}$$

The reflected solar irradiance cannot be determined from the measurements alone. As seen in Eqs. (40) and (42), there is one remaining unknown, which can be either I_s of $(\alpha'_B - \alpha'_W)$, depending on which equation is desired in order to express H_{rs}.

Fortunately, it is not necessary to determine H_{rs} directly, since we are interested in determining the albedo ALB. This is simply obtained by multiplying (42) by the factor $(1/I_s \cos\phi)$; where ϕ is the solar zenith angle at the subsatellite point. This gives the albedo as,

$$ALB = \frac{1}{\cos\phi} (\frac{\pi}{\beta}) \left(\frac{E_B - E_W}{D^*} - 1 \right) \tag{43}$$

A useful refinement to Eq. (43) is to determine an integrated cosine function $\cos^*\phi$ for a solar zenith angle of the area "seen" by the satellite, rather than the cosine function $\cos\phi$ for a solar zenith angle only at the subsatellite point. House (1965) has evaluated $\cos^*\phi$ for TIROS IV measurements from 0 - 90 degrees latitude. The results shown in Figure 5 indicate that the difference between $\cos\phi$ and $\cos^*\phi$ is a few percent when ϕ is small, but is progressively larger with increasing values of ϕ. Thus, the proper function form for Eq. (43) is to use $\cos^*\phi$ rather than $\cos\phi$ in the denominator.

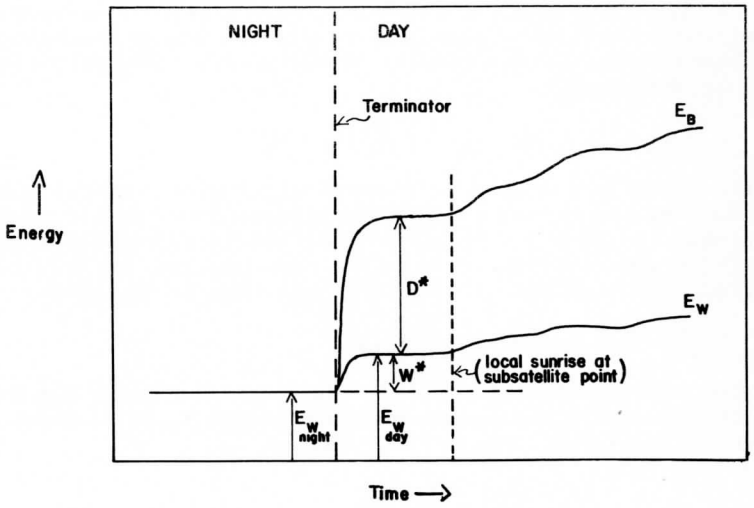

Fig. 4. Energy gain by the black and white sensors when the satellite passes through the terminator.

Fig. 5 (below). Dependence of $\cos^* \phi$ on the zenith angle of the sun at the subsatellite point.

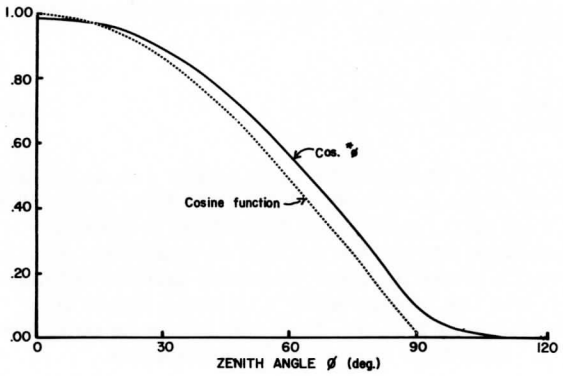

2. Outward IR Irradiance Determination—The Outward IR irradiance from earth is also determined by combining the black and white sensor data. Equation (35) gave the total radiation gain of the white sensor any time during the orbit. This equation is

$$(\alpha'_W \pi I_s) + (\alpha'_W \beta H_{rs}) + (\beta H_{LW}) = E_W$$

and includes the radiation terms I_S and H_{rs} as well as the irradiance H_{LW} that we wish to determine. However, the I_S term is simply the solar contamination of the white sensor W*, and the H_{rs} term may be determined from Eq. (40). As a result, it is possible to combine Eqs. (35), (38) and (40) to give

$$W^* + \frac{\alpha'_W(E_B - E_W - D^*)}{(\alpha'_B - \alpha'_W)} + \beta H_{LW} = E_W \qquad (44)$$

But from Eqs. (37) and (38),

$$W^*/D^* = \alpha'_W/(\alpha'_B - \alpha'_W)$$

which is simply the ratio of the solar contamination of the white sensor to the difference in solar contamination of the sensor pair. This ratio is very useful because it makes it possible to determine the solar contamination of the white sensor due to direct solar and reflected solar radiation together, for measurements at any point along the orbit. As a result, we will define this important ratio as R*. That is

$$R^* = W^*/D^* = \frac{\alpha'_W}{(\alpha'_B - \alpha'_W)} \qquad (45)$$

Now using (45), we may write Eq. (44) as

$$R^*(E_B - E_W) + \beta H_{LW} = E_W \qquad (46)$$

This may be solved for H_{LW} as

$$H_{LW} = [E_W - R^*(E_B - E_W)]/\beta \qquad (47)$$

The physical interpretation of Eq. (47) is that E_W is the total radiation gain from all sources. Therefore, to determine the IR irradiance, it is only necessary to subtract the solar contamination from E_W —leaving only the IR irradiance. The solar contamination that we wish to subtract from E_W is simply $R^*(E_B - E_W)$, since R* is the solar contamination of the white sensor relative to the difference in contamination of the sensor pair.

REFERENCES

Bignall, K., 1962, "Heat-balance Measurements from an Earth Satellite: An Analysis of Some Possibilities," Royal Meteor. Soc., p. 231-244.

House, F., 1965, "The Radiation Balance of the Earth from a Satellite," unpublished Ph. D. Thesis, University of Wisconsin.

Suomi, V., 1958, "The Radiation Balance of the Earth from a Satellite," Annals of the IGY, VI, p. 331-340.

THE "CHIRP" DIGITAL RADIOSONDE[1]

by

Verner E. Suomi, Kirby J. Hanson and Robert J. Parent

[1] Published: Journal of Applied Meteorology, 1967, 6:1, pp. 195-198.

ABSTRACT

This paper reports on a digital measurement ("chirp") system which has application for a wide range of meteorological and earth satellite measurements.

The system employs a simple concept in which a voltage pulse, proportional to a sensor voltage, is used to generate a burst of pulses from a voltage controlled oscillator (VCO). A count of the high frequency oscillations which make up the "chirp" provides the digital measurement. The system is adapted to multiple sensor use with a multiplexer.

The system has the advantage in that one has the option of selecting an ac amplifier for low level signals in conjunction with a variety of multiplexers and VCO for the desired measurement. One particular combination of multiplexer and VCO was used to demonstrate its use as a digital radiosonde.

A flight test of the digital radiosonde was obtained. Results clearly show fine structural detail in the temperature profile without any need for subjective interpretation by the operator. Numerous isothermal and inversion layers less than 100 m in thickness were observed.

The digital radiosonde used conventional (U. S. Weather Bureau) temperature and humidity sensors. Temperature resolution is about 0.1C and relative humidity is about 0.1 percent. The system resolution is 0.1 percent.

1. INTRODUCTION

A digital measurement ("chirp") system has been developed which has possible application for atmospheric studies from satellite, rocket or balloon carriers, or fixed station use in remote areas or on oceanic buoys. The system has been test flown as a digital radiosonde. This paper discusses the concept of the system and reports on its use for a digital radiosonde.

2. THE SYSTEM

The "chirp" system is based on the simple combination of two concepts. If a sensor voltage is used to develop a sequence of pulses of similar shapes, fixed duration, but variable height, the area under each pulse curve is proportional to sensor voltage. Furthermore, this relationship holds for many pulse shapes; for example, the shape one gets in a simple capacitor-resistor differentiating circuit. Second, if the pulse is applied to a voltage controlled oscillator (VCO), the area under the pulse curve can be measured simply by counting the total number of oscillations. Combining these two ideas, it is apparent that such a measurement would be proportional to sensor voltage. Small voltages can be used on the sensor because the pulse wave form is easily preserved with ac amplification; a more expensive dc amplifier is not required.

The system is "open loop" which requires a reference resistor in order to obtain absolute values. In this respect it is similar to the conventional radiosonde.

It should be emphasized that many other multiplexing schemes are possible, particularly when a larger number of sensors or low power consumption is desired. There are also many options available in selecting the VCO.

There is considerable flexibility in recording. Only a simple counter is required for measurement, and its output can be recorded by printing, punching or on magnetic tape. These devices are available commercially. Direct computor input is also possible.

3. DIGITAL RADIOSONDE EXAMPLE

The particular multiplexer and VCO discussed in this paper were selected merely to demonstrate the "chirp" system as a digital radiosonde. The multiplexer (Fig. 1) is a modification of that developed by Kobussen and Weinman (1966) for use in radiosonde switching. The voltage controlled blocking oscillator is that developed by Unter (1965).

The sampling rate of the digital radiosonde is four measurements per second chosen to fit the Hewlett-Packard counter and printer. During a typical (90 min) balloon sounding, each sensor would provide about 5000 measurements.

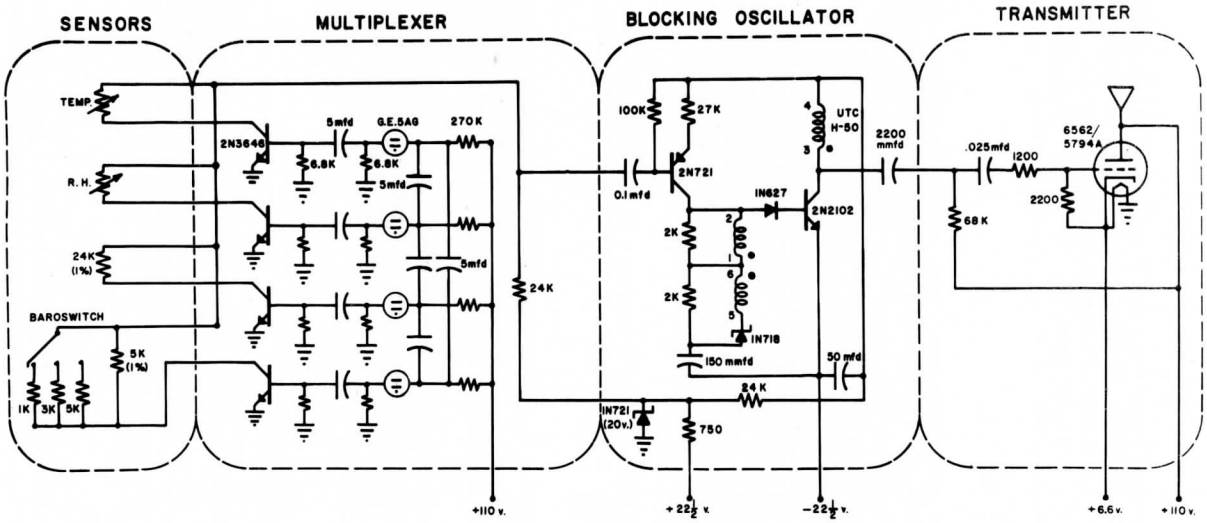

Fig. 1. Circuit for the "chirp" digital radiosonde that was flight-tested at Madison, Wisconsin, on 8 November 1965.

The system resolution is better than 0.1 percent. The temperature resolution is about 0.1C and relative humidity is about 0.1 percent.

Because the pulse sampling time is short, it is possible to apply high voltages to sensors without overheating. For example 20V was applied to the thermistor and only 50 μW of power was dissipated in the sensor.

4. TEST FLIGHT AND RESULTS

A flight test of the digital radiosonde was made (1500 CST, 8 November 1965) using a balloon sounding from Madison, Wisc. The results are illustrated in Figs. 2 and 3 together with a sounding made at Green Bay, Wisc., three hours later. The Green Bay sounding is that obtained by the U.S. Weather Bureau using a standard (or conventional) radiosonde. The similarity of the temperatures at heights above 675 mb (Fig. 2) is quite apparent. The departure of the two soundings below 675 mb can be expected considering space and time differences and the weather situation at that time.

A great deal of structural detail can be seen in the inversion layer, shown in Fig. 3. The main meteorological interest is the fact that the steep slope of the temperature inversion is limited to a shallow (11 mb) layer just above the cloud top. A second shallow inversion layer, 7 mb thick, is found near 700 mb. Both of these layers are only about 100 m in thickness.

The three layers marked "A," "B" and "C" are shallow isothermal layers; through each of these layers, the count value from the temperature sensor did not vary. Such repeatability inflight provides an indication of the low noise level and high reproducibility that can be obtained with this system.

A sample of the paper tape record obtained during a portion of the test flight of the digital radiosonde is shown in Figure 4. Data was received sequentially from the sensors beginning with temperature. Time proceeds upward on the record. Temperature, humidity and reference resistors were sampled on each sequence of four measurements (i.e., once each second). The baroswitch was also sampled on each sequence and had one of four fixed resistance values, depending on the position of the baroswitch arm (see Fig. 1). In this way a change between the fixed resistance values indicated a change in the baroswitch position, which in turn provides the pressure measurement. A similar method is used in the conventional radiosonde. For routine use, a continuously varying pressure sensor would improve resolution a great deal.

A direct comparison between the soundings cannot be made because of space and time differences. The standard radiosonde has analog output and provides much more detail than is illustrated in Figs. 2 and 3. However, much of this find structural detail is lost in the routine scaling of "significant"

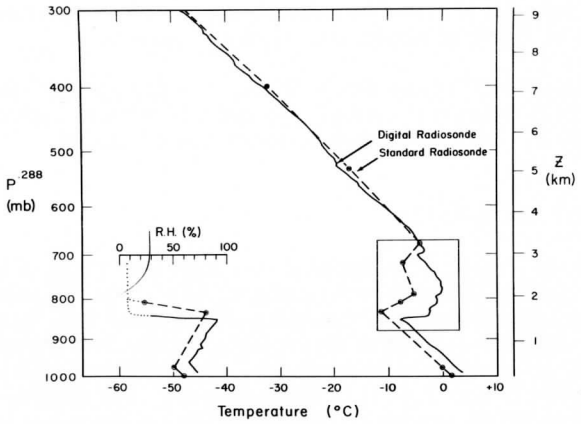

Fig. 2. Radiosonde observations of 8 November 1965, from (1) "chirp" digital radiosonde at Madison, Wisc., 1500 CST and (2) standard radiosonde at Green Bay, Wisc., 1800 CST.

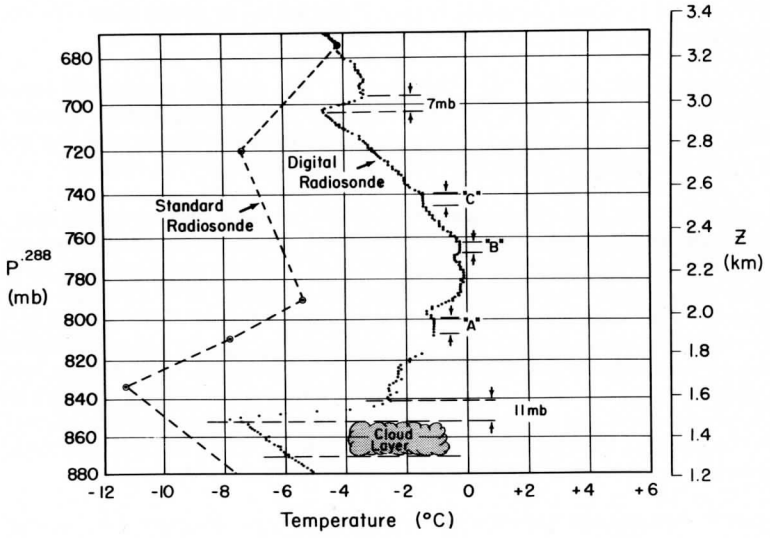

Fig. 3. Expanded scale illustration of the inversion layer shown in Fig. 2.

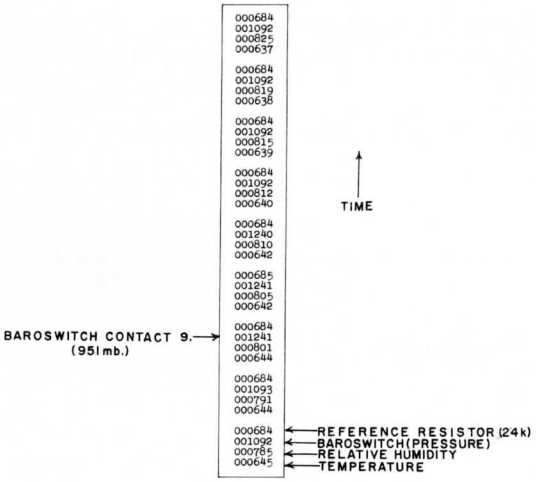

Fig. 4. Sample of paper tape record of the "chirp" digital radiosonde during the test flight on 8 November 1965.

levels from the analog records. All of the "significant" levels have been included in Figs. 2 and 3, however. The same types of sensors were used for both soundings.

5. DIGITAL RADIOSONDE CHARACTERISTICS

A standard U. S. Weather Bureau rod-type thermistor was used for temperature measurement with the digital radiosonde. The count as a function of temperature for that particular sensor is shown in Figure 5. The count-temperature relationship is nearly linear over a large portion of the temperature range. The sensitivity is greater than 10 counts $(°C)^{-1}$ from +10 to -35C. Above and below this range the sensitivity is less.

For humidity measurement, a lithium chloride strip-type sensor was used. The count as a function of relative humidity (for three constant temperatures) is shown in Figure 6. These curves shown that the maximum sensitivity is about (20 counts per unit percentage change); however, the sensitivity is greater than (10 counts per unit percentage change) over nearly the entire humidity range.

ACKNOWLEDGMENTS

The authors express their appreciation to Dr. Douglas Sargaent for helpful discussion during the course of this work, and to Mr. Harry Miller, Mr. David

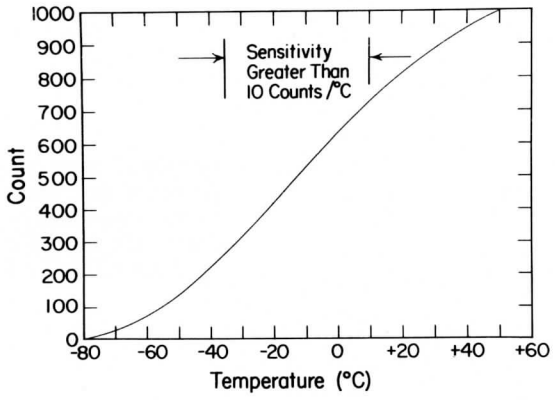

Fig. 5. Temperature measurement sensitivity of the "chirp" digital radiosonde.

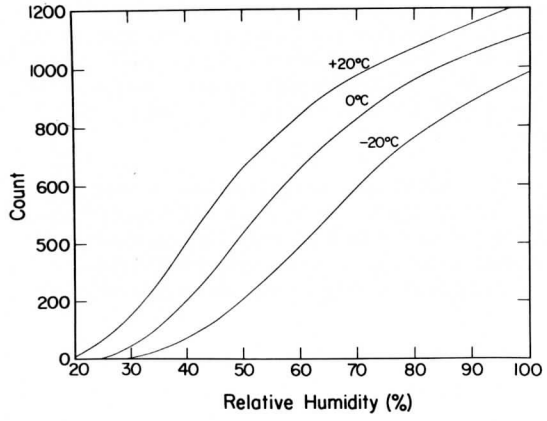

Fig. 6. Relative humidity sensitivity of the "chirp" digital radiosonde.

Nelson, and others of the Electrical Standards and Instrumentation Laboratory, University of Wisconsin, for their assistance during the instrument development.

This development was supported by ESSA under WBG-27.

REFERENCES

Kobussen, R., and J. Weinman, 1967: An economical multiplexer for use on radiosondes, J. Appl. Meteor., 6.

Unter, B., 1965: A unique low-level analog to digital converter. MS thesis, University of Wisconsin.

THE PROTOTYPE DATA LOGGING SYSTEM FOR THE ESSA III FLAT-PLATE RADIOMETERS

by

DAVID F. NELSON

GENERAL DESCRIPTION

This document is a brief description of the University of Wisconsin Type A data logging system as modified for the TOS spacecraft IR subsystem. The type A data logging system is designed to provide four functions: (1) digitize the resistance of external sensing elements such as thermistors; (2) provide sensor commutation so that several sensing elements can be measured in sequence; (3) store the digital data on magnetic tape; and (4) play back the stored data on external command.

The system is designed to require a minimum of power and to operate over a temperature range of -20°C to +60°C. It is packaged to survive environmental tests specified for the TOS spacecraft. The operation of the system will be discussed with reference to the block diagram Figure 1.

THE RECORDER

The recorder package is the heart of the system providing the functions of data storage, sensor commutation and counter input and readout switching. The recorder is packaged in a sealed container to prevent exposure of the mechanical system to the space environment. An outline drawing of the recorder appears in Figure 2.

The recorder is the incremental type, i.e., the tape moves in steps during the recording process rather than continuously. The drive system moves the tape 3.3 mils for every step with each step corresponding to one recorded bit. This results in a packing density of 300 bits/inch of tape. The drive is provided by a 2 phase step motor which is energized for 30 ms during each step. No power is applied to this motor except during a step. The recorder mechanism is held by a mechanical detent between steps. If the tapeup reel fills, the stepper power is removed.

During playback the tape is moved at a constant speed in the opposite direction from the record mode driven by a DC motor.

The step motor and DC motor are connected to the recorder capstan through a clutch which disengages the step motor and engages the DC motor during data playback. When the tape is returned to the beginning, the system reverts back to record mode. The recorder contains enough tape to record a minimum of 90,000 bits.

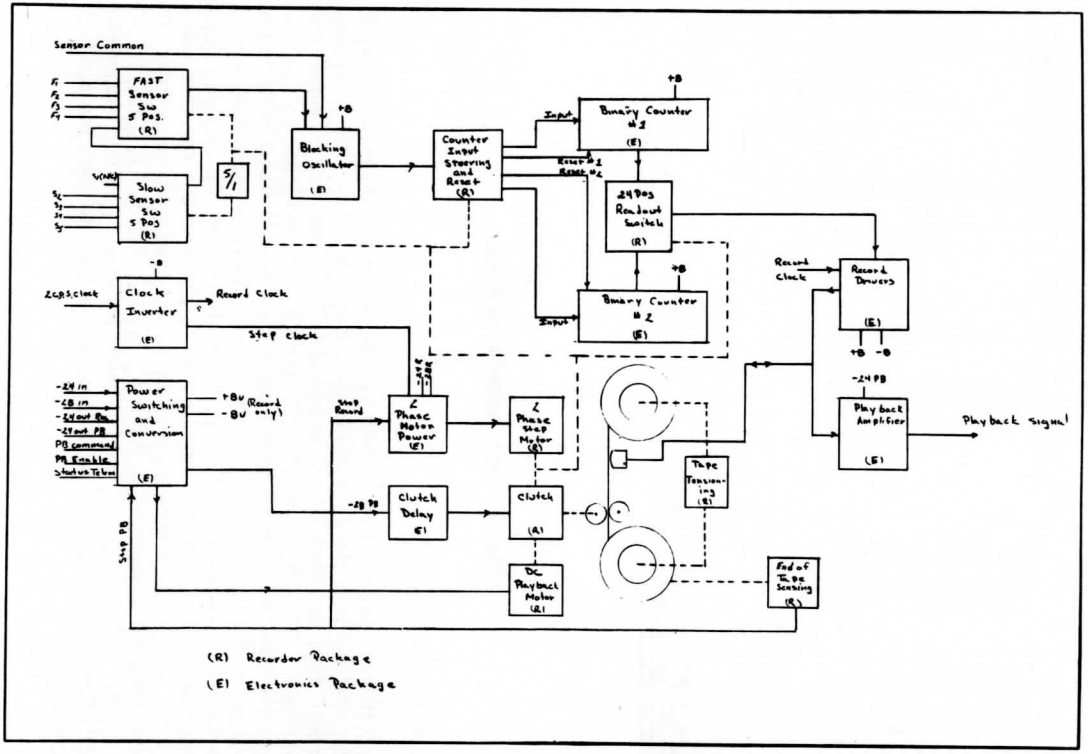

Fig. 1. The Radiometer Data Logging System

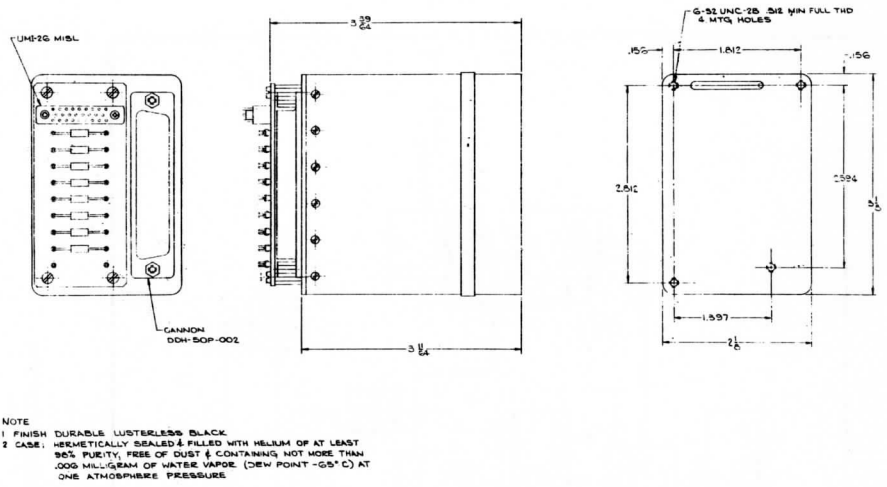

NOTE
1 FINISH: DURABLE, LUSTERLESS BLACK.
2 CASE: HERMETICALLY SEALED & FILLED WITH HELIUM OF AT LEAST 98% PURITY, FREE OF DUST & CONTAINING NOT MORE THAN .000 MILLIGRAM OF WATER VAPOR. (DEW POINT -65° C) AT ONE ATMOSPHERE PRESSURE

Fig. 2. The Recorder Package

SENSOR SWITCHING SYSTEM

The incremental nature of the record system makes it convenient to drive the switch systems from the same motor that drives the tape. All switching in the system is done by rotary switch assemblies designed around magnetically activated reeds. The sensor switching is provided by two 5 position switches. The sensor switches are interconnected mechanically and electrically to provide 4 primary or fast sensor positions and 5 secondary or slow positions. The fast sensors are designated F_1, F_2, F_3, F_4 and the slow S_1, S_2, S_3, S_4, S_5. Each sensor position is sampled for 10 out of 12 steps of the recorder with the change to the new position taking place during the remaining two steps. The sensor positions are sequenced as follows: S_1, F_1, F_2, F_3, F_4, S_2, F_1, F_2, F_3, F_4, S_3, F_1, F_2, F_3, F_4, S_4, etc. Sensor Position S_1 is left unconnected to provide a "zero" character every 25 sensor positions to mark the start of the sequence.

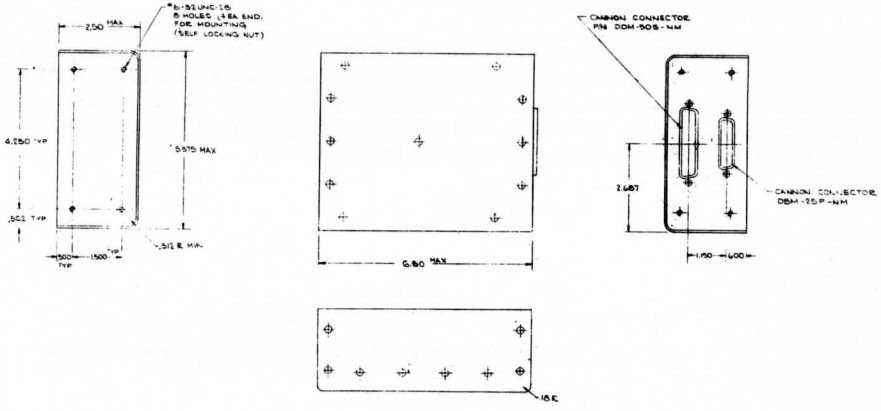

Fig. 3. The Electronics Package

COUNTER SWITCHING

Two additional reed switch assemblies are included in the recorder. One of these is a 24 position switch used for counter readout. This switch connects each stage of the counters to the record electronics in sequence thus determining the bit sequence on the tape. The other connects the output pulses of the resistance to frequency converter (blocking oscillator) to the counter which is not being read onto the tape and resets the counters after readout.

THE ELECTRONICS

The electronics package provides the following functions: (1) resistance to digital conversion; (2) record logic and head drivers; (3) playback amplifier; (4) power conversion; (5) power switching. An outline drawing of the electronics package appears in Figure 3.

RESISTANCE TO DIGITAL CONVERSION

The resistance to digital conversion is accomplished by generation of a frequency which is a function of the external sensor resistance and then counting this frequency in a binary counter for a fixed time interval. The resistance to frequency conversion is done with a temperature compensated blocking oscillator whose frequency is given by the relationship

$$f_c = \frac{K}{R_s + 20K}$$

where:

R_s = external sensor resistance K ohms,

K = a constant (1.7×10^6 typical value), and

f = is in cycles per second.

The output from the blocking oscillator is applied to the input of one of two 10 stage binary counters. One counter is read out while the other fills. The counter being filled counts the output pulses from the blocking oscillator for 10 steps of the recorder drive. The encoded number N for a sensor resistance R_s is then $N = (10/f_c)\left(K\frac{1}{R_s + 20K}\right)$ where f_c is the clock frequency supplied to the system. This clock frequency is 2 cps in the TOS system.

Sensor position S_2 is connected to a fixed precision resistor thus supplying a reference so that corrections can be made to compensate for drift in the value of K of f_c. Over a temperature range of -20°C to +60°C the drift in K is less than 1%.

RECORD SYSTEM

A 12 bit word is recorded on the tape for each measurement. The first ten bits are the binary data followed by a parity bit and a market bit. Two NRZ data tracks are recorded on the tape, designated the 1's track and 0's track. A flux transition occurs in the 1's track for each data "1" recorded and in the 0's track for a data zero. At the end of the readout of the 10 data bits a parity bit is recorded making the total number of 1's in the word even. In the twelfth bit position no change in head current is made in either track marking the end of a word.

The change in head current direction corresponding to a given bit occurs while between the steps of the recorder. The head current is continuous in one direction or another thus erasing all previous data during the recording of new data.

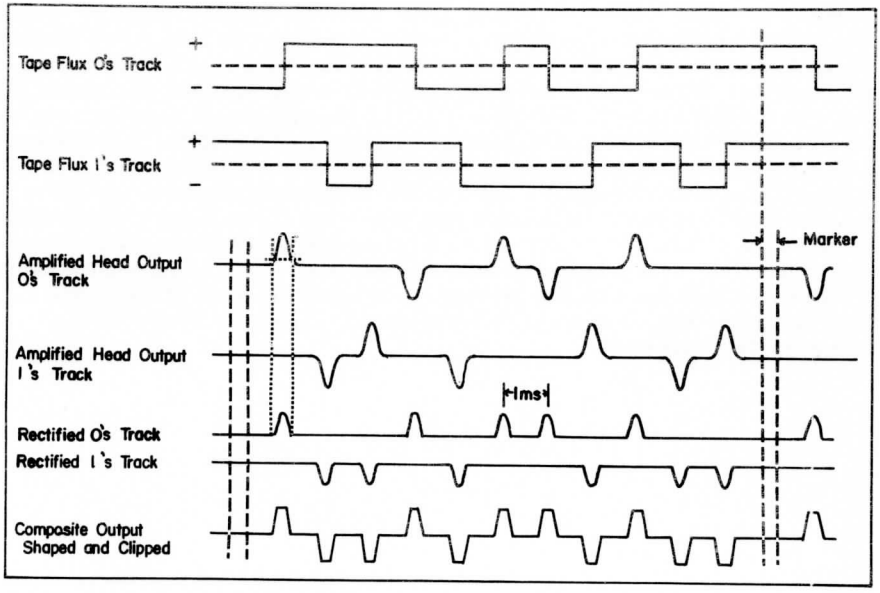

Fig. 4. Waveforms of the Playback System

PLAYBACK SYSTEM

In the playback mode the flux direction transitions on the tape produce positive and negative pulses on the terminals of the two playback heads. The playback electronics amplifies these signals separately and rectifies them so that the 1's track amplifier produces only negative pulses and the 0's track amplifier only positive pulses. These pulses are added and clipped to produce the output signal. The base level of the output is -2.5 V with 0's going to -5V. and 1's to 0v.

A summary of the playback system wave forms appears in Figure 4. The playback bit rate is 1000 bits/sec. $\pm$ 5%. The bit order on playback is reversed from the record sequence with parity first followed by the 512 bit, the 256 bit, etc.

POWER CONVERSION AND SWITCHING

A power switching relay is provided to remove power from the stepper drive and record mode circuits and apply power to the playback motor, clutch and

playback amplifier. There are two inputs to this relay system, playback enable and playback command. The playback enable input must be held at -24 V before the application of the playback command and must remain at -24 volts during the playback. If this enable voltage is removed during playback the system will revert to the record mode. A delay of 1 to 1.5 seconds occurs between switching to the playback mode and application of power to the clutch. This delay allows time for the playback amplifier and playback motor speed to stabilize.
A DC/DC converter provides $\pm$ 8 volts to the record mode circuitry. Power to the converter is removed during data playback. Two power outputs are provided for operation of auxiliary equipment such as the playback subcarrier oscillator. One of these is -24.5 V in record mode and the other -24.5 V in playback mode. A status telemetry point is also provided to indicate the state of the system. The voltages at this point are (1) 0 V-system off, (2) -1.5 V Record mode, (3) -3.5 V Playback mode.

THE PROTOTYPE FLAT-PLATE RADIOMETERS FOR THE ESSA III SATELLITE

by

David F. Nelson and Robert Parent

CONTENTS

1.0 INTRODUCTION

This document describes the wide angle infrared radiometer system developed by the University of Wisconsin as adapted for flight on the TIROS Operational Satellite (TOS). Descriptions of the sensor array, on board data system, data format and ground data handling are included. The design of the sensors and adaptation of an existing data system was carried out under contract to the Environmental Science Services Administration.

2.0 SENSOR ARRAY

2.1 Description

The sensor array has been designed to provide a measurement of the global distribution of the reflected solar and long wave radiation leaving the earth. The reflected solar and long wave radiation occupy two separate spectral regions with very little overlap. About 50 percent of the reflected solar lies primarily in the visible region of the spectrum and 98 percent of the energy at wavelengths below 3 microns. The long wave radiation roughly approximates black body radiation from a source at the temperature of earth. Assuming a temperature of 300°K, 94 percent of the long wave radiation is above 3 microns.

The sensor array is comprised of sensors of two configurations. These are: (1) a flat plate radiometer, with no attempt to restrict the field of view, and (2) a flat plate radiometer with cone optics to reduce or eliminate sensor response to direct solar radiation.

2.2 The Flat-Plate Radiometer

The sensing element of the flat-plate radiometer is an aluminum disc coated with either a black or white surface coating. The disc is thermally isolated from its mounts to minimize radiation and conductive coupling. The construction of the basic radiometer is illustrated in Figure 1.

The aluminum disc is suspended on dacron threads to provide a mechanical support and high thermal resistance to the mount. The back side of the disc including all epoxy (used for mounting) and the thermistor beads, is vacuum coated with aluminum to produce a low emissivity surface.

The exposed aluminum surfaces on the inside of the mount are polished to reduce radiative transfer of heat to the sensor. Two mylar radiation baffles from the back surface of the mount. These are coated with aluminum and gold, as indicated in Figure 1, to provide a reflective surface with low emissivity. Two thermistors mounted to the back surface of the disc provide the means by which

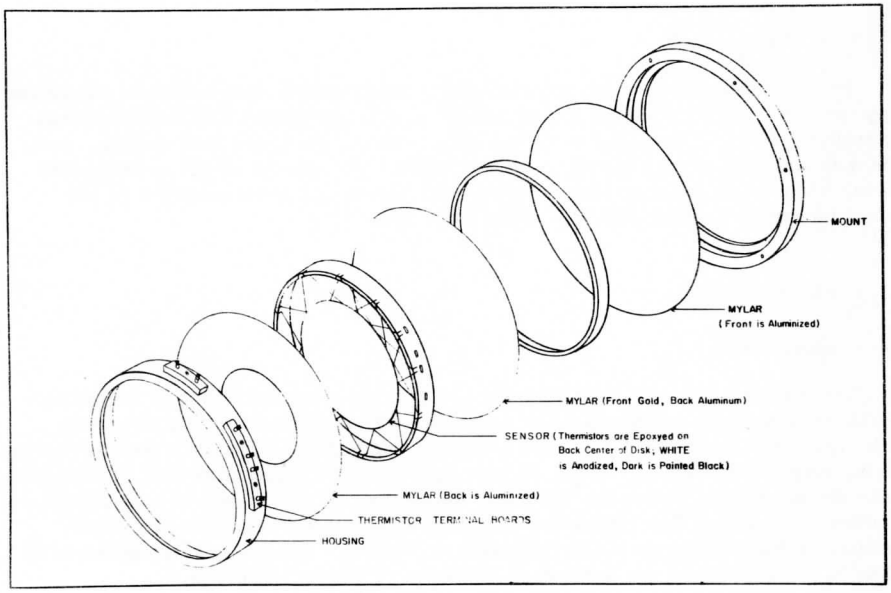

Fig. 1. Expanded view of the basic radiometer components.

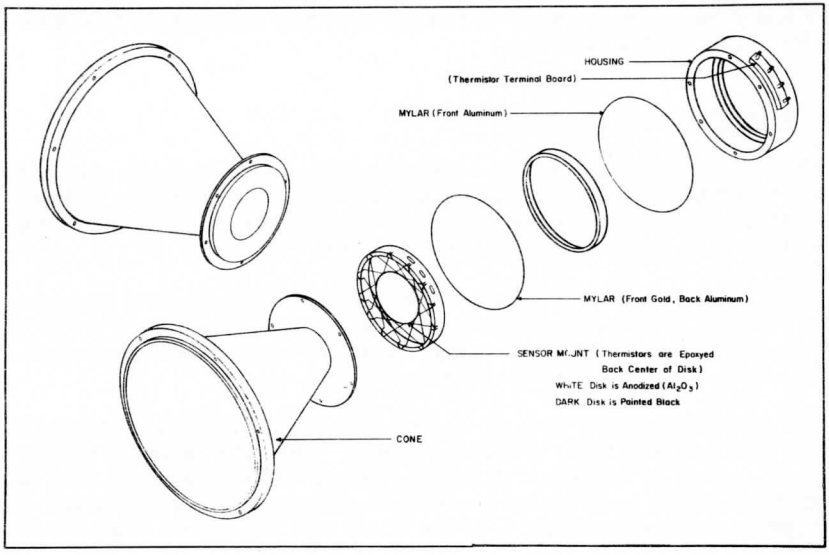

Fig. 2. Expanded view of the radiometer with cone optics.

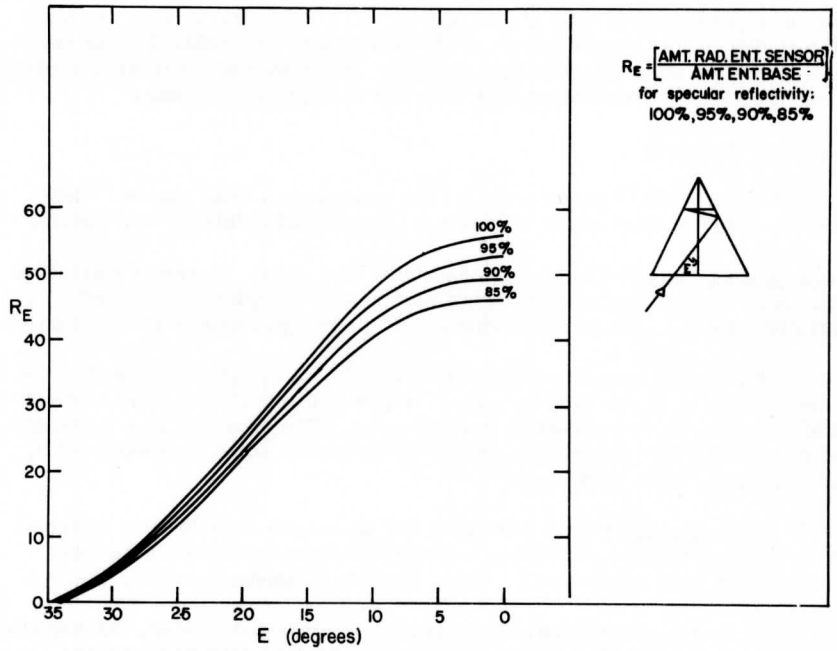

Fig. 3. Relative response (R_E) of the radiometer with cone optics as a function of angle (E) from the normal.

the disc temperature is measured. Constantan wire, 0.002 inch in diameter, connects the thermistors with the terminals on the side of the housing. Constantan wire is used because of its low thermal conductivity. An aluminized mylar baffle is used in front of the disc to prevent radiation from entering the housing where it would be reflected off the inside of the housing and strike the back side of the disc. This baffle is spaced 1/32 inch in front of the disc and has a hole slightly smaller than the disc. A thermistor is attached to the outer surface of the housing to provide an indication of its temperature.

2.3 Flat Plate with Cone Optics

A cone has been added to the basic flat plate radiometer to restrict its field of view. The construction of the sensor is shown in Figure 2. The radiometer disc in this sensor is one inch in diameter and the cone half angle is 20°. The cone surface is a highly reflecting aluminum coating evaporated onto glyptal varnish.

The relative response (R_E) of this sensor vs angle (E) from the normal appears in Figure 3.

Reference to Figures 4 and 5 shows that for N = 0° the sun will be excluded from the sensor or for the entire year if the spacecraft is launched into an orbit with its ascending node at 1500 hours or later. If the spacecraft is in an earlier orbit the direct solar illumination will vary with the time of the year.

2.4 Spectral Response

Two spectral response characteristics are employed in each sensor. They are classified by the appearance of the disc, specifically "black" and "white."

2.4.1 Black Sensors—The black sensor disc is 0.5 mil. aluminum treated on one side with irradite and painted with a Mautz 9300S black paint to give a black matte surface. The total thickness after painting is approximately 5 mils.

The paint produces a surface with reasonably high absorptivity from the visible wavelengths to beyond 25 microns. The absorptivity of this paint is given in Table 1, based on data obtained in a Hohlraum. The accuracy is $\pm$ 2 percent. The black sensor thus responds to the sum of the direct solar, reflected solar, and long wave radiation from earth.

2.4.2 White Sensors—The white discs are made from 99.99% pure aluminum which is electro-polished to produce a highly reflecting surface. It is then anodized on one side to produce a .5 mil. coating of aluminum oxide, (Al_2O_3).

This oxide has an absorptivity of about 20 percent in the visible, but becomes similar to black paint in its infrared absorbing properties beyond 7 microns. Therefore, the white sensor absorbs most of the long wave radiation from the earth, but reflects much of the solar radiation incident on it.

2.5 Sensor/Spacecraft Interface

The TOS Spacecraft is spin stabilized in the wheel mode. A single sensor mounted with its axis perpendicular to the spin axis will scan the earth once per revolution. The temperature of a single sensor would be modulated at the spin frequency; however, to reduce the effect of this modulation, two sensors of each type are used. The two sensors of a pair are mounted 180° apart on the spacecraft base plate and combined electrically in series to act as one sensor. This reduces modulation due to spin. In addition, the time constant of the sensors (which is about one minute) an order of magnitude greater than the period of satellite revolution. This also reduces modulation of the sensors due to spin.

Four sensors (one of each type) are mounted to a common panel and two such panels are mounted 180° apart, facing outwards, along the spacecraft base plate. The axis of each sensor is perpendicular to the spacecraft spin axis. The panels are thermally isolated from the spacecraft by Kel-F-blocks and an

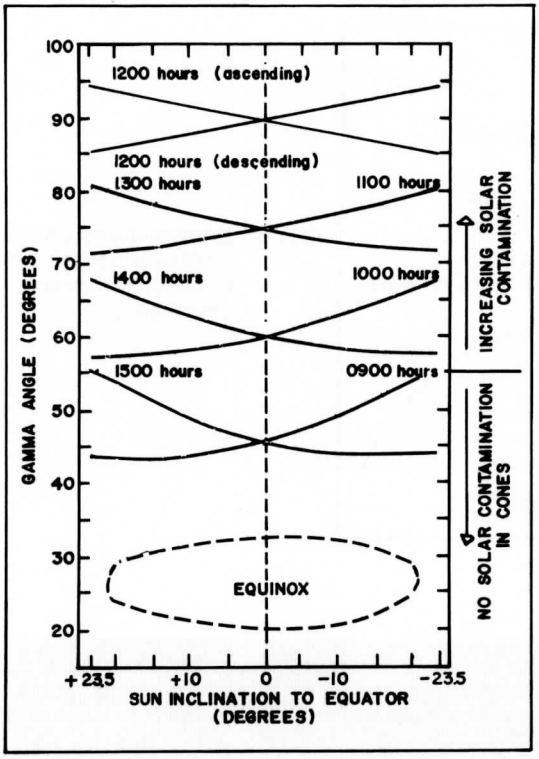

Fig. 4. Seasonal variations of gamma angle (sun angle) for different nodal crossings.

aluminized mylar radiation blanket. The panel is coated with mylar aluminized on the back side to make black surface in the infrared but reflecting in the visible. These techniques are used to radiation cool the sensor mounts to as low temperature as possible to reduce heat transfer to the sensor discs. The temperature of the mounts is monitored at three points on the back of the panel. Photographs of the sensor array appears in Figures 6, 7 and 8.

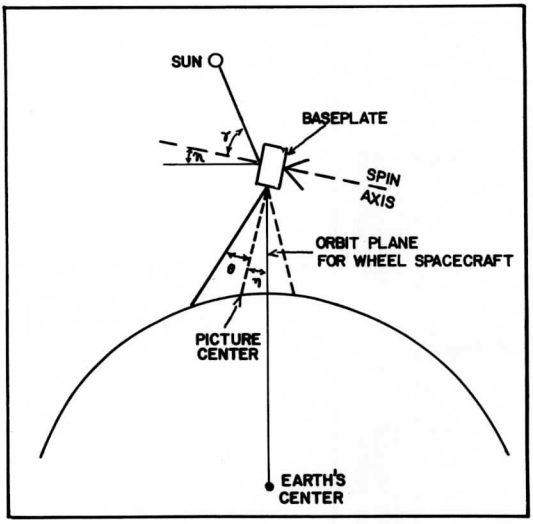

Fig. 5. Definitions of gamma angle and angles used to describe camera coverage.

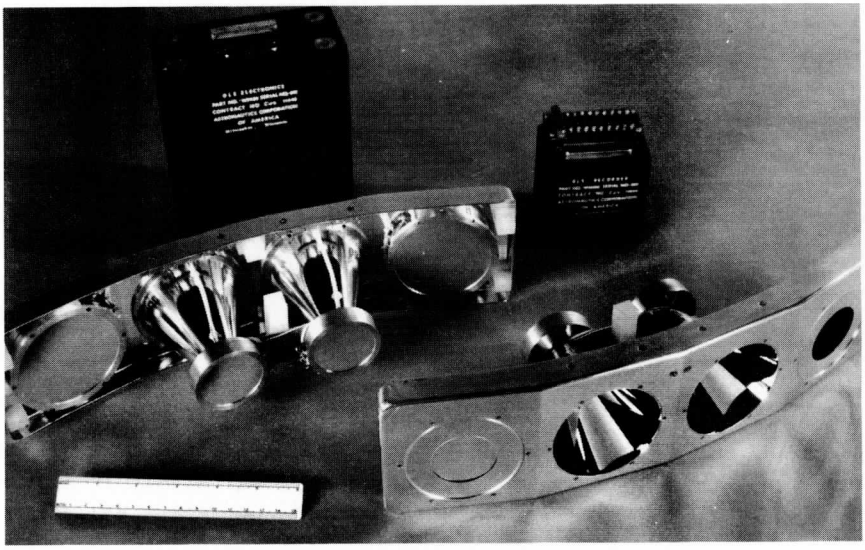

Fig. 6. Radiometers with recorder and electronics packages.

TABLE 1.

Absorptivity of Flat Black Paint, Mautz 9300S

Wavelength (microns)	Absorptivity (%)	Wavelength (microns)	Absorptivity (%)
.5	.915	8.2	.94
.75	.91	8.6	.94
1.0	.92	8.9	.93
1.9	.94	9.3	.92
2.4	.95	9.8	.94
2.8	.94	10.3	.94
3.4	.96	10.8	.95
3.8	.95	11.5	.95
4.0	.95	12.2	.94
4.5	.94	12.9	.94
4.8	.96	13.9	.88
5.1	.95	15.0	.92
5.4	.95	16.0	.91
5.7	.95	17.0	.91
5.9	.95	18.0	.90
6.2	.96	19.0	.90
6.5	.95	20.0	.91
6.7	.95	21.0	.86
7.0	.94	22.0	.87
7.3	.94	23.0	.89
7.6	.94	24.0	.89
7.9	.94	25.0	.85

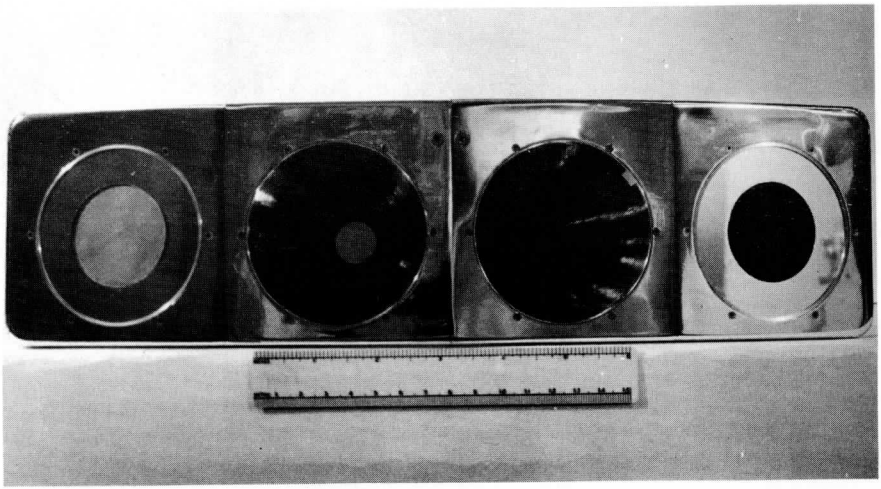

Fig. 7. Front view of the radiometer array.

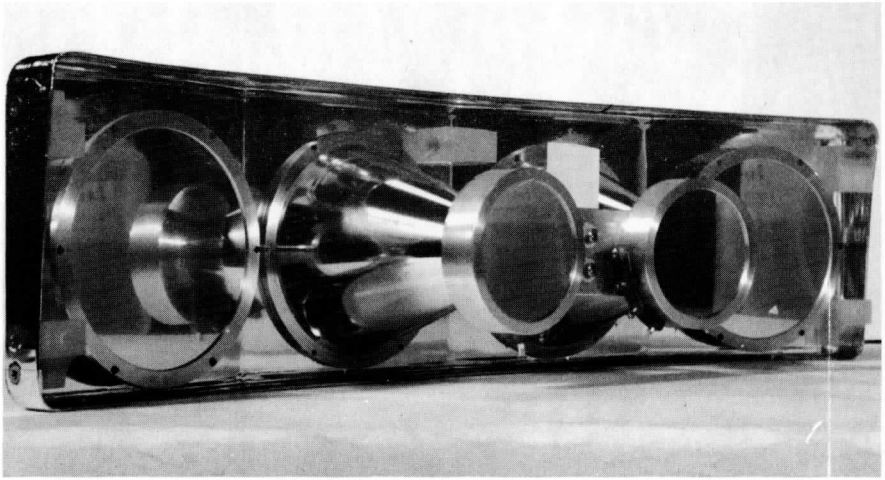

Fig. 8. Back view of the radiometer array.